Fakultät für
Mathematik und Naturwissenschaften
Astroteilchenphysik

**BERGISCHE
UNIVERSITÄT
WUPPERTAL**

Development and investigation of the Forward Beam Monitor for the KATRIN experiment

DISSERTATION
zur Erlangung des Doktorgrades
doctor rerum naturalium
(Dr. rer. nat.)

Der Fachgruppe Physik vorgelegt von

Enrico Ellinger

im April 2019

Gutachter:

Prof. Dr. Klaus Helbing, Bergische Universität Wuppertal (BUW)

Dr. Kathrin Valerius, Karlsruher Institut für Technologie (KIT)

Datum der Abgabe: 12. April 2019

Datum der mündlichen Prüfung: 12. Juli 2019

ABSTRACT

The KArlsruhe TRitium Neutrino (KATRIN) experiment, which is housed at the Karlsruhe Institute of Technology (KIT), is designed to measure the mass of the electron antineutrino in a direct and model-independent way with a sensitivity of $0.2 \, \text{eV/c}^2$ at 90% confidence level. This is achieved by a precise measurement of the beta spectrum of tritium. The electrons originate from a high luminosity windowless tritium source and are measured spectroscopically in an electro static filter (MAC-E filter).

The topic of this work is the development, investigation and final integration of the Forward Beam Monitor (FBM) of KATRIN. The FBM is used in KATRIN to monitor the relative intensity of the electron flux, generated by the tritium source, with a precision of 0.1%. Furthermore the FBM is able to record beta spectra with an energy resolution of $\sigma_{\text{FWHM}} \approx 2 \, \text{keV}$ for additional analysis. In order to achieve this degree of quality, the detector electronics, the detection device itself and its response to electron events must be well understood. Therefore measurements with electrons are performed as well as simulations which can reproduce the measured spectra.

The detector can be moved to any position in the flux tube's cross section with a positioning accuracy of $0.1 \, \text{mm}$. The positioning is realized by a more than two meter long vacuum manipulator. High demands on the hardware are made since the setup must be suitable for the use in ultra high vacuum environment, it has to be non-magnetic and must fulfill all criteria for the use in a tritium bearing system.

The present work presents the developing process from the prototype to the final commissioning of the FBM at KATRIN.

II

Deutsche Zusammenfassung

Mehr als 60 Jahre nach der Entdeckung des Neutrinos im Jahre 1953 [Rei53] hat sich die Neutrinophysik zu einem der aufregendsten Felder der Wissenschaft entwickelt. Das Phänomen der Neutrinooszillation impliziert eine nicht verschwindende Neutrinomasse, was im Widerspruch zur Beschreibung des Neutrinos im Standard Model steht. Da das Neutrino nach den Photonen das am zweithäufigsten vorkommende Teilchen in unserem Universum ist, ist seine Masse, auch wenn sie sehr klein ist, ein wichtiger Parameter im Entstehungsprozess und der weiteren Entwicklung unseres heutigen Universums. Dies begründet die große Motivation, die absolute Massenskala der Neutrinos zu bestimmen. Trotz vieler durchgeführter Experimente konnten bis heute nur obere Ausschlussgrenzen für die Neutrinomasse gemessen werden. Die heutigen besten Limits für das Elektron-Antineutrino wurden im Rahmen von Beta-Zerfalls-Experimenten mit Tritium in Mainz und Troitsk bestimmt. Eine Einführung in die Neutrinophysik mit Fokus auf die Neutrinooszillation und der Neutrinomasse ist in Kapitel 1 gegeben.

Das KArlsruher TRitium Neutrino (KATRIN) Experiment, welches sich auf dem Campus Nord des Karlsruher Institut für Technologie (KIT) befindet, ist das direkte Nachfolgeexperiment der in Mainz und Troitsk durchgeführten Experimente. KATRIN wird die Masse des Elektron-Antineutrino mit einer bis dato unerreichten Sensitivität von $0.2\,\mathrm{eV/c^2}$ (90 % C.L.) messen. Dies geschieht durch eine präzise Vermessung des Betaspektrums des Wasserstoffisotops H_3 (Tritium). Die Elektronen stammen von einer starken, fensterlosen Tritiumquelle und werden in einem elektrostatischen Spektrometer gefiltert (MAC-E-Filter). Um die hohe Sensitivität von KATRIN innerhalb von fünf Jahren zu erreichen, muss das Experiment stark vergrößert werden im Vergleich zu den Vorgängerexperimenten in Mainz und Troitsk: Das Hauptspektrometer alleine hat ein Länge von $24\,\mathrm{m}$ und eine Durchmesser von $10\,\mathrm{m}$ während die volle Länge des KATRIN Experiments $70\,\mathrm{m}$ beträgt. Im Kapitel 2 dieser Arbeit wird der experimentelle Aufbau beschrieben.

Das Thema der vorliegenden Arbeit ist der Forward Beam Monitor (FBM) von KATRIN. Der FBM ist Teil des Überwachungssystem, welches eine Reihe von Komponenten zur Stabilitätskontrolle der Quellenparameter umfasst. Um die gewünschte Präzision von KATRIN zu erreichen muss die Säulendichte der Quelle mit einer Präzision im per-mil Bereich bekannt sein. Der FBM befindet sich kurz vor der Stelle, an der der Elektronenstrahl in den Spektrometerbereich eintritt. Die Hauptaufgabe des FBM ist die kontinuierliche Überwachung des Elektornenflusses mit einer Präzision von 0.1 % ohne dabei einen Schatten auf den Hauptdetektor zu werfen. Um diese Präzision zu erreichen muss die Detektorelektronik, der Detektor selbst (p-i-n-diode) und die Detektorantwort auf Elektronenereignisse gut verstanden sein. Des Weiteren ist der FBM in der Lage, das Betaspektrum mit einer Energieauflösung von $\sigma_{\mathrm{FWHM}} \approx 2\,\mathrm{keV}$ sowie das Magnetfeld an jeder Position innerhalb der Querschnittsfläche des Stahls zu messen mit einer Positionierungsgenauigkeit von $0.1\,\mathrm{mm}$. Für die Positionierung wurde ein über zwei Meter langer Vakuum-Manipulator entwickelt mit einem Faltenbalg, welcher einen Verfahrweg von $1.8\,\mathrm{m}$ ermöglicht. An das Setup sind hohe Anforderungen gestellt da es UHV kompatibel, möglichst aus nicht-magnetischen Materialien bestehen sowie alle Kriterien für den Gebrauch innerhalb eines Tritium führenden Systems erfüllen soll.

In dieser Arbeit sind die Weiterentwicklung, die Untersuchung und die finale Integration des FBM in das KATRIN Experiment beschrieben sowie die Ergebnisse der ersten KATRIN-Messkampagnen, welche u.A. die erste Tritiummessung beinhaltet. Die Weiterentwicklung und Inbetriebnahme des vakuumdichten Manipulators wird in Kapitel 3 im Detail beschrieben einschließlich einer Untersuchung seiner Positionierungsgenauigkeit. In Kapitel 4 wird die Weiterentwicklung des Detektors und des Datenaufnahmesystems sowie deren Integration in das KATRIN Experiment beschrieben. Um Testmessungen mit Elektronen durchzuführen, wurde für diese Arbeit eine Elektronenkanone entwickelt. Der Entwicklungsprozess dieser Elektronenquelle ist in Kapitel 6 beschrieben. Zum besseren Verständnis der Detektorantwort wurden Simulationen durchgeführt, wie sie in Kapitel 7 beschrieben sind, und mit den entsprechenden Daten verglichen. Diese Arbeit schließt mit einem Fazit und einem Ausblick in Kapitel 8.

Contents

Introduction

More than sixty years after the experimental discovery of the neutrino in 1953 [Rei53], neutrino physics has developed into one of the most exciting field in physics. The phenomenon of neutrino oscillation implies that neutrinos have a finite rest mass which is in conflict with its descriptions under the Standard Model. Since the neutrino is the second most abundant particle in the universe, its mass, although it is very small, is a key parameter to understand the development of large-scale cosmic structures. Thus there is strong motivation to measure the absolute mass scale of the neutrino. Many experiments were performed to determine the neutrino's mass but so far only upper limits could be obtained. The current best limit on the electron antineutrino is $2.2\,\text{eV}/c^2$ (95 % C.L.) obtained by beta decay experiments with tritium in Mainz and Troitsk. An introduction on neutrino physics is given in Chapter 1 of this work.

The KArlsruhe TRitium Neutrino (KATRIN) experiment is the direct successor of the Mainz and Troitsk experiments and is located at the Karlsruhe Institute of Technology (KIT) at Campus North. KATRIN is designed to measure the mass of the electron antineutrino in a direct and model-independent way with a sensitivity of $0.2\,\text{eV}$ with a 90 % confidence level (corresponding to a sensitivity of $0.35\,\text{eV}$ at 5σ significance). The precise measurement of the beta spectrum of tritium is the basis of the experiment. The beta electrons, originating from a high luminosity windowless tritium source, are analyzed in a spectrometer utilizing the MAC-E filter principle. In order to achieve the aimed sensitivity of KATRIN within five years the size of the experiment is increased enormously compared to its predecessor experiments: the main spectrometer alone features a length of $24\,\text{m}$ and a diameter of $10\,\text{m}$ while the whole KATRIN experiment is $70\,\text{m}$ long. In Chapter 2 the KATRIN experiment is described in detail.

The topic of this work is the Forward Beam Monitor (FBM) of KATRIN. The FBM is part of the source monitoring system which comprises a set of instruments monitoring the stability of the source parameters. To achieve the design goal of KATRIN the column density of the tritium source must be known with per-mil precision. The FBM is located just before the electron flux, originating from the source, enters the spectrometer section. The main task of the FBM is to monitor the electron flux continuously with a precision of $0.1\,\%$ without shadowing the main detector. In order to achieve this precision the detector electronics, the detector (of silicon type) itself and its response to electron events must be well understood. Therefore measurements with electrons must be performed as well as simulations which can reproduce the data. In addition to its monitoring capability the FBM is able to record beta spectra with $\sigma_{\text{FWHM}} \approx 2\,\text{keV}$ energy resolution and can measure the magnetic field strength at any position in the flux tube's cross section with a positioning accuracy of $0.1\,\text{mm}$. The positioning is realized by a more than two meter long vacuum manipulator which includes a long bellows with a working-stroke of $1.8\,\text{m}$. High demands on the hardware are placed since the setup must be suitable for UHV, non-magnetic and fulfill all criteria for the use in a tritium bearing system.

In this work the further development, investigation and final integration of the FBM is described as well as the results of the first measurement campaigns, including the first tritium data-taking, are given. Chapter 3 comprises a detailed description of the further

development and commissioning of the vacuum manipulator including a brief study on its positioning accuracy. The further development of the detector and the data acquisition as well as their integration into KATRIN is presented in Chapter 4. The analysis results of data from commissioning phase and from the first KATRIN measurement campaigns, including the first tritium data-taking period, are shown in Chapter 5. For this work an electron gun was developed which provides electrons for test measurements during the commissioning phase of the FBM. The development process of the FBM is described in Chapter 6. In order to understand the detector response numerical simulations, as presented in Chapter 7 were performed and validated based on experimental data. The thesis closes with a conclusion and an outlook given in Chapter 8.

1 Introduction to neutrino mass

Decades after their postulation by W. Pauli in the early 20th century and their discovery twelve years later by C. Cowan and F. Reines, the physics of neutrinos has become one of the most exciting fields of science, still puzzling physicists all around the world. Neutrinos are the second most abundant and lightest fundamental massive particles in the universe.

The discovery of neutrino oscillation gave clear evidence that neutrinos have mass, in contrast to the assumption of the standard model. However, their absolute mass scale as well as the question if neutrinos are Dirac or a Majorana particles, remain unanswered up to the present day. This chapter gives a brief overview on neutrino physics starting with a short summary of the neutrino history in Sec. 1.1. The discovery and theory of neutrino oscillation is described in Sec. 1.2 and Sec. 1.3 gives an introduction into the experimental techniques of neutrino mass measurements.

1.1 A brief summary of the neutrino history

In 1896 the phenomenon of radioactivity was discovered by H. Becquerel and further investigated by M.&P. Curie and E. Rutherford in the early 20th century. In this time the β -decay was assumed to be a two-body process in which the mother nucleus X decays into a daughter nucleus Y by emitting an electron. In this picture the full energy freed in the decay is transferred to the electron resulting in a discrete single line spectrum. But there were already first hints that the β-spectrum is not discrete and in 1914 J. Chadwick finally discovered that the β-spectrum of radium is continuous. Even though a continuous spectrum in a two-body model violates the conservation of energy and momentum, it took 15 years until W. Pauli extended the β- decay to a three-body process by postulating a weakly interacting uncharged spin-1/2 particle with nonzero mass [Pau64], which carries away the missing energy and momentum and which he called "neutron" at this time.

Two years later Enrico Fermi introduced a theoretical formulation of the β-decay by assuming a point-like weak interaction and a nonzero neutrino mass [Fer34]. He could derive the transition probability, which was named "Fermi's Golden Rule" in his honor. Fermi found that the shape of the energy spectrum strongly depends on the neutrino mass, especially close to the end point, and hence it would be possible to determine the neutrino mass by a precise measurement of the spectrum. From the spectra available at this time Fermi concluded that the neutrino mass is either zero or very small in relation to the electron mass such that it can be neglected. The beta decay reaction can be written as follows:

$$\beta^-\text{-decay:} \quad {}^N_Z X \longrightarrow \quad {}^N_{Z+1}Y + e^- + \bar{\nu}_e \tag{1.1}$$

$$\beta^+\text{-decay:} \quad {}^N_Z X \longrightarrow \quad {}^N_{Z-1}Y + e^+ + \nu_e \tag{1.2}$$

The cross sections for the interaction of neutrinos with matter, calculated with Fermi's rule, are found to be small ($\sigma \approx 10^{-44}\,\mathrm{cm}^2$) which made an experimental discovery of

the neutrino difficult. It therefore took another 12 years until the first discovery of the neutrino by C. Cowan and F. Reines with their now famous "Poltergeist" experiments in 1956 [Cow56, Rei53]. Predecessor experiments, located at Hanford site, led to inconclusive results such that the experiment was moved to the Savannah River Plant where a high flux of neutrinos from fission processes was available. Two tanks filled with 200 liter water with 40 kg dissolved cadmium chloride ($CdCl_2$) served as the detector volume. The tanks were surrounded by three scintillation modules equipped with PMTs to enable the detection of scintillation light. The detection principle was the classical inverse β-decay:

$$\bar{\nu}_e + p \longrightarrow n + e^+ \tag{1.3}$$

The detection of the neutrinos is based on the delayed coincidence method. The target protons are provided by the water molecules as they are available in a large number in the tanks. The positrons quickly lose their energy in collisions and finally annihilate with shell electrons into two 511 keV photons which are emitted in opposite direction. The recoil neutron becomes thermalized within a few microseconds by collisions with water molecules and finally gets captured by a cadmium molecule. The cadmium nucleus gets excited and decays immediately into its ground state by emitting photons in the MeV range. The short time delay of typically $< 17\,\mu$s between the two signals was used to separate neutrino signals from background. During the total measurement time of 1341 hours only three neutrinos per hour were detected. With Poltergeist the cross section of the inverse beta decay has been determined to the value of $\sigma = 6.3 \cdot 10^{-44}\,\text{cm}^2$ [Cow56]. This example shows why neutrino detectors in general need large detector volumes and low noise levels to obtain a significant event rate.

In 1962 a second type of neutrino, the so-called muon-neutrino, was detected at the Brookhaven National Laboratory by L. M. Lederman, M. Schwartz, and J.S Steinberg [Dan62] and finally, in 2001, the tau-neutrino as the third neutrino flavor was discovered by the DONUT experiment at Fermilab [Kod01]. These results have confirmed the three flavor picture as it has been predicted by the standard model of particle physics.

Generation			Electric charge	Spin	Interaction
1	2	3			
e	μ	τ	$-e$	$1/2$	electromagnetic, weak
ν_e	ν_μ	ν_τ	0	$1/2$	weak
$\bar{e}$	$\bar{\mu}$	$\bar{\tau}$	e	$1/2$	electromagnetic, weak
$\bar{\nu}_e$	$\bar{\nu}_\mu$	$\bar{\nu}_\tau$	0	$1/2$	weak

Table 1.1: Overview of the 12 leptons in the standard model of particles including the three types of neutrino flavors.

In the Standard Model of Particles (SM) there are exactly three neutrinos predicted, each coupling to one of the three charged leptons: the electron e, the muon μ and the tau τ. Neutrinos are electrically neutral and interact only via the weak force. The lepton number is conserved separately for each of the three lepton families: (e, ν_e), (μ, ν_μ) and (τ, ν_τ).
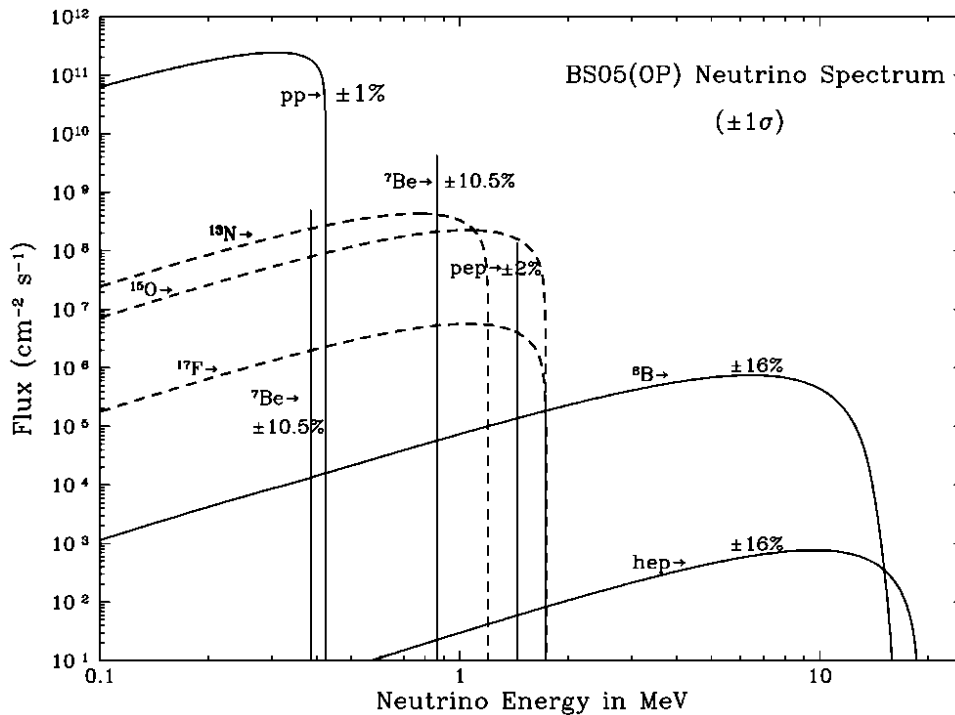
Figure 1.1: Solar neutrino energy spectrum as predicted by the standard solar model (BS05(OP)). The energy distribution of the neutrinos depend on the fusion processes in which they are produced. Taken from [Bah05].

Neutrinos have left-handed helicity, and antineutrinos are right-handed [Gol58]. In total there are 12 leptons in the SM (see Tab. 1.1).

1.2   Neutrino oscillation

During their propagation neutrinos change their flavor eigenstate periodically, e.g. a tau neutrino can be turned into a muon or electron neutrino. This phenomenon is known as neutrino flavor oscillation and implies that at least two of the three mass eigenstates are non-zero. However, in the Standard Model of particle physics neutrinos are described to be massless, thus there is strong motivation to extend the existing model. This section discusses the discovery of the neutrino oscillation phenomenon, its well described theory and the current experimental results.

1.2.1   The solar neutrino problem

In 1970 the Homestake experiment [Cle98] measured the solar neutrino flux intending to confirm the theoretical predictions on the neutrino flux calculated in the framework of the standard solar model which assumes that in total $60 \cdot 10^9$ solar neutrinos per square centimeter and per second reach the Earth (see Fig. 1.1). A tank of $615\,t$ of tetrachloroethylene

(C_2Cl_4) served as the target material, located in the Homestake gold mine $1478\,\text{m}$ underground. The neutrinos were detected with the radiochemical chlorine-argon-method following the inverse beta decay reaction:

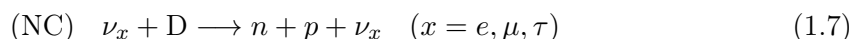$$^{37}\text{Cl} + \nu_e \longleftrightarrow {}^{37}\text{Ar} + e^- \tag{1.4}$$

After a few weeks of measuring time, only small quantities of ^{37}Ar have formed and were isolated by a radiochemical process. The ^{37}Ar atoms decay with a half-life of 35 days via electron capture into exited ^{37}Cl (Eq. 1.4 from right to left). Finally, the Auger electrons from the de-excitation of the ^{37}Cl atom were detected in a proportional counter. The rate of neutrino flux measured in this experiment was only $1/3$ of the expected flux. This deficit is called the "Solar neutrino problem". The result of the Homestake experiment was confirmed by further radiochemical experiments with ^{71}Ga at lower energy threshold (GALLEX [Ham99], SAGE [Abd02]). However, the disadvantages of these experiments were that they were only sensitive to electron neutrinos and that information about the neutrino interactions, such as energy and time of interaction got lost.

In Čerenkov-based neutrino detectors, such as Super-Kamiokande or SNO, neutrinos can be detected in real-time and their energy as well as the direction, where they originate from, can be reconstructed. The Super-Kamiokande detector consists of 50,000 tons of high-purity water surrounded by 1200 photomultipliers and is located $1000\,\text{m}$ underground [Fuk03]. Here, the neutrino can interact via elastic scattering (ES) with electrons:

$$(\text{ES}) \quad \nu_x + e^- \longrightarrow \nu_x + e^- \quad (x = e, \mu, \tau) \tag{1.5}$$
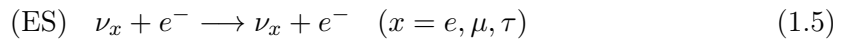
The electrons are accelerated to a velocity above the speed of light in water which cause characteristic Čerenkov radiation. Although the energy threshold is 8 times higher than for the radiochemical experiments about 18 neutrino events per day were detected due to the huge detector volume. Super-Kamiokande confirmed the neutrino deficit and in addition proved that the neutrino actually originated from the sun. Furthermore they found that muon neutrinos produced in the atmosphere traveling great distances through the Earth were disappearing and announced the discovery of neutrino oscillations in 1998 [Fuk98]. Electron neutrinos change into tau neutrinos within the Earth.

The SNO detector instead is filled with 1000 tons of heavy water (D_2O) monitored by 960 photomultipliers and is located $2000\,\text{m}$ underground in a mine in Sudbury/ Canada [Bog00]. The deuterium opens two further reaction channels, following charge current (CC) and neutral current (NC) reactions:

$$(\text{CC}) \quad \nu_e + \text{D} \longrightarrow p + p + e^- \tag{1.6}$$
$$(\text{NC}) \quad \nu_x + \text{D} \longrightarrow n + p + \nu_x \quad (x = e, \mu, \tau) \tag{1.7}$$

The observation of the CC reactions allows to determine the flux of solar electron neutrinos ν_e on the Earth, while the observation of the NC reactions allows to determine the flux of neutrinos of any flavor ν_x ($x = e, \mu, \tau$). In 2002 the SNO experiment showed that the flux of solar electron neutrinos was approximately three times smaller than the flux of all three flavors together [Ahm02]. Thus, it was proved that solar electron neutrinos were transformed to tau and muon neutrinos on their way from the sun to the Earth confirming the theory of neutrino oscillation.

In the following years further model independent experiments with artificial sources such as nuclear power plants (e.g. KamLAND [Abe08]) or particle accelerators (e.g. the MINOS experiment [Ada13]) confirmed neutrino oscillation and measured the oscillation parameters. Thus, neutrino oscillation was discovered. The theory of neutrino oscillation will be described in the next section showing that the existing neutrino data is well described if a three-neutrino mixing is assumed.

1.2.2   The oscillation of neutrino flavors

The theory of neutrino oscillation describe the effect of periodic flavor change of neutrinos. Each of the three flavor eigenstate of a neutrino $|\nu_\alpha\rangle$ where $\alpha = e, \mu, \tau$ is determined as a linear superposition of three light, stationary mass eigenstates $|\nu_i\rangle$ where $i = 1, 2, 3$:

$$|\nu_\alpha\rangle = \sum_{i=0}^{3} U_{\alpha i} |\nu_i\rangle \tag{1.8}$$

Here, $U_{\alpha i}$ represents the unitary PMNS (Pontecorvo-Maki-Nakagawa-Sakata) matrix which is the analogous of the CKM matrix describing the mixing of quarks. In the standard three-neutrino theory the matrix is 3×3 and given by ([Tan18])

$$U = \begin{bmatrix} c_{12}c_{13} & s_{12}c_{13} & s_{13}e^{-i\delta_{\mathrm{CP}}} \\ -s_{12}c_{23} - c_{12}s_{23}s_{13}e^{i\delta_{\mathrm{CP}}} & c_{12}c_{23} - s_{12}s_{23}s_{13}e^{i\delta_{\mathrm{CP}}} & s_{23}c_{13} \\ s_{12}s_{23} - c_{12}c_{23}s_{13}e^{i\delta_{\mathrm{CP}}} & -c_{12}s_{23} - s_{12}c_{23}s_{13}e^{i\delta_{\mathrm{CP}}} & c_{23}c_{13} \end{bmatrix} \tag{1.9}$$
$$\times \begin{bmatrix} 1 & 0 & 0 \\ 0 & e^{i\alpha_{21}/2} & 0 \\ 0 & 0 & e^{i\alpha_{31}/2} \end{bmatrix}$$

where $c_{\alpha\beta} = \cos\theta_{\alpha\beta}$ and $s_{\alpha\beta} = \sin\theta_{\alpha\beta}$. with the mixing angle $\theta_{\alpha\beta}\epsilon[0 : \pi/2)$. In the case the phase factor $\delta_{\mathrm{CP}}\epsilon[0 : 2\pi]$ is nonzero, CP symmetry is violated but this has not yet been observed experimentally. Only if neutrinos are identical to their antineutrinos, known as Majorana particles, the phase factors α_{21} and α_3 are meaningful. The square of the absolute value of one matrix element ($|U_{\alpha i}|^2$) gives the probability to find the neutrino in the mass eigenstate i for a given flavor α.

The evolution in time t of the mass eigenstates $|\nu_i(t)\rangle$ can be expressed as propagating plane waves:

$$|\nu_i(t)\rangle = e^{-i(E_i t - \vec{p_i} \cdot \vec{x})} \, | \nu_i(0)\rangle, \tag{1.10}$$

where E_i is the energy and $\vec{p_i}$ the momentum of the mass-eigenstate i, and $\vec{x}$ is the position of the neutrino relative to its origin.

In the ultra-relativistic limit neutrinos are traveling very close to the speed of light such that their rest mass m_i can be neglected compared to their energies E_i ($|\vec{p_i}| = p_i \gg m_i$):

$$E_i = \sqrt{p_i^2 + m_i^2} \Rightarrow p_i + \frac{m_i^2}{2p_i} \approx E + \frac{m_i^2}{2E}, \tag{1.11}$$

With this approximation and expressing the parameter t via the distance traveled l (and also dropping the phase factors), the wave function of a neutrino mass eigenstate becomes:

$$|\nu_i(L)\rangle = e^{-im_i^2 l/2E}|\nu_i(0)\rangle. \tag{1.12}$$

Because of their different masses, the oscillation frequencies of the mass eigenstates are different which results in a time dependent phase shift among the three mass-eigenstates. Since the neutrino flavor-eigenstate is a superposition of the mass-eigenstates it is possible to observe a neutrino which was originally of flavor α as a flavor β neutrino after at the distance traveled l:

$$P_{\alpha \to \beta} = |\langle \nu_\beta(L)|\nu_\alpha\rangle|^2 = \left| \sum_i U_{\alpha i}^* U_{\beta i} e^{-im_i^2 l/2E} \right|^2. \tag{1.13}$$

To simplify the calculation one can assume that only two neutrinos participate in the mixing. The corresponding PMNS matrix then reduces to a simpler form containing only one mixing angle Θ:

$$U = \begin{pmatrix} \cos\Theta_m & \sin\Theta_m \\ -\sin\Theta_m & \cos\Theta_m \end{pmatrix} \tag{1.14}$$

The probability of observing a neutrino with flavour β, created with flavour α then is given by

$$P(\nu_\alpha \to \nu_\beta) = \sin^2\left(\frac{\Delta m_{ij}^2 c^4}{4E} \frac{l}{\hbar c} \right) \cdot \sin^2\left(2\Theta_m\right). \qquad (\alpha \neq \beta) \tag{1.15}$$

One can see that the oscillation probabilities depend on the difference of the mass squares $\Delta m_{ij}^2 \equiv m_i^2 - m_j^2$ and not on the absolute masses. Figure 1.2 illustrates the oscillation
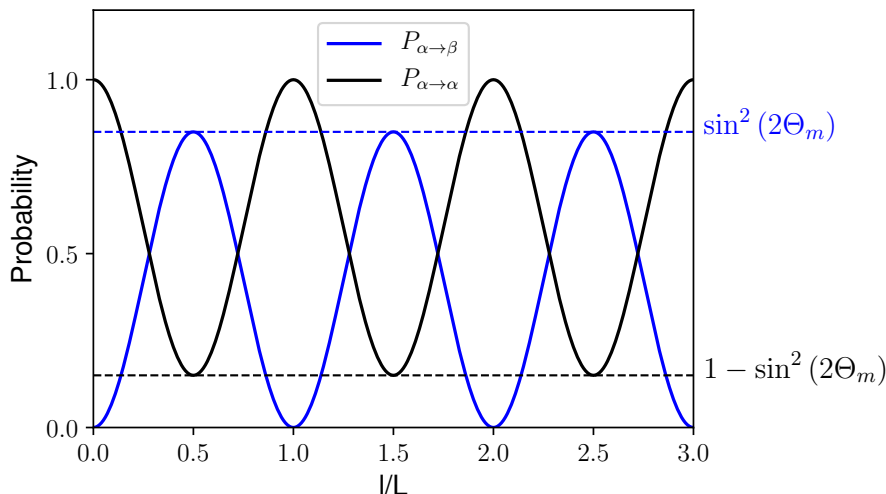
Figure 1.2: Illustration of two-flavor neutrino oscillation showing the probability of an initial neutrino of flavour α to be converted into a flavour β neutrino after distance traveled l. The maximum probability of conversion is defined by the mixing angle. This figure is inspired from [Bab10b].

probability of the two flavor eigenstates given by Eq. 1.15 with the characteristic oscillation length $L = 4\pi\hbar E \Delta m_{ij}^{-2} c^{-3}$.

One of the most important conclusions one can draw from neutrino oscillation is that neutrinos have nonzero mass and measuring the oscillation length allows determining the difference of masses squared. The combined result of the observed oscillation parameters in the three flavour case obtained by a variety of neutrino oscillation experiments, are given in Tab. 1.2.

However, oscillation experiments cannot probe the absolute mass scale of the neutrinos and also leave the question open whether or not m_2 is heavier than m_3, which is referred as the "neutrino mass hierarchy problem". Since the sign of Δm_{32}^2 is not known yet two scenarios are possible:

Normal hierarchy $m_1 < m_2 < m_3$

Inverted hierarchy $m_3 < m_1 < m_2$

An illustration of these orderings is given in Fig. 1.3. If the absolute masses m_i are much larger than the differences of the mass squares Δm_{ij}, the hierarchy is said to be "quasi-degenerated":

Quasi-degenerate hierarchy $m_1 \approx m_2 \approx m_3$

In the following section methods to determine the absolute mass will be presented.
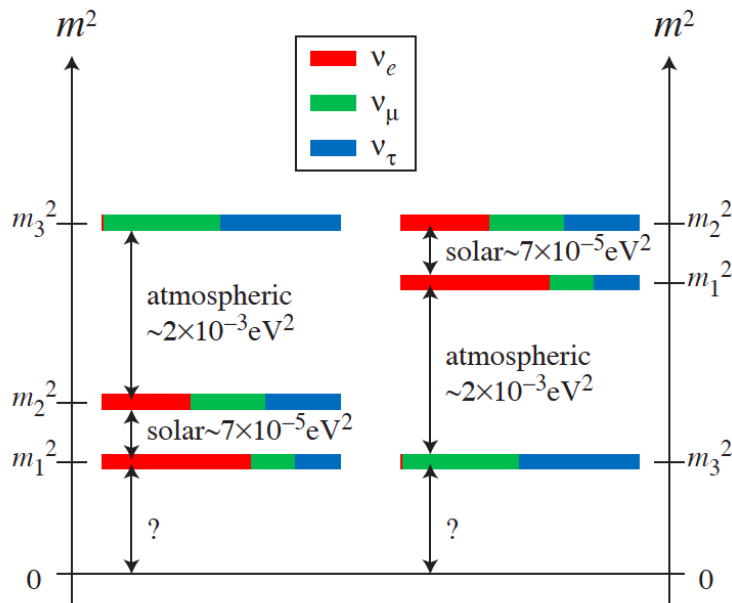
Figure 1.3: Neutrino mass hierarchy and the color-coded probability that a mass eigenstate contains a certain flavor. Note that neutrino oscillation experiments do only have experimental access to the differences of the mass squares. Since the sign of Δm_{32}^2 is not known yet, two mass orderings are possible, namely the normal mass hierarchy (left) and the inverted mass hierarchy (right). Taken from Ref. [Kin13].

1.3 Methods of neutrino mass measurements

As mentioned before only the difference of the mass squares is accessible by the neutrino oscillation experiments. To measure the absolute mass of the neutrino, complementary methods are needed. The different experimental approaches can be divided into two categories: the direct methods such as single or double β-decay experiments are based on the kinematics (energy and momentum conservation) of β-decay, while the indirect methods such as neutrino mass determination from neutrinoless beta decay or cosmology data are based on theoretical assumptions on rare decays or the imprint of cosmological neutrinos. These methods are described in the following sections.

1.3.1 Cosmological approach

Similar to the cosmic microwave background (CMB) the Big Bang theory also predicts the presence of a cosmic neutrino background which was created in the early times of the Universe at a temperature of about $1\,\mathrm{MeV}$. The estimated density of these relic neutrinos is about $112\,\mathrm{cm}^{-3}$ for each species which makes the neutrino the second-most abundant particle after the photon. Although the neutrino density and temperature have not been measured yet due to the extremely low cross sections of neutrinos, it is possible to estimate the summed mass of the neutrinos by fitting cosmological data within the standard ΛCDM model of cosmology. Although their masses are expected to be very small, the neutrinos

Parameter	Source		Value
$\sin^2(\Theta_{13})$	reactor		$(0.212 \pm 0.08) \times 10^{-2}$
$\sin^2(\Theta_{12})$	solar		0.307 ± 0.013
$\sin^2(\Theta_{23})$	atmospheric	NH	$0.421^{+0.033}_{-0.025}$
		IH	$0.417^{+0.025}_{-0.028}$
$\Delta m^2_{21}\,[\mathrm{eV}^2]$	solar		$(7.53 \pm 0.18) \times 10^{-5}$
$\Delta m^2_{32}\,[\mathrm{eV}^2]$	atmospheric	NH	$(2.51 \pm 0.05) \times 10^{-3}$
		IH	$(-2.56 \pm 0.04) \times 10^{-3}$

Table 1.2: Experimentally observed values for the oscillation parameters. The values for the Dirac CP-violation and Majorana phases δ, α_1, α_2 are currently unknown. Since the sign of Δm^2_{32} is also unknown two neutrino mass ordering are possible, the normal hierarchy (NH) and the inverted hierarchy (IH). Data taken from [Tan18].

contribute to the Universe's total energy density Ω_{tot} within the ΛCDM model which takes the different matter contributions (vacuum energy Ω_Λ, baryons Ω_b, and cold dark matter Ω_{DM}) into account. In a publication of the Planck collaboration in 2018 [Agh18] an upper limed of the sum of all three neutrino species is given:

$$m(\nu) = \sum_{i=1}^{3} m(\nu_i) < 0.12\,\mathrm{eV/c^2}\ (95\,\%\ \mathrm{C.L.}) \tag{1.16}$$

However, note that this method extremely depends on the model in which strongly correlated fit parameters have to be adjusted simultaneously. When varying these parameters, different specific neutrino mass limits are obtained. Turning it around: a precise model-independent measurement of the neutrino mass is of great importance for cosmology since the absolute neutrino mass has great impact onto the structure of the universe.

1.3.2   Neutrinoless double beta decay

The neutrinoless double beta decay ($0\nu\beta\beta$) (unobserved so far) is a beyond SM process which opens the opportunity to derive the neutrino mass and at the same time to prove whether neutrinos are Majorana particles or not. In the ordinary double beta decay ($2\nu\beta\beta$) two neutrons of a nucleus simultaneously decay into two protons:

$$2\nu\beta\beta\text{-decay:}\quad {}^{N}_{Z}X \longrightarrow {}^{N}_{Z+2}Y + 2e^- + 2\bar{\nu}_e \tag{1.17}$$

The electron spectrum of this allowed and observed process is continuous as it is in the single β-decay. Assuming the neutrino is its own anti-particle (Majorana particle) the neutrinoless double beta decay

$$0\nu\beta\beta\text{-decay:}\quad {}^{N}_{Z}X \longrightarrow {}^{N}_{Z+2}Y + 2e^- \tag{1.18}$$

is possible in which the originally continuous spectrum of the double β-decay becomes discrete such that a sharp electron energy peak will be observed at the energy of the full Q-value.

In principle $2\nu\beta\beta$ -decay can appear in any beta emitters but is much less likely compared to the single β-decay. To investigate $2\nu\beta\beta$-decay, therefore, isotopes are used in which single β-decay is energetically forbidden according to the Bethe-Weizsäcker equation [Wei35]. The two most promising isotopes are ^{76}Ge and ^{136}Xe so they are used in several experiments, such as GERDA [Ago13], EXO [Aug12] and KamLAND-Zen [Gan16].

However, by now no $0\nu\beta\beta$-decay was observed. But it is possible to obtain limits on the effective neutrino mass. The inverse half time for $0\nu\beta\beta$-decay is given by

$$(T_{1/2}^{0\beta})^{-1} = G \left|\mathcal{M}\right|^{2} \left|m_{\beta\beta}\right|^{2} \tag{1.19}$$

where G is a phase space factor, M is the nuclear transition matrix element. Hence the current limits on the half time obtained in the ongoing experiments also give limits on the neutrino mass. The current best limit from $0\nu\beta\beta$-decay is

$$m_{\beta\beta} = \sum_{i=1}^{3} m_i U_{ei}^2, < 0.05 \text{ to } 0.16\,\text{eV/c}^2 \ (90\,\% \text{ C.L.}) \tag{1.20}$$

given by the KamLAND-Zen collaboration. Note that this limit is only valid if $0\nu\beta\beta$-decay actually exists.

1.3.3   Single beta decay

Another method to measure the neutrino mass, which is also the basic approach of the KATRIN experiment, is given by investigating the kinematics of the three body process in the single β-decay (Eq. 1.1). Since it is fair to assume that the kinematics of this process are well understood, this method can be regarded to be model independent. Neglecting the recoil energy of the nucleus the decay energy (Q-value) is only shared between the electron and the neutrino where the energy of the neutrino is given by

$$E_\nu = \sqrt{m_\nu^2 c^4 + p_\nu^2 c^2}. \tag{1.21}$$

In case of a nonzero neutrino rest mass m_ν the end point of the tritium spectrum is shifted by the neutrino's rest mass (see Fig. 1.4). Therefore investigating the shape of the beta spectrum close to the end point allows drawing conclusions on the neutrino mass. The transition rate $\Gamma_{i\to f}$ of the β-decay process can be calculated with Fermi's Golden Rule:

$$\Gamma_{i\to f} = \frac{\mathrm{d}^2 N_e}{\mathrm{d}E\mathrm{d}t} = \frac{2\pi}{\hbar} \left|\mathcal{M}_{fi}\right|^2 \rho(E_f) \tag{1.22}$$
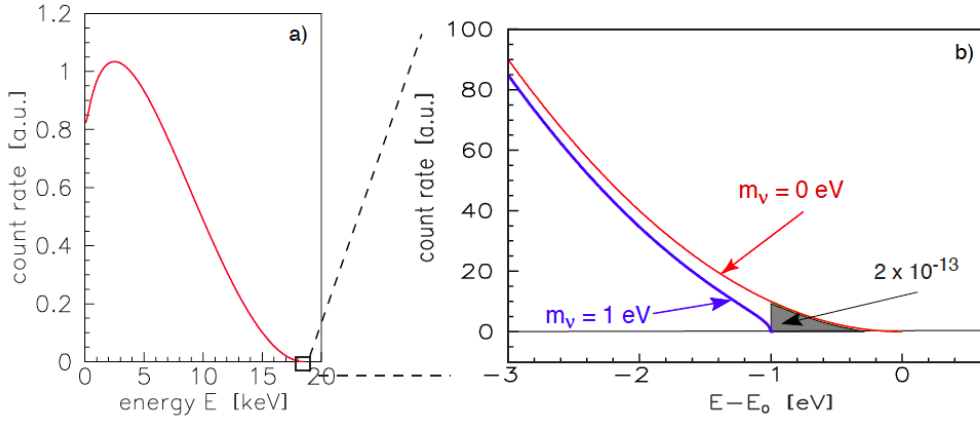
Figure 1.4:   a) Entire electron energy spectrum of tritium β-decay (complete). **b)** Spectrum close to the end point E_o for a vanishing neutrino mass (red) and a nonzero neutrino mass of $m_{\bar{\nu}_e} = 1\,\text{eV}$ (blue). Taken from [KAT05]

where M_{fi} denotes the matrix element for the transition of the initial state i to the final state i and $\rho(E_f)$ corresponds to the final states density of energy E_f. Applying the relativistic relation of the energy-momentum, the integrated rate over all possible discrete and continuous final states is given by [Ott08, KAT05]:

$$\frac{\mathrm{d}N_e}{\mathrm{d}E}(E) = C\cdot F(Z+1,E)\cdot p\cdot(E+m_ec^2)\cdot(E_0-E)\cdot\sqrt{(E_0-E)^2 - m(\nu_e)^2c^4}\cdot\Theta(E_0-E-m(\nu_e)c^2) \tag{1.23}$$

with the constant

$$C = \frac{G_f^2\cos^2(\theta_c)}{2\pi^3c^5\hbar^7}\,|\mathcal{M}|^{\,2} \tag{1.24}$$

where

F :   Fermi function (includes the Coulomb interaction between doughter nucles and electron)

E :   kinetic energy of the electron

p :   momentum of the electron

E_0 :   end point energy (equals the Q-value if recoil energy is neglected)

Θ :   Heaviside function (ensures the conservation of energy)

G_f :   Fermi coupling constant

θ_c :   Cabibbo angle

$\mathcal{M}$:   matrix element

In Fig.1.4 the theoretical differential spectrum is shown. The experimental observable in Eq. 1.23 is the square of the effective electron anti-neutrino mass $m_{\bar{\nu}_e}^2$, which is given by the incoherent sum of the three neutrino mass eigenstates m_{ν_i}:

$$m_{\bar{\nu}_e}^2 = \sum_i |U_{ei}|^2 \, m_{\nu_i}^2 \qquad (1.25)$$

with the neutrino mixing matrix U_{ei}.

The currently best limits on the electron anti-neutrino mass by kinematic methods have been achieved by measurements of the tritium β-spectrum with Magnetic Adiabatic Collimation Electrostatic (MAC-E) filters. The upper limits achieved by experiments in Mainz [Kra05] and Troitsk [Ase11] are given by:

$$
\begin{aligned}
\text{Troitsk experiment:} \quad & 2.2 \, \text{eV/c}^2 \quad (95\,\% \text{ C.L.}) \\
\text{Mainz experiment:} \quad & 2.3 \, \text{eV/c}^2 \quad (95\,\% \text{ C.L.})
\end{aligned}
$$

KATRIN, the direct successor of these experiments, aims to improve these limits by one order of magnitude.

2   The KATRIN Experiment

KATRIN (KArlsruhe TRitium Neutrino experiment) is the upcoming next generation experiment to determine the effective mass of the electron anti-neutrino ($\bar{\nu}_e$) in a direct and model-independent way with a sensitivity of $0.2\,\text{eV}$ with a $90\,\%$ C.L (corresponding to $0.35\,\text{eV}$ at the statistical significance of 5σ) after three years of data taking (five calendar years of operation). This design goal is to improve the former upper limits by the Mainz and Troitsk experiments by one order of magnitude. In order to achieve this KATRIN will precisely measure the shape of the spectrum of the tritium β-decay. The experiment is located at the Karlsruhe Institute of Technology (KIT).

In this chapter an overview on the KATRIN experiment is given. In section 2.1 the measuring principle of MAC-E filters is explained. In section 2.2 the main components of the experiment and their working principles are described. Since this work focuses on monitoring the KATRIN tritium source, the different monitoring methods are described in more detail in section 2.3.

A more detailed description of KATRIN, complementing the introduction given in this chapter, can be found in the KATRIN design report [KAT05].

2.1   MAC-E filter electron spectroscopy

To obtain the neutrino mass from a precise measurement of the end point region of the tritium β-spectrum both a high energy resolution and a high source luminosity is required. The Magnetic Adiabatic Collimation with Electrostatic (MAC-E) filter technique was successfully applied for both preceding neutrino mass experiments in Mainz [Lob85] and Troitsk [Pic92] and will also be applied at KATRIN.

MAC-E filters combine electrostatic filtering and magnetic adiabatic collimation. The electrons are guided adiabatically from the source with the help of strong magnetic fields provided by superconducting magnets. Since electrons from the tritium decay are emitted isotropically their momentum $\vec{p}$ can feature both a parallel component $p_\parallel = |\vec{p}|\cos\theta$ and a transversal component $p_\perp = |\vec{p}|\sin\theta$ where θ denotes the angle between electron momentum and magnetic field (also known as pitch angle). Then the full energy can be written in two components (in the non-relativistic case):

$$E_{\text{kin}} = \frac{|\vec{p}|^2}{2m_e} = E_\parallel + E_\perp = E_{\text{kin}}\cos^2\theta + E_{\text{kin}}\sin^2\theta \tag{2.1}$$

The "longitudinal energy component" $E_\parallel$ propagates the electrons along the field lines while the "transversal energy component" $E_\perp$ causes the rotational movement. Both movements superimpose to a cyclotron movement. For the transport of an electron along a magnetic field line the adiabatic invariance is important which implies that the product of the magnetic moment $\mu = E_\perp/B$ and Lorentz factor is constant. In the case of tritium with its low
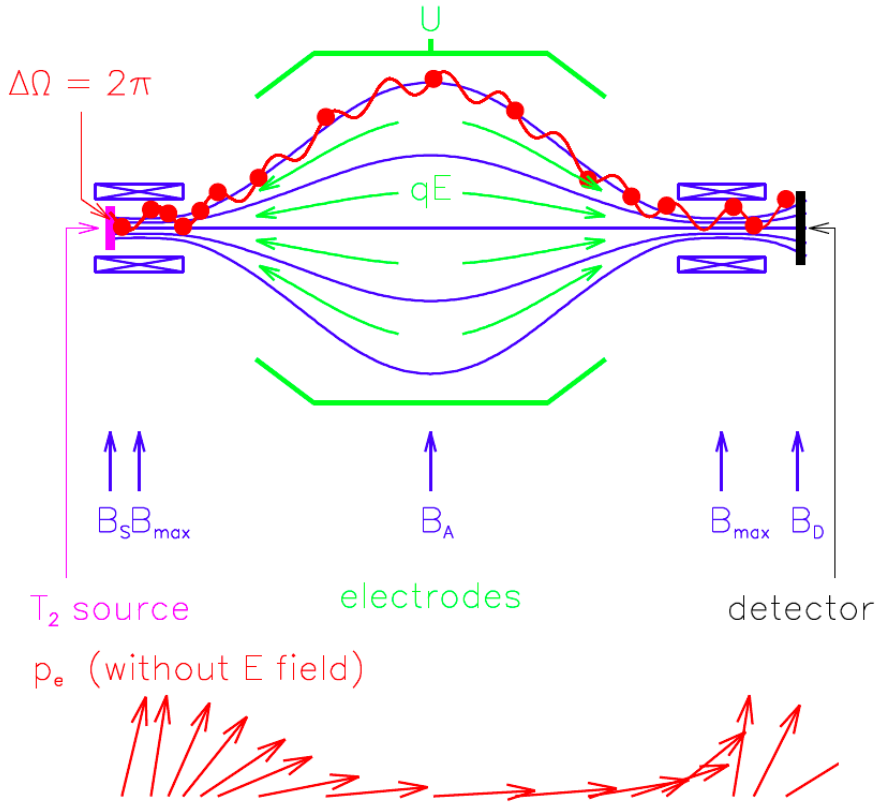
Figure 2.1:   The working principle of a MAC-E filter. The schematic shows the magnetic (blue) and electric (green) field lines as well as one trajectory (red) of an electron traveling through the filter with cyclotron motion. The retarding potential U determines the minimum energy qU a particle of charge q must feature to pass the filter while the different magnetic fields B_x define the energy resolution and the acceptance angle of the setup (see text for details). Following the conservation of the magnetic moment the electron's transversal momentum (red arrows) is transformed into a longitudinal momentum. Figure taken from Ref. [KAT05].

Q-value the electrons feature a mild relativistic gamma factor ($\gamma = 1.04 \approx 1$) such that in a first approximation only the magnetic moment needs to be considered:

$$\mu = \frac{E_\perp}{B} = \text{const.} \tag{2.2}$$

Thus, if the magnetic field is changed, the transversal energy component changes in the same way. A MAC-E filter takes advantage of this fact as illustrated in Fig. 2.1: the MAC-E filter utilizes an electrostatic retarding potential U to analyze the longitudinal energy. Therefore the transversal energy is transformed into longitudinal energy by lowering the magnetic field, following Eq. 2.2. To ensure that this transformation happens adiabatically the magnetic field gradient must be sufficiently small ($\Delta B/B \ll 1$). This process is called magnetic adiabatic collimation. The magnetic field reaches its minimum at the maximum of the retarding in the center of the MAC-E filter, in the so-called analyzing plane. At this point only electrons with sufficient longitudinal energy can overcome the retarding

potential. Since the magnetic field can never be zero, a small part of transversal energy alway remains.

The energy loss, mainly due to scattering, is prone to large uncertainties and it is therefore beneficial to limit the absolute path length of the electrons through the experiment by limiting their starting angle θ and hence their transversal energy component. With Eq. 2.1 and 2.2 the maximum acceptance angle becomes

$$\theta_{\max} = \arcsin \sqrt{\frac{B_{\mathrm{s}}}{B_{\max}}} \tag{2.3}$$

where B_{s} is the magnetic field in the source and $B_{\max}$ the maximum magnetic field at the entrance of the MAC-E filter[1].

The resolution of MAC-E filters is basically determined by the residual transversal energy component $E_\perp$ at the analyzing plane. It is given by

$$\frac{\Delta E}{E} = \frac{B_{min}}{B_{max}} \tag{2.4}$$

where $B_{\min}$ is the magnetic field at the analyzing plane. At KATRIN the field configuration is $B_s = 3.6$ T, $B_{\max} = 6$ T and $B_{\min} = 0.3\,\mathrm{mT}$ which results in the acceptance angle $\theta_{\max} \approx 50.77°$ and the high resolving power of $\Delta E \approx 0.93\,\mathrm{eV}$.

2.2   Main Components

KATRIN is located at the KIT Campus North, where the Tritium Laboratory Karlsruhe (TLK) provides the expertise and infrastructure to handle the large amount of gaseous molecular tritium required by the experiment. In Fig. 2.2 an overview of the 70 m-long beam-line is shown including all major components. The setup can be divided into two parts which are located in two different buildings.

Source and Transport Section (STS)   The STS contains all tritium-bearing components and is therefore located in the TLK building. It includes the windowless gaseous tritium source (WGTS), the rear section, the Differential Pumping Section (DPS) and the Cryogenic Pumping section (CPS).

Spectrometer and Detector Section (SDS)   The SDS houses all tritium free components and is located outside the TLK in the spectrometer hall. It contains the pre- and main spectrometer as well as the detector system (FPD).

In this section the major components are discussed.

---

[1]At KATRIN an asymmetrical magnetic field configuration is chosen such that the maximum magnetic field is located at the end of the main spectrometer just before the detector.
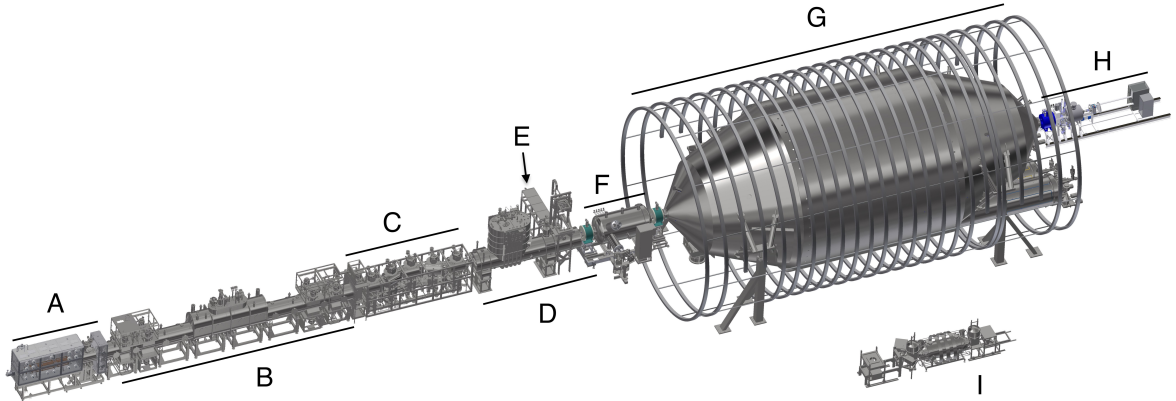
Figure 2.2: Overview of the 70 m-long KATRIN beam including all major components: **(A)** Rear section **(B)** Windowless Gaseous Tritium Source (WGTS) **(C)** Differential Pumping Section (DPS) **(D)** Cryogenic Pumping Section (CPS) **(E)** Forward Beam Monitor (FBM) **(F)** Pre-spectrometer **(G)** Main spectrometer **(H)** Focal Plane Detector (FPD) system **(I)** Monitor spectrometer

2.2.1   Tritium source

The central piece of the windowless gaseous tritium source (WGTS) is a 10 m long evacuated beam tube with an inner diameter of 90 mm. Gaseous molecular tritium (T_2 at temperature $T = 27$ K) is injected through capillaries at the center of that beam tube and pumped out again at both ends by differential pumping systems (DPS1-R and DPS1-F). The source is terminated upstream by a gold-plated disc (Rear Wall) but features no window downstream that could cause electron energy loss. The tube is surrounded by seven superconducting magnets creating a highly homogenous magnetic guiding field along the beam tube of $B_s = 3.6$ T.

The column density $\rho d = N/A$ of the source is defined by the number of gas molecules N per cross-section area A and can be controlled by the gas inlet pressure p_{in}. It is possible to increase the source activity by increasing the column density but this would also increase the scattering probabilities. For KATRIN the optimal inlet pressure is $p_{in} = 3.4 \cdot 10^{-5}$ mbar (results to a flow of $q = 1.853$ mbar $\cdot$ l/s) such that the column density equilibrates to the value $\rho d = 5 \cdot 10^{17}$ cm^{-2} . The full magnetic flux tube in the source is $\Phi_{\text{full}} = 229$ Tcm^2 but for tritium analysis only the so-called inner flux tube $\Phi_{\text{i}} = 191$ Tcm^2 is used which corresponds to the cross-section area $A_i = 53$ cm^2. With the nominal tritium purity of $\epsilon_t = 95$ % the β-decay activity of the source is

$$A_\beta = \epsilon_t \cdot \rho d \cdot A_i \cdot \frac{\ln(2)}{t_{1/2}(T)} \cdot 2 \approx 10^{11} \, \text{Bq} \tag{2.5}$$

considering the tritium half time of $t_{1/2}(T) = 12.3$ years. The factor 2 originates from the fact that each tritium molecule T_2 contains two tritium atoms. In order to achieve
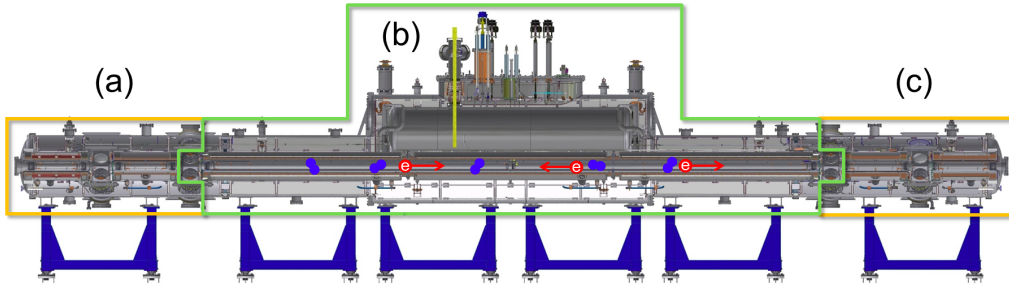
Figure 2.3: Cross section view of the windowless gaseous tritium source (WGTS). Cold gaseous tritium molecules (blue) (T_2, temperature $T = 27\,\text{K}$) are injected via capillaries into the center of a $10\,\text{m}$ long evacuated beam tube (b). Electrons from beta decay (red) are guide through the source via magnetic fields ($B_s = 3.6\,\text{T}$) produced by seven superconducting magnets. The gas is pumped-out again by two $3\,\text{m}$-long differential pumping systems (DPS1-R (a) and DPS1-F (c)) at both ends of the tube. Figure taken from [Wan13].

the sensitivity goal of KATRIN the column density must be kept stable at a level of $0.1\,\%$. Therefore the source parameters are kept under constant monitoring. Since source monitoring is one of the scopes of this work its concept is described in more detail in Sec. 2.3.

2.2.2   Transport sections (DPS and CPS)

The transport section connects the WGTS and the spectrometer section. It is needed to reduce the tritium flow to the spectrometer (since there is no physical barrier in the source), thus preventing tritium related background in the spectrometer section. To fulfill the design goal of KATRIN the tritium flow must be reduced by 14 orders of magnitude. Two pumping sections, namely the differential pumping section (DPS) and the cryogenic pumping section (CPS), utilize different approaches to achieve a reduction of seven orders of magnitude each.

DPS   The full differential pumping section (DPS) is the first pumping stage (see Fig. 2.2 and 2.4). It features an approximately $6.5\,\text{m}$-long beam tube consisting of five elements arranged with an angle of $20°$ between each of these elements to form chicanes. Along the chicanes four high performance turbomolecular pumps (TMPs) with an overall pumping speed of more than $2400\,\text{l/s}$ for T_2 are installed. The neutral tritium molecules cannot overcome the chicanes such that they hit the walls of the beam tube and can get pumped out. Five superconducting magnets, providing a field strength up to $5.5\,\text{T}$, guide the electrons through the chicane without collisions with the walls. However, ions are produced in large numbers inside the tritium source as well and can also be guided to the spectrometer and produce background. To prevent this from happening the ions are removed by electrostatic dipole fields via the $\vec{E} \times \vec{B}$ drift. In order to analyze the ions, a Fourier Transform-Ion Cyclotron Resonance (FT-ICR) mass spectrometer is installed [UD09]] [[Ubi11]]). At the exit of the DPS the tritium flow is reduced by seven orders of magnitude.
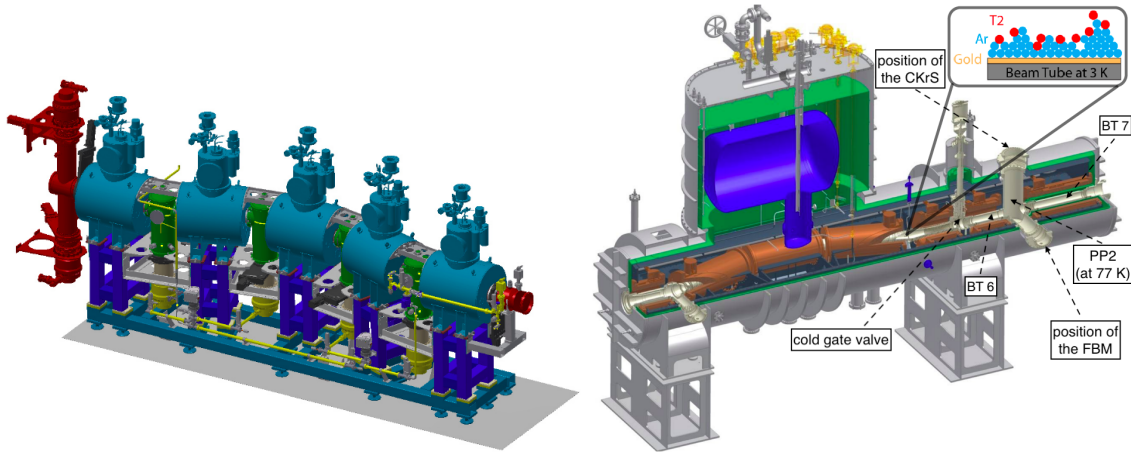
Figure 2.4: Technical drawing of the transport section. **Left:** The DPS features five beam tube segments worming a chicane and each sourced by super conducting magnets guiding the electrons through the chicane while uncharged particle as tritium molecule (T_2) hit the walls and get pumped out. Taken from [Jan15]. **Right:** The gold plated beam tubes of the CPS are cooled down to $3\,K$ and prepared with an argon frost layer on which tritium molecules get captured. Behind the cold gate valve the pump port 2 (PP2) is located (between beam tube (BT) 6 and 7) which provides access to the CPS. The Forward Beam Monitor (FBM) is mounted to the vertical port. Figure adapted from [Wan13].

CPS   At the end of the DPS the tritium flow is still too high and must be reduced by another seven orders of magnitude in the cryogenic pumping section (CPS) which makes use of the so-called cryosorption technique. The CPS beam tube has a length of about $7\,m$ and features, like the DPS, a chicane with an angle of $15°$ in between its elements. The gold-coated beam tube is cooled down with liquid helium to a temperature of $4\,K$ and cold argon snow will be frozen on the beam tube surface. This argon frost layer has a high sticking probability for all neutral molecules including tritium T_2. To limit the background contribution from the decay of the absorbed tritium molecules the cryosorption pump is regenerated every two months by removing the absorbed gas, flushing, out-baking and preparing a new argon frost layer. There are seven superconducting magnets guiding the electrons in a field of $5.6\,T$.

Besides the gas reduction capability the CPS features two pump ports (PP1 and PP2) which are equipped with vacuum monitoring equipment, such as pressure gauges, residual gas analyzers and pumps. Pump port 2 (PP2) in addition provides both a horizontal and vertical port which allow access to the CPS from the outside. They lead to a $255.7\,mm$ wide cylindric vessel, which connects beam tubes 6 and 7 of the CPS. At these ports two calibration and monitoring instruments are installed, namely the Condensed Krypton Source (CKrS) and the Forward Beam Monitor (FBM). At the horizontal port the FBM is located, which is the subject of this thesis and will be introduced and discussed in detail in Sec. 2.4 and from Ch. 3 on. The CKrS, which is mounted to the vertical port, provides conversion electrons from krypton (^{83m}Kr) gas condensate at a cold finger, to check for drifts in the retarding potential of the MAC-E filter. Both devices can be separated from the CPS volume by valves. Pump port 2, as well as the beam tubes 6 and 7, are cooled with liquid nitrogen down to $77\,K$.

2.2.3 Spectrometers

The spectrometer section comprises two MAC-E filters (see Sec. 2.1), the pre- and main spectrometer, in a tandem setup in which the high-precision β-spectroscopy takes place. A third spectrometer, the monitor spectrometer, is implemented in parallel to the beam line in order to monitor small fluctuations of the main spectrometer's high voltage. All three spectrometers are basically large stainless steel ultra high vacuum ($< 10^{-11}$ mbar) vessels with a appropriate electrode and magnet system to form a MAC-E filter.

Pre-spectrometer   The task of the 3.4 m-long and 1.7 m-wide pre-spectrometer is to reject the vast majority of the β-electrons with energies well below the tritium end point $E_0 = 18.6$ keV. As pointed out in Sec. 1.3.3 only the electrons close to the end point are used for the neutrino mass analysis. To avoid background signals from ionization of residual gas in the main spectrometer, electrons below the threshold of 18.3 keV are rejected which corresponds to an electron flux reduction by a factor of 10^7. Two superconducting magnets, one at each end of the pre-spectrometer, generate a field of 4.5 T. Unlike for the main spectrometer, high filtering precision and hence high field stability is not critical for the pre-spectrometer.

Main spectrometer   The main spectrometer is the analyzing MAC-E filter of KATRIN. It is a much larger version of the pre-spectrometer featuring a length of 24 m, a diameter of 10 m and a volume of 1240 m³. The large dimensions are a consequence of the design requirements for precise energy-analysis and adiabatic transport (see Sec. 2.1). The high-voltage for the retarding potential is applied to the vacuum vessels itself. Additionally a two-layered wire electrode system is installed at the inner surface of the vessel. These wires are kept about 100 V below the vessel voltage to prevent secondary electrons, which are emitted from the vessel wall (e.g. from interaction with cosmic muons or from radio active decays) from entering the flux tube.

In order to reach the ultra low pressure of $p < 10^{-11}$ mbar the main spectrometer is equipped with six TMPs and in total 3000 m of Non-Evaporable-Getter (NEG) stripes. Since getter pumps emit radon, which is a source of background inside the main spectrometer, a cooled (77 K) copper baffle is positioned in front of each pump. These baffles absorb the radon such that it can not decay in the flux tube. Pre- and main spectrometer share the magnet which is located between them and creates 4.5 T. The second magnet of the main spectrometer creates a magnetic field of 6.0 T at the exit side. Additionally, in order to compensate for the earth magnetic field and for fine tuning the field in the spectrometer, a large volume air coil system is installed, surrounding the main spectrometer vessel.

2.2.4 Focal plane detector

Electrons passing the main spectrometer are finally register by a p-i-n diode-type silicon detector which terminates the flux tube at the end of KATRIN. Two super conducting solenoids guide the signal electrons to the wafer. The segmented detector with 90 mm

sensitive diameter covers the inner flux tube of $\Phi_i = 191\,\mathrm{Tcm}^2$. The 148 pixels of the array, all of equal area, are arranged similar to a dart board pattern. The central four pixels form the bulls eye which is surrounded by twelve concentric rings and each of these rings has twelve segments. The mean energy resolution of the pixels is about $(2.2\pm0.2)\,\mathrm{keV}$ FWHM which allows separation of the electron signal from background. In order to keep the background rate below $10^{-3}\,\mathrm{cps}$ in the region of interest (ROI) the detector includes an active muon veto system and passive shielding with lead and copper surrounding the detector. Additionally, a post acceleration electrode is installed such that the signal can be shifted up to $35\,\mathrm{keV}$ to further reduce background and to increase the detection efficiency at the same time.

2.2.5   Rear section

The rear section is located at the rear side of the WGTG terminating the primary KATRIN beam line. It comprises a calibration and monitoring system (CMS-R): the X-ray detectors (BIXS) and the rear section electron gun (RS e-gun). Since both devices are part of the source monitoring system they are explained together with the further source monitoring devices in the next section. A detailed description of the Rear section can be found in Ref. [Bab14].

2.3   Monitoring methods for the KATRIN tritium source

Among several other sources of systematic uncertainties, such as uncertainties due to the final distribution of the daughter molecule of $(^3\mathrm{HeT})^+$ or scattering processes in the source (see Ref. [KAT05]), the fluctuation in the column density ρd of the source is one of the main contributions to systematic uncertainties on the analysis of the observable m_ν^2. None of these contributions is expected to add more than $\sigma_\mathrm{syst.} = 0.0075\,\mathrm{eV}^2$ which, together with the expected statistical uncertainty of $\sigma_\mathrm{stat.} = 0.018\,\mathrm{eV}^2$, leads to the total uncertainty of

$$\Delta m_\nu^2 = \sqrt{\sum_{i=1}^{5} \sigma_\mathrm{syst.,\, i}^2 + \sigma_\mathrm{stat.}^2} = 0.025\,\mathrm{eV} \tag{2.6}$$

resulting to KATRIN's target sensitivity of $0.2\,\mathrm{eV}$ ($90\,\%$ C. L.). Figure 2.5 shows the systematic error caused by an unobserved change in the column density. The horizontal black line represents the above mentioned upper limit $\sigma_\mathrm{syst.}$. This makes clear that, depending on the analyzing energy interval, it is required to monitor the source parameters on the per-mil level. This is done by a number of monitoring systems (see Fig. 2.6) which apply different methods to measure the working parameters of the WGTS. While the gas inlet pressure and the temperature of the WGTS are monitored and controlled with $0.1\,\%$ precision within the so-called inner loop (see Fig. 2.6) by conventional methods, dedicated customized monitoring systems are applied for monitoring the activity, column density and the gas composition of the source. These systems are presented in this section.
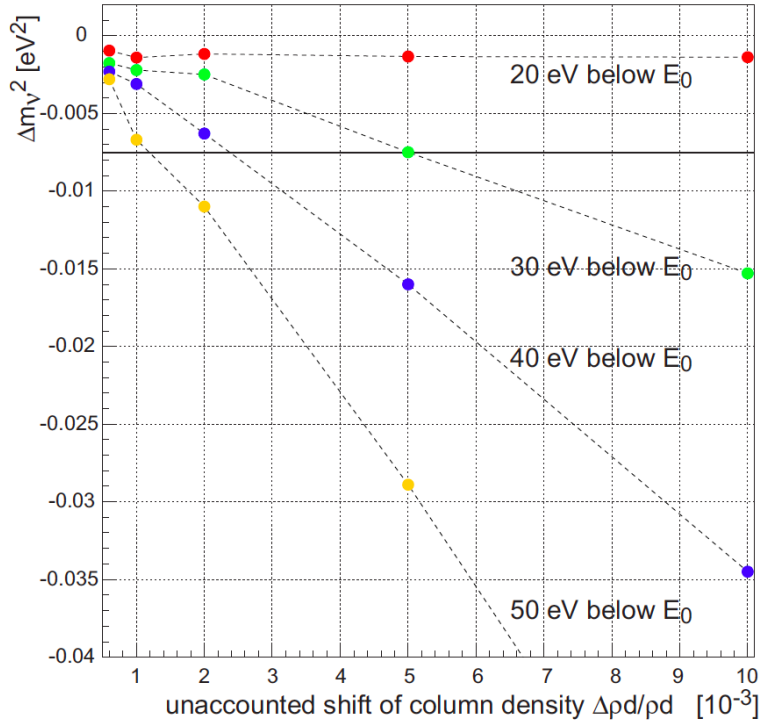
Figure 2.5: The impacted of unaccounted shift of the column density on the systematic uncertainty for different analysis intervals. For instance: if the end point region $[E_0 - 30\,\text{eV}, E_0]$ is used for neutrino analysis an unaccounted shift of the column density above $0.5\,\%$ will induce a systematic uncertainty above the limit of $\sigma_{\text{syst.}} = 0.0075\,\text{eV}^2$ (black horizontal line). Taken from [KAT05].

2.3.1   BIXS

The rear sections includes a β-induced X-ray spectroscopy (BIXS) system for monitoring the activity of the source. It comprises two custom-made high-resolution silicon drift detectors which are attached close to the so-called Rear Wall (RW) of the rear section. The gold plated RW terminates the beam line upstream such that electrons from β-decay impinging the RW induce X-ray fluorescence and bremsstrahlung. A part of the emitted X-ray radiation pass through two beryllium windows to reach the detectors. Half of the isotropically emitted β-electrons are guided in backwards direction directly to the RW while most of the electrons, which are emitted in forward direction, will be reflected either by magnetic mirroring or by the high potential barrier in the main spectrometer and finally also reach the RW. The intensity of the X-ray radiation is proportional to the number of electrons impinging the RW. BIXS measures the source activity with a precision of 0.1% over time intervals of 100 s.

2.3.2   LARA

The Laser-Raman (LARA) system measures the composition of neutral gas molecules in the source [Sch11]. It is integrated into the inner loop system. The system takes
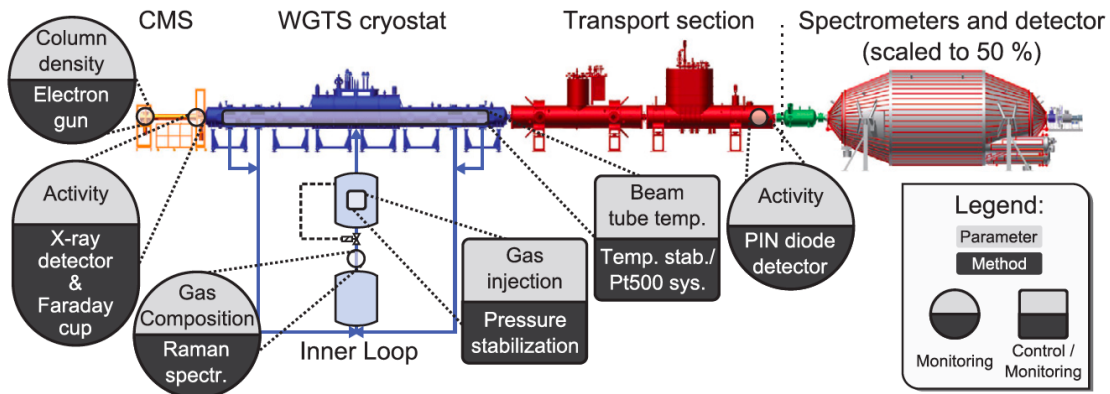
Figure 2.6:   Overview on the source monitoring system. Taken from [Bab12].

advantage of the inelastic Raman effect which is the inelastic scattering of a photon by molecules which are excited to characteristic vibrational and rotational states. For this, light originating from a high intensity 5 W laser with a wavelength of 532 nm, scatters with with a representative sample of the WGTS gas. The wavelength-shifted light (carrying the information of gas composition) is collected under an angle of $90°$ and analyzed by optical spectroscopy to obtain the isotopic composition and the tritium purity. The gas mixture is analyzed both qualitatively and quantitatively with a precision of 0.1 % on a time scale of 100 seconds.

2.3.3   RS e-gun

The rear section electron gun (RS e-gun) is another monitoring system installed in the rear section. The angular-selective e-gun is based on the photoelectric effect and provides a nearly mono-energetic thin electron beam of 1 mm diameter. The e-gun can be operated with two different light sources: a laser-driven light source (LDLS) produces variable wavelengths of about 240 nm to 320 nm and a pulsed laser which provides monochromatic UV light with 266 nm wavelength. The free electrons generated at the gold coated photocathode are accelerated and guided in dedicated electrical and magnetic fields in which the beam can also be directed using a set of dipole magnets.

The column density can be determined with the e-gun by shooting a mono energetic electron beam at $0°$ pitch angle through the gas filled WGTS. The rates of the transmitted electrons are measured at two different retarding voltages. The ratio of these rates can be used to determine the column density with a precision of 0.2 % within 2 minutes. A similar approach is used to determine the energy loss function. For further details the reader is referred to [Bab14]. In contrast to the other monitoring systems the e-gun measurement cannot be combined with regular neutrino-mass data taking. The e-gun measurements are therefore scheduled every 2 hours.
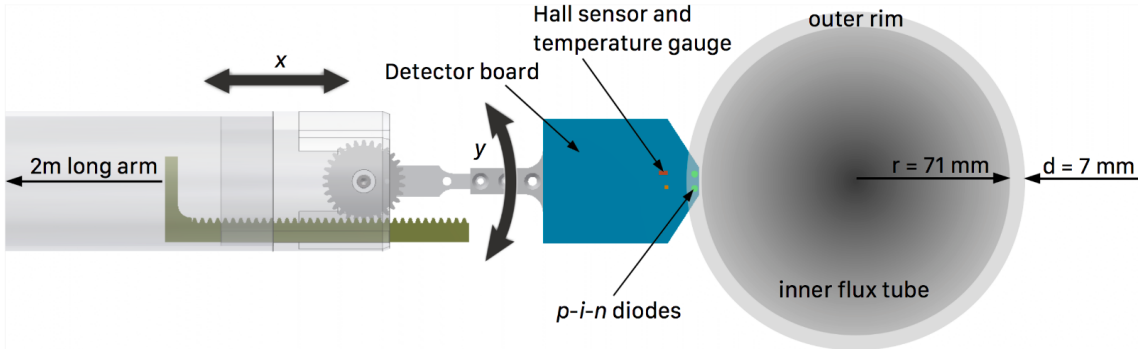
Figure 2.7: The FBM inserted into the electrons flux tube at monitoring position. Two separate drive systems allows the detector board to be moved within the full cross section of the electron flux tube (grey shaded circles, scaled down relative to FBM). For electron detection two silicon *p-i-n* diodes are mounted to the tip of the board such that they can be position into the outer outer rim of the flux tube which is not projected to the main detector (see text for details). Taken from [Are18].

2.3.4   FBM

A further device for monitoring the WGTS activity is the Forward Beam Monitor (FBM) which is installed at the horizontal pump ports of the CPS. Since the FBM forms the central topic of this thesis, it is described in detail in the following sections and chapters.

2.4   The concept of the Forward Beam Monitor (FBM)

As pointed out in Sec.   2.3 it is required to monitor the source properties with 0.1% precision in order to extract the neutrino mass with the target sensitivity of $0.2\,\text{eV}$. The determination of the column density using the e-gun or the focal plane detector requires interruption of the regular neutrino-mass data taking and are therefore planned to be performed only in certain time intervals. The Forward Beam Monitor (FBM) complements the BIXS system, as part of the monitoring system, which measures the source properties continuously. Unlike BIXS, the FBM analyzes the electron flux in the forward direction and directly within the flux tube. The concept of the FBM was first proposed in Ref. [Sch] in which the requirements and the properties such a detector system has to meet is described. The design document includes the basic concept of the mechanical infrastructure, the vacuum systems and the detector itself. In the following three years the FBM prototype was developed by the author of Ref. [Sch08] and the concept was tested and proven. The detector (silicon type) was further developed as described in Ref. [Bab10b] and it was investigated with respect to its (temperature) stability [Bes11]. Before going into the details on the further development of the FBM, its integration into the KATRIN beam line and the results of the first measurements, this section introduces the reader to the topic by depicting the concept of the Forward Beam Monitor.

The main demand on the FBM arises from the precision required for the continuous monitoring of the source properties as pointed out in Sec.   2.3. To detect fluctuations in the

column density with a given precision it is required to measure the electron flux with at least the same precision. (Eq. 2.5). Thus, the event rate must be in order of $O(10^4)$ to achieve the aimed 0.1% precision in less than 100 seconds. Furthermore, the detector must not shadow the FPD so that the regular neutrino measurement is not disturbed. The possibility to reach with the detector any point within the cross section of the flux tube was an additional design goal.

Position		B [T]	D_{full} [cm]	D_{i} [cm]	d_{brim}[cm]
WGTS	nominal	3.6	8.2	9	0.4
	reduced	2.5			
CPS @ FBM	nominal	1.2	14.81	16.21	0.7
	reduced	0.84			

Table 2.1:   Size of the magnetic flux tube and width of the outer rim at WGTS and FBM. Due to conservation of the magnetic flux ($\Phi = A \cdot B = $ const) the size of the flux tube can be calculated for any position in the beam line if the magnetic field is known. The full magnetic flux is $\Phi_{\text{full}} = 229\,\text{Tcm}^2$ but for tritium analysis only the inner flux tube $\Phi_i = 191\,\text{Tcm}^2$ is used. As a result an outer rim of width d_{brim} is formed allowing the FBM monitoring the electron flux without shadowing the main detector. For the first measurements phases the magnets were operated with reduced (70 %) field strengths which does not change the rim size.

The position of the FBM within the KATRIN beam line at the pump port 2 of the CPS (see Fig. 2.2 and Fig. 2.4) was carefully chosen considering the following aspects:

Tritium free environment: Although the FBM is located in the TLK building the region between the cold gate valve of the CPS and the pre spectrometer is already considered to be quasi tritium free. This fact prevents contamination by tritium diffusing into the detector which would reduce the detection capability. Additionally the integration and maintenance of the FBM is facilitated because there are fewer safety requirements to be fulfilled than in tritium bearing components. For example, the FBM only requires a fume hood while the CPS itself is enclosed by a second containment[2]. Although the safety requirements are lower, it is still necessary to perform contamination measurements and supervision by the radiation office if maintaining the FBM after tritium measurements.

Axial symmetric magnetic field: At pump port 2 the magnetic field is axially symmetric because the two magnets mainly creating the field are aligned coaxially unlike the others which are tilted to guide the electrons along the chicanes. Since the intensity of the electron flux is proportional to the magnetic flux it is easier to find asymmetries of the source emission or other unwanted effects in the WGTS or the STS. In Sec. 5.6 the results of the magnetic field measurements and their comparison with simulations will be presented.

Moderate magnetic fields: The continuous source monitoring must be performed at the outer region of the flux tube such that the main detector (FPD) is not covered. This region is called outer rim and only exists because not the full magnetic flux tube

---

[2]Glove boxes are used as secondary tritium containment.

of the source is projected onto the FPD (see Sec. 2.2.1). With the conservation of the magnetic flux

$$\Phi = A \cdot B = \mathrm{const} \tag{2.7}$$

one can calculate the radius of the magnetic flux tube at the FBM position by

$$R_{\mathrm{FBM}} = R_{\mathrm{WGTS}} \sqrt{\frac{B_{\mathrm{WGTS}}}{B_{\mathrm{FBM}}}} \tag{2.8}$$

where R_{WGTS} is the radius of the flux tube in the tritium source at magnetic field strength B_{WGTS}. The moderate magnetic field in pump port 2 of the CPS reaches its minimum in the measurement plane of the FBM (B_{FBM}). The resulting width of the outer rim is about 0.7 mm (compare with Tab. 2.1) which provides sufficient space for the FBM detector. However, during the last measurement campaigns the outer rim appeared to be smaller than expected, probably due to unaccounted collisions of the flux tube with the walls in the source and the transport section. In Fig. 2.7 the flux tube with its outer rim is illustrated including a CAD drawing of the FBM front end as it is in monitor position, measuring the electron flux within the outer rim. The moderate magnetic field also lowers the forces acting on the hardware and possible disturbing influences on the detector electronics.

Beam tube slightly above 77 K: To prevent large temperature gradients the beam tube temperature should be at least at 77 K.

3   The vacuum manipulator

The FBM is designed to measure the electron flux produced in the WGTS (see Sec. 2.2.1) directly in the flux tube, just before it enters the spectrometer section. In order to do this, a detector board will be inserted horizontally into the beam line from the spectrometer sided pump port 2 (PP2) perpendicular to the CPS (see Sec. 2.2.2). Schmitt et al. [Sch] were the first to propose a manipulation mechanism and presented a prototype of the FBM vacuum manipulator in Ref. [Sch08] which was manufactured by an external company. The prototype proved the concept with a positioning reproducibility in a two-dimensional plane which is better than $50\,\mu$m.

However, for the final integration of the FBM into the KATRIN experiment the vacuum manipulator had to undergo several modifications such that almost every part needed to be redesigned and reproduced.

The main reason for these modifications was the increased distance between the FBM and the CPS, compared to the original design, which arose from adding additional vacuum components (TMP, RGA, vacuum gauges and vales) to PP2 (red marked area in Fig. 3.1). This made it necessary to extend the movement range of the FBM and therefore its absolute length by approximately 1.5 m. Additional design changes were necessary because strict material specifications needed to be fulfilled for tritium safety reasons as well as magnetic field and UHV compatibly. These aspects were not fully considered for the prototype.

All vacuum related components of the newly developed FBM were designed and specified in Wuppertal, produced by an external company and temporarily assembled in the laboratory in Wuppertal to further build up and test the system. In Figure 3.8 an overview of these components is given. In the following the same symbols x as in the drawing will be used in the text to ease identifying and locating the hardware parts. All other parts were either manufactured in the local workshops or purchased from external companies.

The first two sections of this chapter describe the principle mechanical setup of the FBM and its further development with the focus on the major modifications which had been done for this work. Section 3.3 begins by introducing the positioning hardware, followed by a brief overview of the FBM's control and interlock system, and closes with an investigation of the positioning reproducibility. In section 3.4 the final integration of the FBM into the KATRIN experiment is presented including the investigation of alignment and absolute positioning accuracy using magnetic field measurements. The vacuum system is outlined in the last section.

3.1   Mechanical setup

The movement of the detector board is realized by combining two linear drive mechanisms. A long stainless steel support tube 106 with an outer diameter of 54 mm and a wall thickness of 2 mm can be driven by 1.8 m along its symmetry axis. At its forward end the detector holder (hereafter know as the "front end", see section 3.2) is attached. The support tube provides space inside for the electrical feeding and a driving rod 108 which can be moved
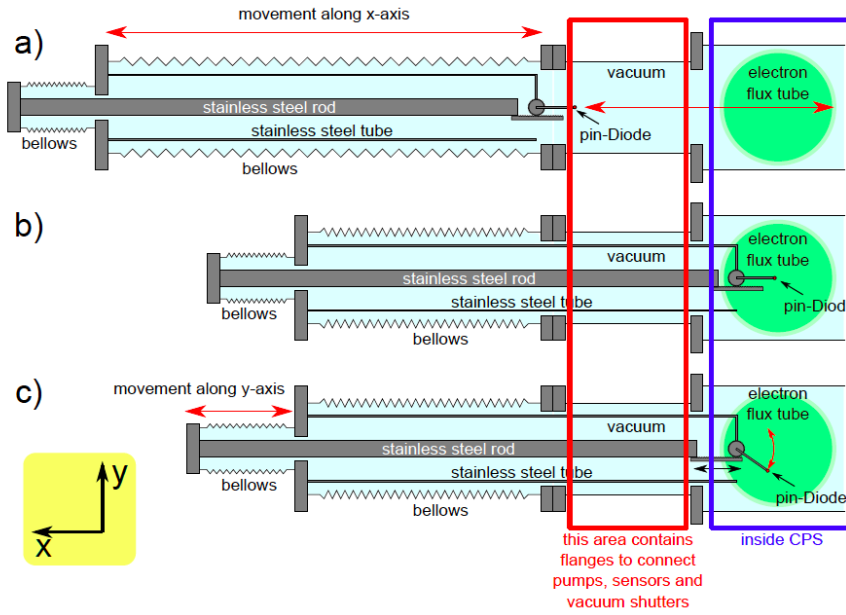
Figure 3.1: Sketch showing the mechanics of the FBM. The p-i-n diodes for the electron detection can be positioned at any point within the electron flux tube (x-y plane, green, normal to this page) with the help of two combined linear drive mechanisms (a support tube and a driving rod inside the tube) where one is converted into a rotary movement with a rack-and-pinion drive. This is an idealized illustration where many flanges and components are not drawn. Taken from [Tep13], changed by the author.

coaxially along the tube by approximately 10 cm. The latter linear movement is converted by the front end into a rotary movement such that the combination of these two movements enable the positioning of the detector board in a two-dimensional plane.

Figure 3.1 shows the principal of the movement mechanism. Two edge-welded bellows 105 and 108 are used to realize the linear movements within vacuum. The large bellows 105 has an unusual long extended length of 2223 mm with a working-stroke of 1800 mm. This is the most delicate and sensitive part of the FBM and requires careful handling. Even the smallest particles inside the ripples of the diaphragms of the bellows can generate strong forces on the material, if the bellows is compressed, and this may lead to micro-leaks. Hereafter the linear movement of the support tube is called "x-movement" and the movement created by the rotary mechanism is called "y-movement" even if the latter is always a combined x-y-movement.

At the rear end of the long tube a DN63 T-piece flange 107 with two DN40 outlets is attached providing the electrical feedthrough as well as the mechanics for the y-movement. The complete rear end's sub-assembly is called "back-end" in the following.

The customized integrated linear unit of the prototype setup for the x-movement was replaced by a 2 m long of-the-shelf variant with spindle drive (slider) featuring a low play, two carriages for more stability, an aluminum shaft housing profile for more compatibility and an integrated end switch. A special slide plate with a DN63 flange holder for the support tube and the long bellows was added to the sliders carriages.
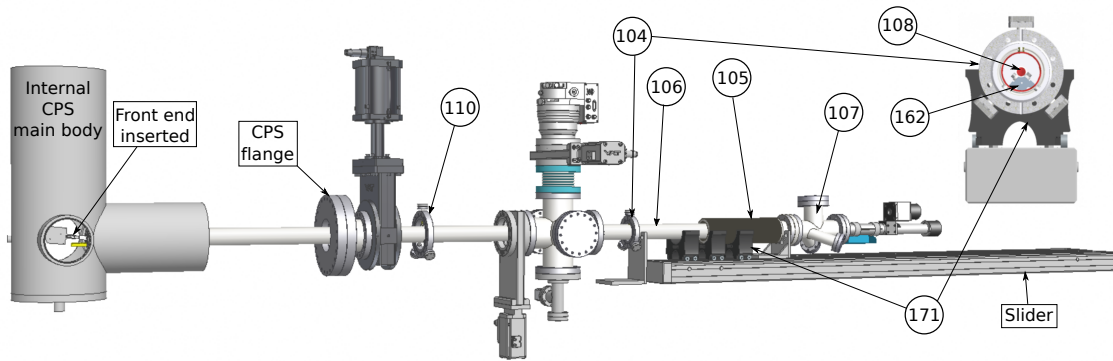
Figure 3.2: CAD drawing of the FBM as it is inserted into the CPS. Parts of PP2 and the CPS and half of the FBM's bellows are invisible for a better illustration of the mechanics. To prevent the tube from hanging down it is supported and led by two supports with ceramic ball bearings 104 110. Also the driving rod 108 is supported inside the tube by two analogous supports 162. The long bellows is supported by three 3D printed trolleys 171 which are automatically pulled along from the bellows.

Due to the elongation of the FBM it was necessary to design and add several supports to prevent the long parts from sagging and hanging down. Three new support types were added to the setup (see Fig. 3.2 for illustration): **(i)** To prevent the driving rod 108 from sagging it is evenly supported at two points. The supports 162 are situated inside the support tube and use ceramic ball bearings to lead the driving rod coaxially to the tube. **(ii)** To prevent the support tube from hanging down if the detector is inserted, an additional support flange 110 (also with ceramic ball bearings) was added close to the CPS. **(iii)** To prevent the new over 2 m long bellows from sagging and hereby grinding onto the support tube three 3D printed trolleys 171 were added which can move freely on the slider and are automatically pulled along from the motions of the bellows. The wagons do not have a fixed path of motion and therefore their positions need to be verified from time to time. Before inserting the FBM they need to be evenly distributed along the slider/bellows and if inserted the wagons should not touch each other. Additionally the bellows' flange holder should not touch the last wagon.

3.2 The front end

The front end of the FBM is the mechanical and electrical connection between the detector and the manipulator. It converts the linear movement of the driving rod into a rotary movement with a rack-and-pinion drive to allow the y-movement. This part had to be redesigned completely because of the following reasons: **(i)** Due to the necessary extension of the FBM the tube must be supported at a second position 110 when the detector is inserted into the CPS to reduce a possible hanging of the detector and the leverage force acting on the first support. The old design of the front end did not allow that since the main body was not flush with the support tube. **(ii)** The new detector board is longer and wider and therefore requires adaptions. **(iii)** The permeability of the old pinion did not fit the specifications.

The front end needs to consist, as with all vacuum components, of low permeability μ_{p}
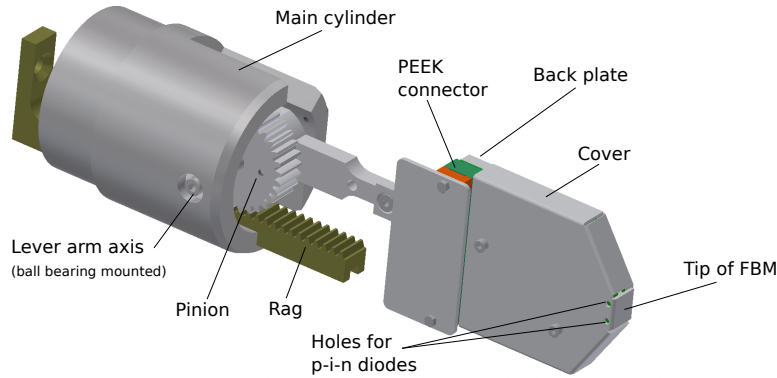
Figure 3.3:   The front end is the mechanical and electrical connection between the detector board and the manipulator. It converts the linear movement of the driving rod into a rotary movement with a rack-and-pinion drive enabling a ±40 degree movement. The main body is flush with the support tube. The materials of the moving mechanism alternate to prevent cold welding (steel, titanium, and aluminum). Including the cover the head of the detector has a width of 50 mm and a lever-arm length of 130 mm. The tip of the FBM is the reference point for positioning.

und vacuum suitable materials. Using materials with high permeability would increase the magnetic force acting on the system and in addition the magnetic flux guiding the beta electrons would get denser and hence more field lines collide with the detector which might remove electrons from the beam. Furthermore it is necessary to alternate the materials of moveable parts to prevent cold welding.

The new front end's cylindrically shaped main body is made of stainless steel 1.4429 ($\mu_{\mathrm{p}} <$ 1.005) and fits now the long tubes outer diameter of 54 mm. To facilitate an easy slipping onto the second support 110 the cylinder has a chamfer at its forward end. Two cut outs extend the movement limits in y-direction and provides space for the electrical feeding. To lead the rack free from play along the pinion a precise groove needed to be added inside the cylinder. Here the correct leading of the rack through the groove is a crucial point. The bottom of the rack, which is made of titanium, was face grinded to find the ideal fitting which allows the leading of the rack without play against the pinion on one side and without clamping, and a minimum of friction in the groove on the other side. To further reduce the friction, lubrication of the groove and the rack was necessary. In UHV applications only dry lubrications can be used because of the strong outgassing of standard lubricants. Therefore ultra low friction dry lubrications is used, which mostly consists of a coating with tungsten disulfide.

The axis of the detector holder is made of steel 1.4429 like the pinion and is ball bearing mounted. These dry full-ceramic ball bearings were not considered for the prototype because they were not available in the required quality at that time. Dry metal ball bearings could not be used because of potential cold welding. The lever arm is made of steel 1.4429 but the detector board holder (back plate) of aluminum to reduce weight. To shield the detector board from radio frequency and, even more importantly, from the electron beam, a steel 1.4429 cover was designed featuring two small holes for the two p-i-n diodes. The full lever arm length from the axis to the tip (including the cover) is 130 mm and the maximum width of the detector equals the width of the cover which is 50 mm.

The electrical connector is covered from the electron beam by a thin steel plate.

3.3   Positioning and controlling

All parts of the actuators are placed outside the vacuum chamber. For each of the drive mechanisms (y, x) a set of one motor and one encoder allow driving and position detection separately.

3.3.1   Motorization

Both drive mechanism are actuated by stepper motors. To guarantee full compatibility with the new controller of the slow control system (3.3.3) the old motors of the prototype needed to be replaced. The new stepper motor for the main spindle works with a holding torque of 12.1 Nm and a smaller one for the driving rod with 2.7 Nm. Unlike the vacuum recipient, the motors are magnetic and external magnetic fields can influence the fault-free operation. Non-magnetic motors utilizing other techniques (e.g. piezo or pneumatic) can not be used because they are either too weak or not precise enough. To minimize the impact of the magnetic stray fields, the motors are attached at positions located as far as possible from the beam axis. From measurements with the old motors [Sch08] an upper limit of 30 mT was determined. This value was confirmed within the present work, i.e. the new motors also work up to this limit. Figure 3.6 illustrates the distances of the whole equipment from the beam axis when the FBM is inserted as well as the simulated and measured magnetic fields. The numerical simulations were performed with the internal simulation framework KASPER [Fur17] of KATRIN and the measurements performed during the first tritium measurement campaign. Both will be discussed in more detail in section 5.6. One can see that the absolute magnetic field at the closer situated y-motor's position never exceeds 2 mT which is well below the limit. The x-motor is attached to the end of the slider and therefore exposed to even lower fields. Hence, no malfunctions of the motor due to the influence of magnetic stray field are expected.

Both motors are not directly acting on the spindle axes but with one stage transmissions using toothed wheels. Since the FBM is not equipped with motor breaks the x-transmission needed to be chosen such that the torque at the motor can withstand the vacuum forces when there is no current in the motor. The transmissions are 19/25 for x and 12/18 for y-direction receptively. Both motors have a resolution of 200 steps per revolution (1.8°).

3.3.2   Position detection

Stepper motors can miss steps without being noticed, thus counting steps is insufficient to determine the position of the detector. To perform the task of position detection independently from the stepper motors, two separate encoders are used. Power cuts can cause a loss of all data, i.e. the counted number of revolutions of standard incremental encoders can get lost. Therefore absolute rotary encoders are used for the FBM because

they always keep the full information of the position even during a power cut which has been tested successfully[3]. These optical encoders work with up to 16-bit single turn and 14-bit multi turn resolution, i.e. 2^{16} steps per revolution and in total 2^{14} revolutions can be counted. This sums up to an overall resolution of 2^{30} steps. The data is transferred via a RS422 interface using the Gray-Code standard. To reduce mechanical play both encoders are connected directly to their corresponding spindle axes. The main spindle has a slope of 2.5 mm, hence a theoretical precision of $10^{-5}\,\mu m$ can be reached. However, due to mechanical tolerances the real precision is significantly lower as it will be described in section 3.3.5.

3.3.3   Control system and interlock

The movements of the FBM are a potential risk for the whole experiment since mechanical collisions can cause internal damage. For example a closing valve when the FBM is inserted or a retraction with a non horizontal lever arm might cause huge damage to the setup. Also a collision of the FBM with the condensed Krypton source (see Sec. 2.2.2) which also uses PP2 to be inserted into the flux tube, needs to be avoided. To avoid such collisions both systems should never be in the CPS at the same time. Hence it is crucial to know the position of the detector at any time and to set movement limits as well as interlock conditions. Therefore hardware switches are applied for x- and y- direction and connected with the valves and the FBM's control system. Furthermore the FBM control system is integrated into the TLK's interlock system.

Switch system

A system of multi-level end switches prevents collisions. The first stage is the evaluation of the switch status by the software of the control system and the second stage directly cuts the power supply for the stepper motors.

For the y-movement three optical switches are attached to the back end limiting the movement range of the lever arm and indicating if it is in horizontal position. Two mechanical end switches are integrated into the slider switching off the motors if the FBM reaches the end of the slider or the CPS. Three optical and three mechanical switches are attached to the moving bellows holder. They indicate the FBM's position between the end switches. Two of them prevent the FBM from being inserted when the valves are closed and the valve from being closed when the FBM is inserted. One switch indicates that the FBM is fully inserted into the beam tube such that pivoting with the detector arm is allowed. At all other x-positions, y-movements are prohibited. The optical switches are connected with the slow control system and the mechanical switches directly (hardwired) with the valves.

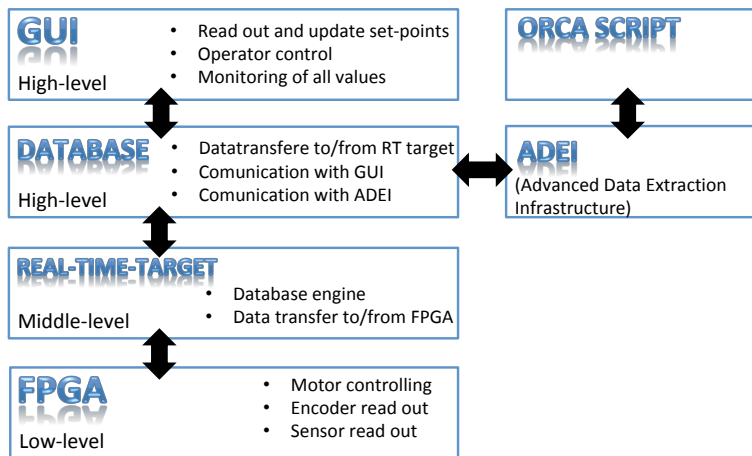[3]Detailed acceptance test protocol available.

Figure 3.4:   The data hierarchy of the control system. The low level is represented by an embedded controller with real-time processor and reconfigurable Field-programmable gate array (FPGA) which runs system-independently and permanently. It includes a full safety retraction of the FBM even when all higher data level have crashed. The middle level provides a database and communication between the high and low level.

FBM slow control system

To fulfill the aforementioned safety requirements a highly stable system needs to be integrated which even keeps on running during a power cut. Hence software based solutions on standard computers have an insufficient reliability. The system needs to read switch and valves statuses, read out the encoder values, control motors, communicate with the global interlock system and provide a database and data access as well as have a safe user interface environment.

In collaboration with the Institute for Data Processing and Electronics (IPE) at KIT a system was integrated which fulfills all needs. An embedded controller with real-time processor and reconfigurable Field-programmable gate array (FPGA) runs system-independently and permanently even during a power cut with the help of accumulators. FPGAs are highly reliable hardware based systems. It represents the low level of the data hierarchy (see Fig. 3.4) and is directly connected with the motor controllers, encoders and sensors. It controls and monitors and also includes a full safety retraction of the FBM even when all upper data level have crashed. The middle level of the data hierarchy is the Real-Time-Target running in a stable Real-Time Linux OS. It provides database functions for reading process values and writing set points and transfers commands and set points from the higher level (GUI) to the FPGA . The GUI (Graphical User Interface) is connected to the database to read and update set-points at the Real-Time Target. The operator can control the system and monitor all values and statuses. The most comprehensive method to control the system is via ORCA (Object-oriented Real-time Control and Acquisition software, [How04]) scripts which are optimized for DAQ and combines slow and run control. In ORCA hardware and DAQ concepts are realized by software objects which are accessible in a graphical user in-

terface. The set-points are updated via ADEI (Advanced Data Extraction Infrastructure) [Chi10].

3.3.4   Positioning theory

When talking of the "position of the FBM", a point on the detector board needs to be defined which represents that "position". For data analysis it would be logical to use the sensor for this reference point but there are three sensors which are equally important. Since for safety reasons the position of the tip of the detector, which represents the end of the FBM, is from importance, the reference point of the FBM is on the symmetry axis and at the end of the detector arm (see Fig. 3.3). The position of this point is given by the following relation:

$$
\begin{pmatrix} x \\ y \end{pmatrix} = \begin{pmatrix} x_0 + N_x s_x + r \cos\left(\alpha_0 + \frac{N_y s_y}{d_0} \frac{2\pi}{n}\right) \\ r \sin\left(\alpha_0 + \frac{N_y s_y}{d_0} \frac{2\pi}{n}\right) \end{pmatrix}
\tag{3.1}
$$

- N_x (Ny): number of revolutions of the spindle

- s_x (s_y): slope of the spindle thread

- x_0: x-direction offset

- d_0: distance between two teeth of the rack

- n: number of teeth of the pinion

- r: length of the detector arm

- α_0: angle offset of lever arm

Note that the x coordinate depends on the y coordinate.

When using rotary encoders (3.3.2) coaxial to the spindles for positioning detection one can determine for $x_0 = 0$ the corresponding absolute encoder value x_0^e and for $\alpha_0 = 0$ (horizontal lever arm) y_0^e, respectively. The number of revolutions can then be written as $N_x = R_x^{-1}(x^e - x_0^e)$ and $N_y = R_y^{-1}(y^e - y_0^e)$ where R_x and R_y are the resolutions (number of steps per revolution) of the encoders. Defining the transition coefficients $T_x = R_x \cdot s_x$ and $T_y = \frac{R_y \cdot s_y}{d_0 \cdot n}$, the coordinates can be written as

$$
\begin{pmatrix} x \\ y \end{pmatrix} = \begin{pmatrix} T_x(x^e - x_0^e) + r \cos\left(2\pi T_x(y^e - y_0^e)\right) \\ r \sin\left(2\pi T_x(y^e - y_0^e)\right) \end{pmatrix}.
\tag{3.2}
$$

Table 3.1 summarizes the relevant quantities to calculate T_x and T_y. The determination of x_0^e and y_0^e is part of the alignment and is described in the following sections. So far the accuracy is determined by the hight resolution of the rotary encoders. However, the play of the mechanical parts and the uncertainties in the alignment will limit the positioning accuracy.

	resolution of encoder	slope spindle [mm]	pitch of rack [mm]	pinion (no of teeth)	Transition $(T_{x,y})$
x	2^{18}	2.5	-	-	$-9.53674 \cdot 10^{-6} \frac{mm}{step}$
y	2^{18}	1	3.14159	30	$2.54313 \cdot 10^{-7} \frac{rad}{step}$

Table 3.1: The necessary quantities to calculate the transition coefficients from encoder steps to x- and y- movement. The motors have different, 100 times smaller transitions and therefore limit the step lengths.

3.3.5   Positioning reproducibility

Positioning reproducibility expresses the ability of the FBM to find a position relative to a former position. This is different to the absolute positioning accuracy which includes external reference points, e.g. given by the KATRIN coordinate system. In particular, the ability to find back to a former position is of crucial importance for the monitoring mode. The reproducibility has been validated twice, once in the Wuppertal laboratory and once in the TLK. In Wuppertal a simple setup with a laser pointer and a mirror was used to increase the accuracy in measuring the angle of the lever arm and hence the y-position. For the x-position a caliper gauge was used to measure the distance between the front end and a fixed reference point in the laboratory. At TLK a portable coordinate measuring machine (CMM) was used to determine both positions.

For the tests[4] moving sequence were carried out which move the detector up and down or forwards and backwards but always come back to its origin. As an example: the detector is moved 1000 motor steps up, 2000 steps down and then 1000 steps up again. Before and after the sequence the position is measured with the aforementioned methods. This was repeated several times and also with different sequence to reduce the statistical and systematic errors, respectively. The positioning reproducibility is expressed by the standard deviation of the mean of reproduced positions. The results are summarized in Tab. 3.2. The error $\tilde{\sigma}_{ymax}$ in the y-position obtained in the TLK deviates from the result in Wuppertal by a factor of 4.4. It is assumed that the measurements with the CMM include a large systematic error because the exact measuring point at the front was difficult to find between each moving sequence. All following magnetic field measurements performed in the CPS (see Sec. 5.4.4 and 5.6) agree with the smaller error obtained in Wuppertal which was also expected from the specifications of the prototype. Therefore the positioning reproducibility of the FBM is better than 0.1 mm for both directions.

3.4   Mechanical integration and alignment

The necessary makings for the mechanical integration of the new FBM were done by the modifications described in section 3.1. Figure 3.5 shows the FBM as it is attached to the CPS. The additional vacuum components which are attached to the PP2 (and which caused the extension of the FBM) close with a DN100 gate valve which is there to separated the

---

[4]Detailed acceptance test protocol available.

Measurement	σ_x[mm]	σ_α[°]	$\tilde{\sigma}_{ymax}$ [mm]	$\tilde{\sigma}_{xmax}$ [mm]
Wuppertal	0.015	0.03	0.07	0.042
TLK	0.018	(0.138)	(0.312)	(0.180)

Table 3.2: The positioning uncertainties determined with two measurements with different methods. The uncertainties in both directions generally depend on the angle of the lever arm. For simplicity the upper maximums $\tilde{\sigma}_{ymax}$ and $\tilde{\sigma}_{xmax}$ are given. The values in brackets include unknown systematic uncertainties and therefore should not be used (see text).

FBM from the PP2 volume. These vacuum components are supported by a separate stand (stative) which also serves as the support for the FBM six-way cross, the TMP 119 and the FBMs gate valve 140. The FBM itself is supported by a profile stand and connected with the small bellows 103 to the six-way cross as vibration insulation. The DN100 distance flange 110 with the additional ball bearing support is positioned close to the CPS valve (compare Fig. 3.2). The beam line and therefore the main axes of the FBM and PP2 is situated at a height of approximately 1.8 m from the uneven floor.

As shown in section 3.3.5 the FBM is able to find relative positions in a plane with a precision of less than 0.1 mm. However, this section is about the absolute alignment of the FBM manipulator in relation to the KATRIN coordinate system, to the CPS, and to the magnetic flux tube. The last three are not necessarily the same since the alignment of the CPS has uncertainties as well as the flux tube's position which is determined by the alignment of the WGTS and the solenoids which create the magnetic field in PP2. A global frame is given by the KATRIN coordinate system (x_k,y_k,z_k) which has its origin in the analysis plane approximately in center of the main spectrometer (see Sec. 2.2.3). The center of PP2 of the CPS, where the FBM is connected normal to the beam line, is located at $z_k = -18.27535$ m.

For the alignment a portable coordinate measuring machine (CMM) was provided by TLK. With a CMM it is possible to perform a three dimensional analysis of the FBM setup to find the position of single points, planes or axes of flanges with a precision better than 0.1 mm. Prior to measurements, the CMM is calibrated to the KATRIN coordinate system with a set of four reference points which are installed in the laboratory at several locations.

y,z-**alignment** The FBMs main axis needs to match the axis of the vertical PP2 at $y_K = 0$ mm and $z_K = -18.27535$ m. The main axis is defined by the axis of the support tube 106. At its rear end the support tube is welded to a distance flange which is supported from the outside by a flange holder which is connected to the linear unit (compare Fig. 3.2). During operation a second support is provided by ball bearings which are installed in a distance flange 110 behind the second six-way cross to hold the long tube coaxial during movements. These two flanges are the only two points supporting the FBM during operation, hence for the alignment they need to be coaxial to vertical PP2 at all times. During movements of the FBM along the x-axis using the linear unit the FBM must not move its main axis. Consequently the slider must be parallel to the x-axis and perpendicular to the z-axis.

part (fl.-=flange)	Δz [mm]	Δy [mm]	x [mm]	σ [mm]	encoder value
CPS fl. big	-6660.38	-1.26	-	< 0.10	-
CPS fl. small	-6660.05	-1.34	-	< 0.10	-
support fl. big	-6660.24	-1.03	-	< 0.10	-
support fl. small	-6660.48	-0.93	-	< 0.10	-
fl. long tube	-6660.97	-0.98	-	< 0.10	-
slider back	-6736.39	-103.13	-	< 0.50	-
slider front	-6736.55	-102.39	-	< 0.50	-
front end	-	-	1572.46	<0.28	578191798
slider end	-	-	2000,745	-	-
fl. holder back	-	-	4256.718	<0.50	-
fl. holder front	-	-	1916.662	<0.50	-

Table 3.3:   Deviation of the alignment from the specified values. The errors are upper estimations including the main uncertainty of the CMM by measuring a single point and the uncertainties in the alignment of the CMM to its reference points which was specified to be less than 0.5 mm. Errors can be reduced by using more then one measuring point. The misalignment in y-direction of approximately -1 mm is caused by the deviations of the big support tube holder and the slider .

x- alignment   For the alignment in x-direction the CMM was used to determine the position of the tip when the FBM is in the six-way cross with a horizontal lever arm.

Table 3.3 lists the deviations of the alignment from the upper specification.

With the errors of the alignment and the errors of the reproducibility measurements in Sec. 3.3.5, an overall error can be calculated using standard error propagation. The result is given in Tab. 3.4. When former alignment is done and the lever arm is set to zero angle the corresponding encoder value y_0^e relates to $y_{FBM} = 0$ mm.

	$\sigma_{aligment}$ [mm]	$\tilde{\sigma}_{max}$ [mm]	σ_{full} [mm]
x	0.28	0.042	0.28
y	0.1	0.07	0.13

Table 3.4:   The precision of absolute positioning results from the combination of the uncertainties of the alignment and the positioning reproducibility. The alignment error dominates the precision for the x-direction but this can be optimized in future.
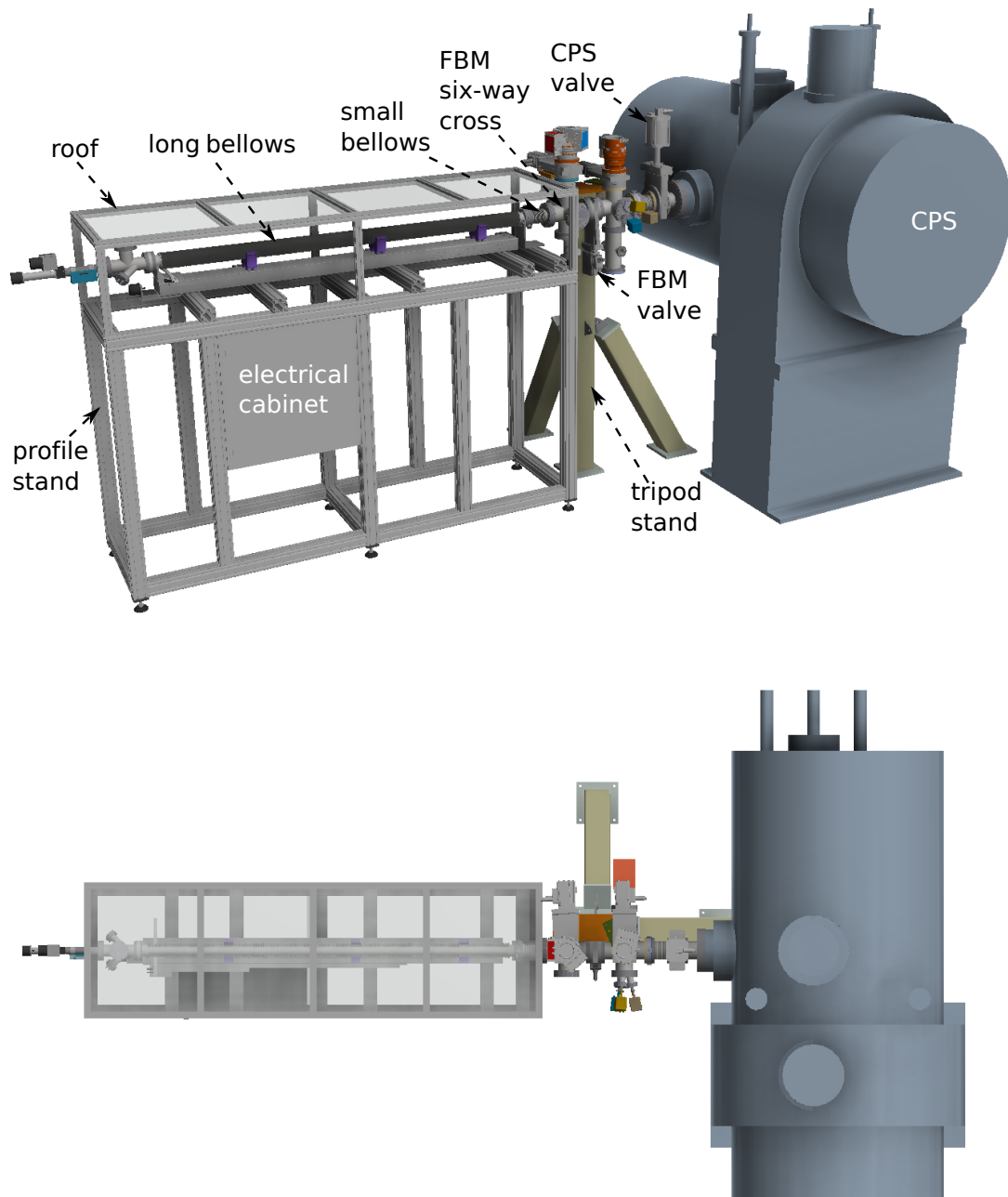
Figure 3.5: In this CAD drawing the FBM is shown as it is attached to the CPS. The FBM six-way cross, valves and TMP are supported by a tripod stand which also serves as the support for additional vacuum equipment such as pumps and a residual gas analyzer. The FBM is installed on a profile stand which also features a roof to prevent dirt from falling into the bellows. The manipulator is connected to the FBM six-way cross via the small bellows which serves as vibration insulation.
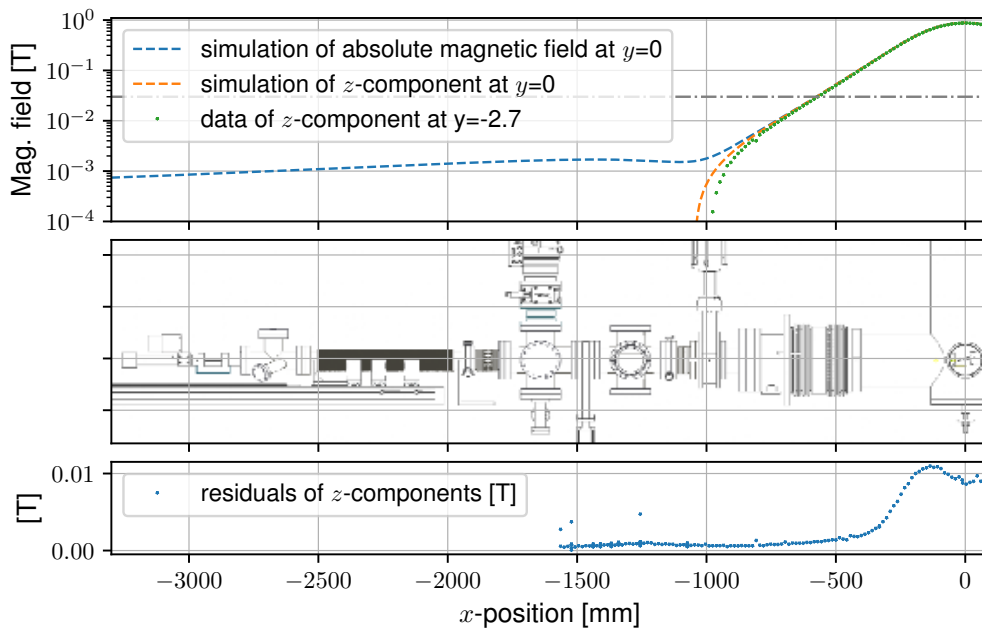
Figure 3.6: Measured and simulated magnetic field along the x-axis. The middle panel shows the positions of the hardware components within the magnetic field. Motors, encoders, TMP, valves and vacuum gauges operate in a magnetic field of less then $2\,\text{mT}$ such that no malfunctions due to the impact of the field are expected.

3.5 Alignment with magnetic field measurements

The FBM is the only device in KATRIN which can perform measurements directly within the flux tube. Therefore the detector board is equipped with a 1D Hall sensor which is there to measure the z-component of the magnetic flux tube directly within the CPS. These measurements are important for the FBM commissioning since it enables alignment relative to the magnetic flux tube and hence to the actual hardware, i.e. the magnets and the CPS. Additionally, magnetic field models can be validated. In this section the magnetic field data is only used for alignment and to determine the field strength in which the FBM hardware operates. A more detailed analysis on the data including the comparison to simulations is carried out in section 5.6.

Horizontal scan

Around the flux tube a magnetic stray field is built up which might influence the functionality of external components. This is of particular importance for the stepper motors and the TMP but also in general for ferromagnetic components which experience magnetic forces. Therefore simulations were carried out for the z- and x-components within the field. The y-component is negligible in this picture. Figure 3.6 shows the simulated and measured magnetic field as well as the positions of the external components. The Hall sensor can only measure the z-component which is the strongest up to $800\,\text{mm}$ radial distance from the beam axis. The probe only reaches positions up to approximately

$x = -1500\,\text{mm}$. Simulation and data agree well within the range of the Hall sensor and the simulated magnetic field at the TMP and the y-stepper motor is less then $2\,\text{mT}$ which is within specification. None of the devices have shown any malfunction during several weeks of operation in the fields.

Full scan

The strength and the position of the magnetic field in CPS is mainly determined by the magnets no. 6 and no. 7. These fields can be considered as stationary because the currents through the magnets can be kept stable to a high level. On the other side these fields can be measured very precisely with the Hall sensor on the detector board. With the following method the relative positioning between the magnetic flux and the FBM can be derived from the full (2D) scans. Of even greater importance is, that the encoder value for a horizontal lever arm y_0^e can be determined easily and precisely.

The shape of the magnetic flux can be described by a two-dimensional Gaussian. Open fit parameter in a global fit are the encoder value for the horizontal lever arm y_0^e , a possible offset (x_0, y_0) of the magnetic flux to the FBM system, the widths (σ_x, σ_x) of Gaussian and the maximum magnetic field B_0 in the center. The fit function is given by

$$B = B_0 \left(\exp\left(\frac{(x_h - x_0)^2}{2\sigma_x^2} \right) + \exp\left(\frac{(y_h - y_0)^2}{2\sigma_y^2} \right) \right) \tag{3.3}$$

with the coordinates x_h and y_h off the Hall sensor given by equation 3.2, but corrected by the offset of the sensor from the tip. In Fig. 3.7 the data and the fit of one of the scans can be seen as an example. The data was calibrated [Sch17] and temperature corrected (see Sec. 5.7). Table 3.5 shows the results of four scans which have been performed at different times.

3.6   Vacuum system and compatibility

While in the main spectrometer an ultra-high vacuum (UHV) with less than 10^{-11} mbar is reached, the CPS still reaches pressures in the 10^{-10} mbar regime. For reaching these pressures a combination of turbo molecular pumps (TMP) and non-evaporable getter pumps (NEG) [Are16] are used. The FBM is connected to the PP2 of the CPS but can be separated from the CPS volume by a UHV gate valve 101. Before opening the valve the pressure in the FBM volume needs to be comparable to the pressure in the CPS. The reasons for that are as follows:

1. The valve cannot be opened at a pressure difference above $30\,\text{mbar}$ which is a hardware limitation implemented by the producer.

2. A possible high gas load from the FBM stresses the NEG pumps and the argon frost layer which would require a shorter maintenance cycle of these systems.
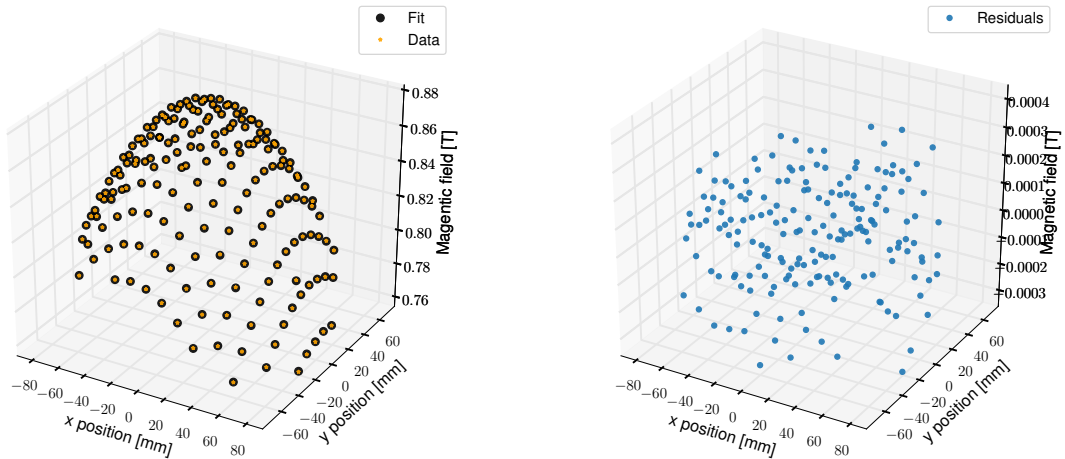
Figure 3.7: The left plot shows the calibrated and temperature corrected magnetic flux data measured with the Hall sensor and the fit result. The right plot shows the residuals from the fit.

After opening the gate valve the TMP of the FBM is separated with another gate valve 140 from the system for safety reasons. The final pressure of the FBM which is needed to be reached before opening the valve is specified to 10^{-9} mbar.

Outgassing test

One of the major concerns for vacuum processing equipment designed to reach the UHV range, is the outgassing from the walls of the vacuum chamber and its containing equipment. Whenever a vacuum system is exposed to air, the internal surfaces will be covered with layers of water molecules. Also dirt (e.g. from finger prints) and the outgassing of other molecules with a low boiling point (such as hydrocarbon) increases the amount of residual gas. These effects increase the gas load, which is given in $\text{mbar} \cdot \text{l} \cdot \text{s}^{-1}$, and which is a quantity for the number of molecules entering the volume. Also leaks add to the gas load. The TMP removes the molecules with its pumping speed given in $\text{l} \cdot \text{s}^{-1}$. A rough estimate of the end pressure which can be reached can be given by the ratio of gas load and pumping speed.

Leak tests with a helium leak tester show that the FBM setup has a integral leakage rate of $< 1 \times 10^{-8}$ mbar l/s. This leakage rate is relatively high for UHV applications but still negligible compared to the outgassing rate which is shown next.

The gas load is determined with the Rate-of-Rise method by which the pressure rise after separating the TMP from the volume is investigated. If the TMP does not remove molecules anymore the pressure rises because of the gas load. The slope of the curve multiplied by the volume of the recipient represents the degree of gas load. The results given in Tab. 3.6 show that the leakage rate but also the outgassing rate from the stainless steel surfaces, which is typically less than 10^{-8} mbar $\cdot$ l/s, can be neglected. The main source of the gas load is expected to originate from the detector board. The SMD parts have plastic casings which likely contribute the most to the overall gas load. Dedicated outgassing tests

Name	Date	Run	I_{mag} [A]	Prespec.	T_{det} [°C]	Comment
Sim50	2017/07/19	N/A	99.8 ($\triangleq$ 50 %)	On	0.5	
Sim70	2017/07/19	N/A	139.6 ($\triangleq$ 70 %)		0.5	
FirTri	2018/07/15	346	139.6 ($\triangleq$ 70 %)	On	−15.5	
EnW	2018/07/30	N/A	139.6 ($\triangleq$ 70 %)	On	38.2 to 33.8	Cooling down
EnK	2018/08/08	N/A			−13	

Name	B_0 [mT]	x_0 [mm]	y_0 [mm]	σ_x [mm]	σ_y [mm]	y_0^e []
Sim50	617.99(1)	−1.390(9)	3.408(41)	176.97(4)	179.23(9)	628402440(1341)
Sim70	863.93(2)	−1.167(9)	3.49(4)	175.54(4)	177.00(9)	628400841(1412)
FirTri	879.96(2)	−1.08(1)	3.69(4)	174.94(4)	175.10(6)	628442371(1279)
EnW	872.77(3)	−0.27(2)	4.34(8)	175.2(1)	176.1(1)	628371029(2718)
EnK	874.03(3)	−0.15(1)	4.34(5)	175.08(6)	176.18(8)	628423287(1707)

Table 3.5: The results from 2D Gaussian fits of data from different magnetic field scan. The currents of the CPS magnets I_{mag} are listed as well as the FBMs board temperature T_{det}.

[Bab10b] with an earlier version of the detector board came to the same result. Further strong contributions probably originate from the lead and the adhesive.

measurement	P_i [mbar]	P_e [mbar]	Δt [h]	gas load [mbar·l/s]
1	9×10^{-8}	1.6×10^{-3}	1	6.7×10^{-6}
2	3.6×10^{-8}	1×10^{-3}	1	4.3×10^{-6}

Table 3.6: Gas load of the FBM calculated with the Rate-of-Rise method. The pressure rise after separating the TMP from the system is measured for one hour. The rate of rise (given in mbar/t) multiplied by the volume of the vacuum recipient represents the degree of gas load.

Pumps For the layout of a pump system the desired end pressure and pump down time need to be specified as well as the surface area A and the desorption rate $q_{des,M}$ of the materials used need to be known. Typically, the largest fraction of the pump down time is caused by the continuous desorption of molecules and atoms from the surfaces which need to be removed by the TMP. The approximate volume of the FBM vacuum chambers is 15.13 l and consists mainly of steel with $q_{des,M} = 2.7 \cdot 10^{-4} \, \mathrm{Pa\,m^3\,s^{-1}\,m^{-2}}$. The TMP has a pumping speed of 300 l/s and to reach the final pressure of $p_f = 10^{-9}$ mbar a time of

$$t_{des} = \frac{q_{des,M} \cdot A \cdot t_0}{S \cdot p_f} = 2.67 \cdot 10^6 s = 741 \, \mathrm{h} \qquad (3.4)$$

is needed. The forepump is an oil free (dry) multi-stage Roots pump with a pumping speed of maximum $28 \, \mathrm{m^3/h}$.

Materials Besides the outgassing problematic, also the use of magnetic fields and the tritium usage give further material requirements. Only materials with a permeability

very close to 1 reduce the magnetic force acting on the setup and minimizes a change in the fields. Since the FBM is measuring directly in the beam, the latter is of greater importance than for other systems. The vacuum chamber is mainly made of 1.4429-ESU (316 LN) steel which has a lower permeability (≤ 1.005) then standard stainless steels. The driving rod and the back plate are made of aluminum and the rack of titanium. The detector board is made of polyimide.

Out baking

Below a pressure of 10^{-4} mbar surface outgassing becomes the dominant effect for the pump down time. Here the desorption rate of water from the stainless steel surfaces of the recipient is the most prominent part. The TMP can only remove molecules which are close to it in the volume of the recipient but due the permanent outgassing new molecules reach the volume. The outgassing rate drops very slowly, hence depending on the amount of surface the pump down time can take very long, up to timescales of days, weeks and even months. Out baking of the vacuum parts increases desorption and diffusion rates in the chamber and reduces significantly the pumping times to days.

The largest surface area is the long bellows 105. Additionally, the shape of the bellows and the small distance to the support tube 106 causes low conductivity for molecules, which increases the pumping time, too. Standard heating cables or belts can not be used because of the difficulty of putting them on, the difficulty of maintaining homogenous temperatures and the danger of adding dirt which might remain in the ripples of the diaphragms and cause damage when the bellows is compressed again. Therefore a customized heating collar was purchased which perfectly fits the bellow and heats it homogeneously. The bellows must be relaxed or slightly extended for the procedure. Before putting on the heating collar, it is recommended to put a sheet of standard tinfoil around the bellows to cover it from dirt. The front part (six-way cross and short bellows) and back end of the FBM can be baked out with standard heating cables and sheets of tin foils for insulation. The back end, long bellows and front part can be set to different temperatures. To find the right temperature configuration one needs to consider the following: **(i)** The higher the temperature the shorter the pumping time but from TLK regulations the upper limit is 200 °C **(ii)** Maximum temperature allowance for the detector board (120 °C), the bellows (150 °C), the TMP and vacuum gauge flanges (35 °C and 80 °C) should never be exceeded. **(iii)** The bake out temperature must be a gradient from the back to the front towards the TMP to further reduce pumping time.

To find the right configuration a test was performed at BUW. The heating devices were set to the following values:

- $T_{back} = 170$ °C (cable)

- $T_{bellows} = 150$ °C (heating collar)

- $T_{front} = 90$ °C (cable)

The heating collar and cables have their own temperature gauges for regulating the heat. Additionally five temperature gauges were attached to measure the temperature at the

time [min]	Back [°C]	Bellow [°C]	Slider [°C]	TMP [°C]	Gauge [°C]	Board [°C]
0	22.0	23	21.2	23.3	24.1	37.2
10	199.4	157	25.2	23.9	24.8	37.4
20	>200	152	27.8	25.7	26.9	39.0
30	191	153	28.5	26.7	28.9	41.4
40	186	154	28.7	28.3	30.6	43.7
70	193	162	29.2	32.6	34.5	49.5
130	190	148	30.3	35.9	37.9	56.7
250	197	159	30.8	36.9	39.3	63.5
430	190	154	31.1	37.1	39.7	66.6
>490 equilibrium	194 ± 6	155 ± 5	30.4 ± 0.4	37 ± 0.1	40.6 ± 0.6	67.0 ± 0.1

Table 3.7: The temporal temperature profile and maximum temperature of the critical components during back out. The set temperatures are $T_{back} = 170\,°C$ (cable), $T_{bellows} = 150\,°C$ (heating collar) and $T_{front} = 90\,°C$

critical points of the setup plus the sensor on the detector board. Because the heating collar touches the slider it is also monitored. Table 3.7 lists an excerpt of the time dependent temperature development and in the last line the mean value over 3.5 hours after reaching the equilibrium (after approximately 7 hours). The slider, vacuum gauge and the detector board are well bellow their hardware limits. The TMP temperature exceeds the limit by two degrees but the temperature gauge was conservatively close to the flange such that the actually TMP temperature is expected to be lower. The temperature at the back end occasionally exceeds the TLK limit but that is just because of the temperature oscillation due to the control mechanism, the mean temperature is within the limit. The temperature of the bellows is $5\,°C$ higher than allowed.

This test is to be redone at TLK since the new detector board has a higher thermal conductivity and likely will become warmer, although not much warmer. It is proposed to reduce the set temperatures of the bellows and the back end by $5\,°C$.
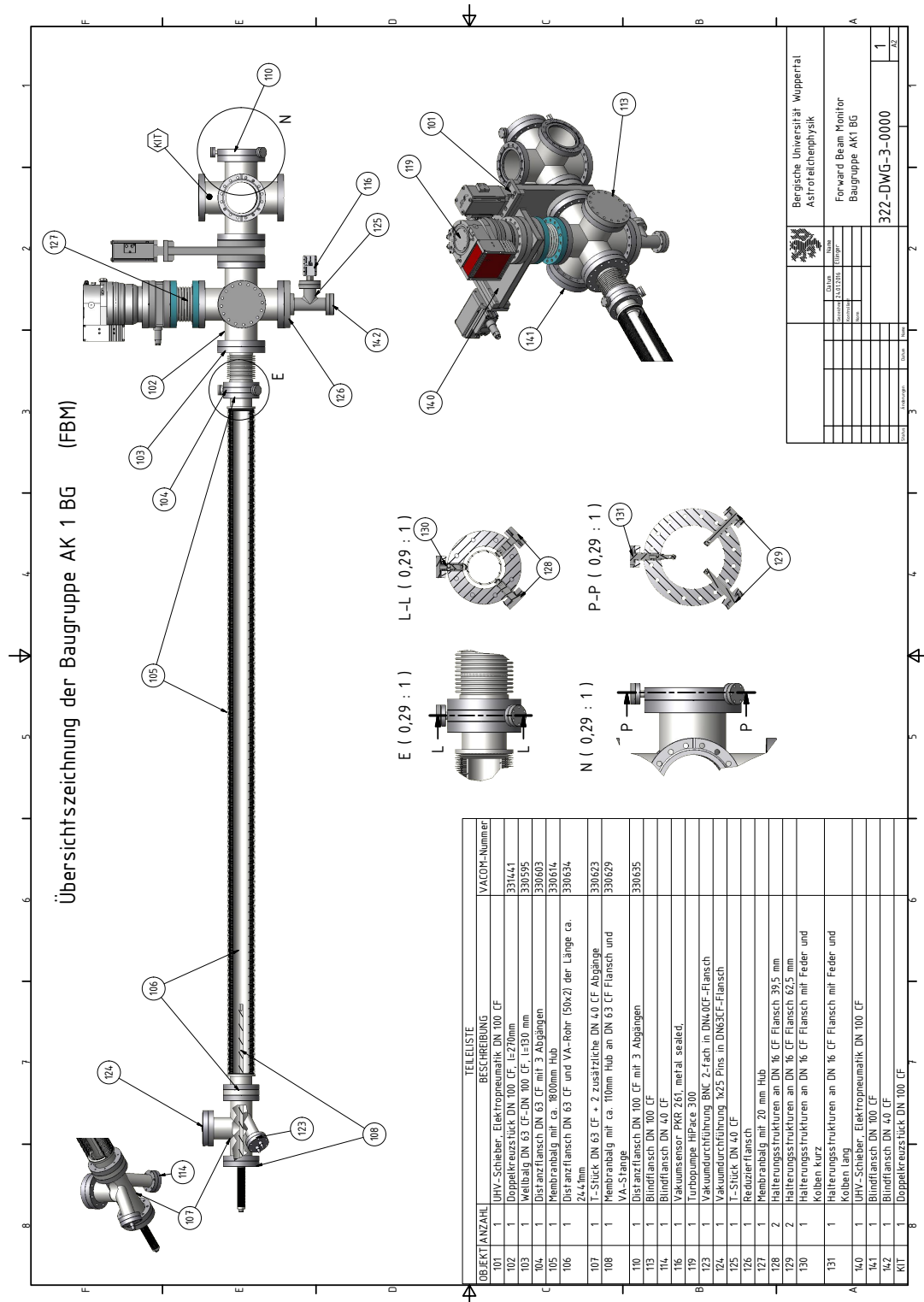
Figure 3.8: General layout drawing of the requirement class 1 (AK 1) sub-assembly. The AK 1 contains all parts that separates the vacuum volume (which potentially can be contaminated with tritium) from the atmosphere (the laboratory), e.g. the vacuum recipient and the pump. The rod and the front end are not part of AK 1 and therefore not shown. The second (right) six-way cross is provided by the KIT und just displayed because of position 110 which is attached to it.

4   Detector

The main task of the FBM is to monitor the electron flux within the electron beam and to obtain the beta spectrum of tritium. Silicon detectors provide a large range of applications for particle detectors. For the FBM, detector chips with a thin entrance window (dead layer) are needed to allow the detection of electrons with energies below 10 keV. In addition they must also allow detection of low energy photons which is important for calibrating the detector. In Ref. [Bab10b] and [Sch08] the basic preamplifier circuit was developed in cooperation with the IPE and a prototype detector board was tested successfully. However, a suitable detector chip as well as the final layout of the detector board were open issues. For this work several silicon detectors were tested, and based on the existing preamplifier circuit, a new two-channel detector board was developed, including additional sensors and a UHV compatible electrical connector.

The first section 4.1 of this chapter gives a brief overview of the interaction of ionizing radiation with matter which is important for understanding the detector response and for performing simulations. In the following sections the working principle of silicon detectors (4.2) and signal processing (4.3) are introduced with focus on the detector chips and DAQ used for this work. Section (4.5) describes the development of the new detector including the detector chip, the board, the electrical connector and feeding. The final section 5.2 presents the evaluation of the detector properties as energy resolution, efficiency and dead layer thickness and closes with the temperature dependence of these parameters.

4.1   Interaction of radiation with matter

Ionizing radiation interacts with matter in several ways resulting in electrical, optical or thermal signals. For the present work, only photons with energies below 60 keV and electrons with energies below 20 keV are of interest. The cross sections for each interaction process depends on the particle's energy E_x ($x = \gamma$, e^-) and the atomic number Z of the target material. Each primary interaction can produce further secondary particles. Hereafter the incident particles (photons, electrons, etc) are called "primary" particles and particles created within interactions, "secondary" particles.

4.1.1   Photons

Photons in the energy range, as mentioned above, interact with matter via Compton and photoelectric effect. Electron-positron pair production is not expected in the FBM as the photons do not reach the minimum energy of 1.024 MeV, and thus is not discussed.

Compton effect: When a photon interacts with free electrons or loosely bound outer-shell orbital electrons of an atom it can get scattered. In this inelastic scattering process the wavelength λ of the scattered photon increases and hence the energy of
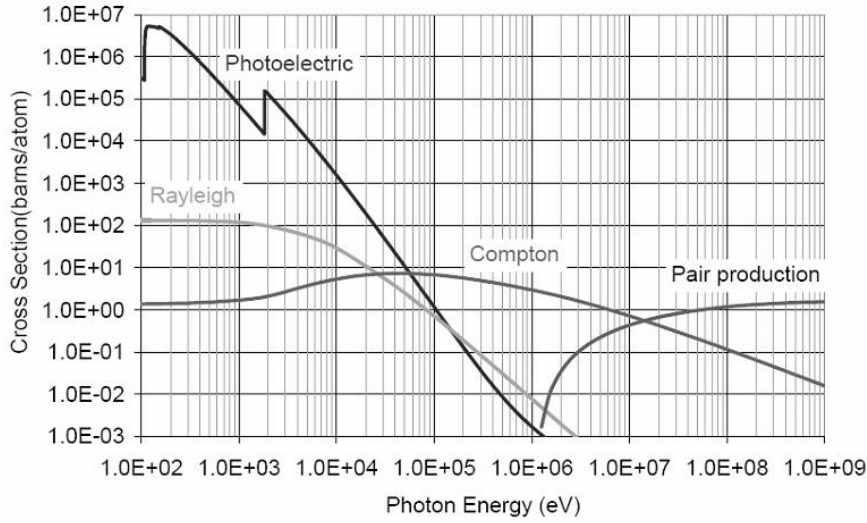
Figure 4.1: Partial cross sections of photoelectric absorption, Compton scattering and electron-positron pair production in silicon as a function of energy. For photon energies below 60 keV, the photoelectric absorption is the dominant effect. This plot is taken from [Wro05].

the photon $E = \frac{hc}{\lambda}$ is lowered. The total energy and momentum are conserved in this process. The transferred energy

$$\Delta E_{(\phi)} = \left(1 - \frac{1}{1 + \frac{E_\nu}{m_e c^2}(1 - \cos(\phi))} \right) \tag{4.1}$$

depends on the scattering angle ϕ and is therefore continuous. Here E_ν is the primary photon energy. Taking into account that the electrons are loosely bound (ionization energy $W_A \sim O(100\,\text{eV})$), the energy is transferred almost completely into kinetic energy. The cross section of the Compton effect depends on the energy of the incident photon and is linear to the atomic number Z of the given target material.

Photoelectric effect: The Photoelectric effect describes the process where the full energy of the incident photon is transferred to a shell orbital electron of an atom. The photon effectively disappears and transfers both its energy and momentum whereas the nucleus acts as the third scattering partner. The energy carried away by the electron equals the energy of the photon minus the binding energy of the electron. The probability for the Photoelectric effect depends on the photon energy and is proportional to the third to fourth power of the atomic number, Z^{3-4}.

In Figure 4.1 the interaction probabilities for each channel in silicon as a function of photon energy is displayed. Secondary electrons from the primary interaction will undergo further scattering processes as described below.

48

4.1.2 Electrons

Unlike low energy photons, electrons lose their energy in matter in many subsequent inelastic interactions. This is a result of a larger cross section in combination with a smaller energy loss per collision. For example the mean free path of 10 keV electrons is only $\lambda \approx 10\,\text{nm}$ [JP99]. For photons the mean free path is about 100 to 1000 times larger then for electrons. The mean energy loss per distance travelled (or stopping power) of electrons is described by the Bethe formula with correction for slow electrons [Tan18]:

$$
\begin{aligned}
-\left\langle \frac{dE}{dx} \right\rangle =\, & 2\pi N_A r_e^2 m_e c^2 \rho \frac{Z}{A} \frac{1}{\beta^2} \left[\ln\left(\frac{m_e c^2 \beta^2 \gamma^2 T_{max}}{2I^2} \right) \right. \\
& \left. + (1-\beta^2) - \frac{2\gamma-1}{\gamma^2}\ln 2 + \frac{1}{8}\left(\frac{\gamma-1}{\gamma}\right)^2 - \delta \right]
\end{aligned}
\tag{4.2}
$$

where

$N_A:$	Avogadro's number
$r_e:$	Classical electron radius
$m_e:$	Electron mass
$\rho:$	density of absorber (for silicon $2.336\,\text{g/cm}^3$)
$Z:$	Atomic number of absorber
$A:$	Atomic mass of absorber
$c:$	Speed of light
$v:$	Speed of incident particle
$I:$	Mean excitation energy (for silicon $172\,\text{eV}$)
$T_{max}:$	Maximum imparted kinetic energy
$\delta:$	Density effect correction
$\beta=$	v/c
$\gamma=$	$1/\sqrt{1-\beta^2}$

As a result of the large cross section the following substantial differences between electrons and photons are important for detector applications:

- The interactions of electrons take place within the first μm of the detector material while photons can interact through the whole volume.

- The possibility detecting an electron entering the detection volume is generally much higher than for photons, which may leave the detection volume without performing any interactions. Hence the detection efficiency for electrons is higher.

- Electrons interact with significant probability already in the non-sensitive region of the detector. This region is called the "dead layer" and forms the entrance window of the detector. It mainly consists of a silicon dioxide layer (which is either a result
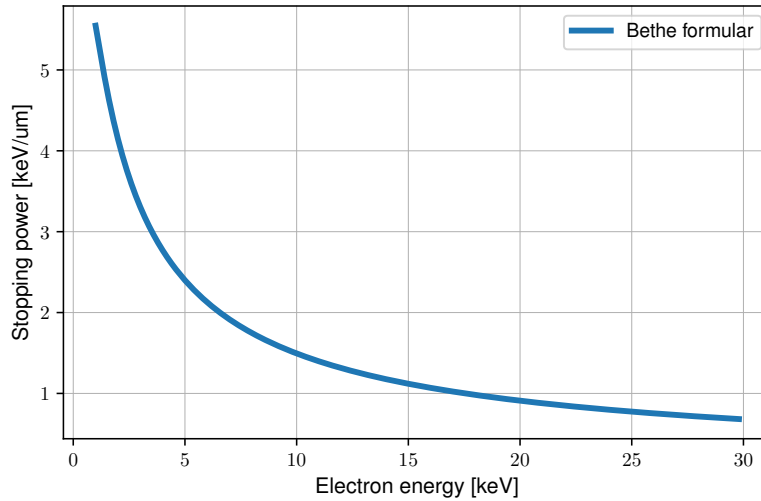
Figure 4.2:   Stopping power of low energy electrons in silicon calculated with the Bethe formula.

of natural or induced passivation) and a doped layer of the diode (compare with Fig. 4.4). The interactions in the dead layer result in the non-detection of electrons or in detections at lowered energies, thus modifying the observed spectrum.

- A significant fraction of electrons are reflected from the entrance window of the detector.

4.2   Silicon detectors

Semiconductor detectors are commonly used in particle and nuclear physics since they have a better energy and spatial resolution compared to other types of detectors, e.g. gas ionization chambers. However, they effectively function as ionization chambers. Particles penetrating the detection volume deposit their energy by creating positive and negative charge carriers which are guided under an applied electric field to the electrodes where a change in charge is induced. The key is to create a so-called reverse-biased p-n-junction. Silicon is a group 4 semi conductor and has a band gap of 1.11 eV at room temperature. The conductivity of intrinsic silicon is too small for detector appliance but it can be increased by introducing controlled impurities into the crystal, a procedure called "doping". By replacing a silicon atom by a group 5 atom (n-doping) one valence electron is left without a partner. The bound level of this donor electron is approximately 0.01 eV below the conduction band and can easily be introduced into it at room temperature ($E = 0.026$ eV). Replacing a silicon atom by a group 3 atom (p-doping) leaves an unpaired silicon bond whose bound level is above the valence level also by approximately 0.01 eV. At room temperature electrons from nearby atoms fill a substantial fraction of these levels and leave mobile quasiparticles (acceptor holes) in the valence band.
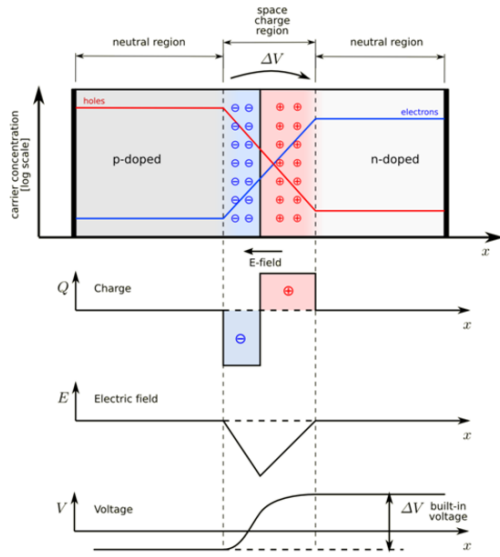
Figure 4.3:   Illustration of a *p-n*-junction with zero bias voltage in thermal equilibrium. By thermal diffusion free charge carriers from the p-region (n-region) are driven to the n-region (p-region) where they recombine. The result is a positive (light red) and negative (light blue) space charged region. The resulting potential is called "built-in" potential of the diode. Taken from [Adu].
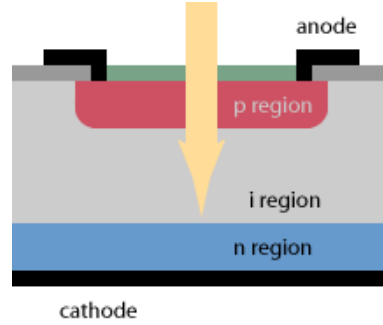
Figure 4.4:   Schematic of a *p-i-n* photodiode. A *p-i-n* diode comprise a third, intrinsic region located between the n- and p-region of a common *p-n*-junction. Photons (or electrons) enter the entrance window (green and p-region) and create electron-hole pairs also in the i-region. The created charge carriers are guided under an applied electric field to the electrodes where a change in charge is induced. Taken from [Pas].

4.2.1   The reverse-voltage biased *p-n*-junction

To form a *p-n*-junction the silicon crystal is doped in a way such that a donor and acceptor region adjoin. Thermal diffusions drive the electrons of the *n*-region into the *p*-region where they fill the holes. The result is a positively charged region which restrains the diffusion process more and more until the space charge potential exceeds the available thermal diffusion energy. In the analogous process the diffusion of the holes into the n-region is also limited. The resulting potential between the n- an p-regions is called the "build-in" potential V_b of the detector. The diffusion process leaves a region which is free of mobile charge carries. This neutral region is called depletion region (or space charge region) and can be increased by applying a reversed voltage V_r. The depletion width is given by

$$d = \sqrt{\frac{2\epsilon_0\epsilon_r}{e}\left(\frac{1}{N_A} - \frac{1}{N_D}\right)(V_b - V_r)} \qquad (4.3)$$

where N_D and N_I are the donor and acceptor doping concentrations.

The conductive n- and p-region can be seen as electrodes of a capacitor and the depletion region as its dielectric. The capacitance is then given by

51

$$C = \epsilon_0 \epsilon_r \frac{A}{d} \tag{4.4}$$

where the permittivity of silicon $\varepsilon_r = 11.8$, the detector area A and the depletion width d are then used.

Free mobile charge carriers in the depleted region will be swept by the electric field. In this way the diode acts as an ionization chamber and is the base of the semiconductor detector. Applying a reversed voltage to the diode has two important effects: The volume of the ionization chamber (depleted region) increases and the time for sweeping the charge carriers is shorter which results in a faster detector response.

4.2.2   *p-i-n* diodes

A *p-i-n* diode (compare Fig. 4.4) comprises a third, intrinsic region between the p- and n-region of a common *p-n*-junction diode as described in the last section. The intrinsic region is a layer without or with only low doping and is usually much wider than the p- or n-region. This makes *p-i-n* diodes interesting for detector appliance because the intrinsic layer increases the detection volume and therefore the efficiency for detecting passing by particles. Fortunately *p-i-n* diodes are commonly used e.g. as high voltage rectifiers, radio-frequency switches and photodiodes, such that a wide range of *p-i-n* diodes is available. Here photodiodes are of the most interest because they are already optimized to act as photon detectors. Such photodiodes are used as detector chips for the FBM. Section 4.5 deals with the requirements a suitable diode has to meet.

4.3   Signal processing

4.3.1   Charge sensitive preamplifiers

Charge sensitive preamplifiers (CSPs) are commonly used in radiation detectors to determine the energy of ionizing radiation. Their design offers low noise, good stability, and due to its integrating nature the output is proportional to the total charge flowing from the detector during the pulse event. The fundamental design of all CSPs is illustrated in Fig. 4.5. The pulse, which is in the nanosecond range, needs to be integrated and amplified by the preamplifier. The feedback capacitor C_f stores the charge flowing from the detector (i_d) between the input and output of an operational amplifier (op-amp). The output voltage V_{out} is proportional to the collected charge Q in dependence of the integration time:

$$V_{out}(t) \propto Q(t) = \int^{t} i_d \, \mathrm{d}\tau \tag{4.5}$$

To create one electron-hole pair in silicon an average energy of $\epsilon = 3.8\,\mathrm{eV}$ is needed. The clearly higher absorbed energy E from an X-ray photon or electron (e.g. from nuclear

decay) therefore produces $N = E/\epsilon$ electron-hole pairs. The number of electron-hole pairs is hence proportional to the deposited energy E. The charge flowing to the electrodes is $Q = e * N$ and the conversion factor of the preamplifier C_f^{-1}. Assuming a capacitance of $C_f = 0.5\,\mathrm{pF}$ and a particle energy of $E = 3.8\,\mathrm{keV}$ the output voltage of the preamplifier is given by
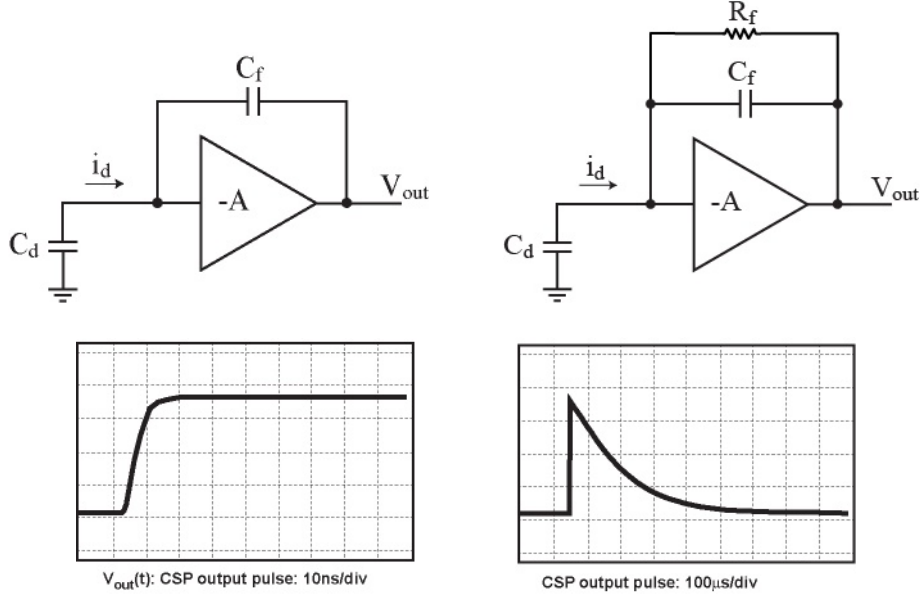
Figure 4.5: The fundamental design of a charge sensitive preamplifier. The charge flowing (I_d) from the detector is stored in a feedback capacitor C_f between the input and output of an operational amplifier. The signal is amplified by the factor of C_f^{-1}. Without applying a feedback resistance R_f (left) the resulting signal is step shaped (lower left panel). The feedback resistor (right) discharges the C_f after each pulse which results in a exponentially falling signal after peaking. Figures taken from Ref. [Inc18].

$$V_{out} = \frac{Q}{C_f} = \frac{\frac{E}{\varepsilon} \cdot e}{C_f} = \frac{\frac{3.8\,\mathrm{keV}}{3.8\,\mathrm{eV}} \cdot 1.6 \cdot 10^{-19}\,\mathrm{C}}{0.5 \cdot 10^{-12}\,\mathrm{F}} = 0.32\,\mathrm{mV}. \tag{4.6}$$

The storage of the δ-like pulses results in a step shaped signal as shown in the lower left panel of Fig. 4.5. It is superimposed with the leakage current of the detector. To prevent the amplifier from saturation the charge needs to be removed from the feedback capacitor C_f. Two standard methods can be used: The "Pulse Reset" method fully discharges the detector in certain time intervals. But the sudden discharge adds noise in the detector and dead time after each reset. The "Static Clear" method removes the charge permanently with a feedback resistor R_f which is in parallel with the feedback capacitor C_f (see Fig. 4.5, upper right panel). In this setup the charge is removed exponentially with time from C_f just after an event occurred. The time dependent decay of the voltage is given by

$$V_{out}(t) = V_0 e^{-t/\tau_d} \tag{4.7}$$
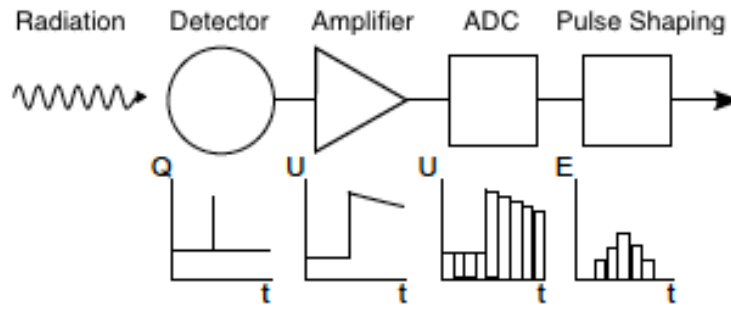
Figure 4.6:   Scheme of signal processing. The δ-like detector pulse is at first amplified followed by digitization and pulse shaping. Taken from Ref. [Bab10a].

where $\tau = R_f \cdot C_f$ is called the feedback time. The amount of discharge per time is proportional to the charge in the capacitor. This leads to an equilibrium between the discharge via R_f and the incoming charge from events and leaking current of the detector and results in a voltage offset.

4.3.2   Data acquisition

The task of the data acquisition (DAQ) is to process the weak, analogue detector signal from the preamplifier output, to trigger events and to extract the pulse height. Figure 4.6 outlines the different stages of the pulse processing. The DAQ includes several shaping and filter procedures (e.g integrating, differentiating and trapezoidal filter) to extract the pulse height fast and precisely. Furthermore the DAQ digitizes the data to enable post analysis with dedicated software.

For the FBM two digital pulse processors[5] (DPP) are used as they are already used for other subsystems in KATRIN. A software module for the DPP is already available in the control and acquisition software ORCA [How04], such that the FBM detector control and data flow can be integrated into KATRIN. In this section, the functionality of DPP's in general and of the DPP's used for the FBM in particular are described based on the documentation of the manufacturer.

DPPs are commonly used in high performance nuclear instrumentation where both low noise and high count rates are required. The basic working principles of DPPs and common analog DAQs are the same. In both cases the preamplifier output is differentiated and integrated which improves the signal-to-noise ratio. In both cases the pulse height is digitized and stored in a histogram. The main difference is that in DPPs the preamplifier signal is digitized directly using a fast ADC. Thus the pulse shaping is digital which enables applying almost ideal digital filters to the input to get the best signal-to-noise ratio at a given count rate. Further advantages of an early digitization is the stability and

---

[5]Manufacturer: Amptek, Inc. - Products: PX5 and DP5
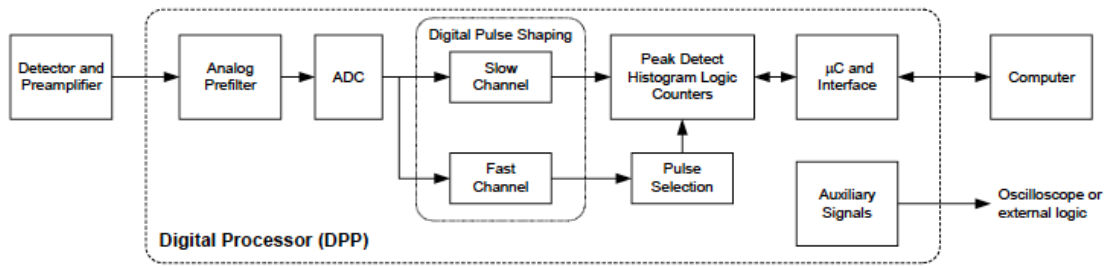
Figure 4.7: Block diagram of the DPP. The output of the charge sensitive preamplifier is the input signal of the DPP. First, the signal is prepared for digitization in an analog prefilter which includes a gain such that the largest pulses are approx. $1\,\text{V}$ (to maximize the effective ADC resolution) and a high pass filter whit a $3.2\,\mu\text{s}$ time constant. Unlike analog DAQs the signal is digitized before pulse shaping in a fast ADC, hence the pulse shape process is digital. There are two independent channels which are optimized for accurate pulse height extractions (slow channel) and a good time resolution of $120\,\text{ns}$ (fast channel). Pulses for which an accurate measurement cannot be made are rejected by the pulse selection logic which includes pile-up rejection, threshold and rise-time discrimination. The histogram logic stores pulses with certain peak height values in their corresponding bins of an ADC and the result is the energy spectrum which is the main outcome of the DPP. The DPPs can be controlled and read out by computers via USB or ethernet connection. It is possible to observe the signal's different stages of the pulse process with an oscilloscope via the DAC output.

reproducibility because in analog systems all parameters are determined by resistors and capacitors and therefore the stability is limited to the stability of these components.

The following outlines the working principle of the DPPs (compare with Fig. 4.7)

Analog Prefilter and ADC: The negative output signal of the CSP is the input signal of the DPP. First it enters the prefilter circuit which prepares the signal for digitization. It includes a high pass filter with a relatively short $3.2\,\mu\text{s}$ time constant, a gain such that the largest pulses are approximately $1\,V$ (to maximize the effective ADC resolution) and a DC offset such that the signal always falls within the range of the ADC. The output of the analog prefilter is digitized by a 12-bit ADC at a 20 or 80 MHz rate. This stream of digitized values is sent into the digital pulse shaper in real time.

Digital Pulse Shaper: The DPP utilizes trapezoidal shaping. A trapezoidal filter provides a very good signal-to-noise ratio and reduces pile-up events at the same time because of its finite nature. Fig. 4.8 shows the typical output shape of the trapezoidal filter as well as the input signal. The rise/fall time (peaking time) and the duration of the flat top can be adjusted over many steps. For comparison a DPP with $2.4\,\mu\text{s}$ peaking time will be roughly equivalent to a semi-Gaussian shaper with $1\,\mu\text{s}$ shaping time. The DPP provides two independent channels. The "slow channel" is optimized to extract the pulse height and therefore provides long shaping times in μs range. The "fast channel" is optimized for isolating pulses which are separated by only $120\,\text{ns}$ in the slow channel. It works with relative short peaking times of $O(100\,\text{ns})$.
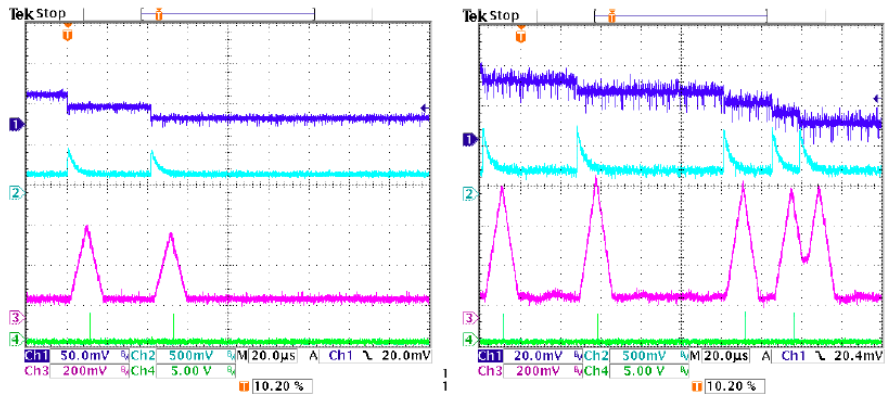
Figure 4.8: Oscilloscope traces illustrating the signal processing. The dark blue trace shows the output of the CSP (in Static Clear Mode). The traces were measured with 60 keV (left) and 5.9 keV (right) X-rays. For the lower energy the signal to noise ratio is clearly degraded. The light blue traces show the output of the analog prefilter, with its 3.2 μs time constant. The magenta trace shows the output of the trapezoidal filter. Its peak height is extracted and binned in the ADC memory. Figure taken from the product manual of the producer.

Pulse Selection: The pulse selection logic rejects pulses for which an accurate measurement cannot be made. It includes the threshold, pile-up rejection and rise-time discrimination.

Histogram Memory: The histogram memory operates as in a traditional MCA. When a pulse with a certain pulse height occurs, a corresponding counter in the memory is incremented. The result is a histogram containing in each bin the number of events with the corresponding peak height value. This is the energy spectrum which is the primary output of the DPP. The unit also includes several other scalers, counting the total number of selected pulses but also counting input pulses, rejected events, etc.

The DPPs provide a BNC input for the signal and auxiliary outputs including a DAC output, such that the signals at different stages of the pulse processing can be tapped and e.g. observed with an oscilloscope (see Fig. 4.8). The devices can be controlled and read out either via USB or ethernet connection. The manufacturer provides a user interface but also a programmers interface which allows customized user interfaces or integrations in other software, as it was done with the ORCA module.

4.4   Quality of a detector

4.4.1   Energy resolution

The energy resolution σ expresses the ability of a detector to accurately determine and resolve the energy deposited in the detector. It is given by

$$\sigma^2 = \sigma_F{}^2 + \sigma_n^2. \tag{4.8}$$

Often the energy resolution is given by the full width at half maximum (FWHM)

$$\sigma_{FWHM} = 2\sqrt{2\ln(2)}\sigma \approx 2.355 \cdot \sigma. \tag{4.9}$$

The first term in Eq. 4.8 σ_F is called Fano noise and arises from statistical fluctuations in the charge collection process. Even when particles deposit the same amount of energy in the detector, there will be fluctuations in the number of electron hole pairs produced. It is given by

$$\sigma_F = \sqrt{\varepsilon F E} \tag{4.10}$$

where F is the Fano factor ($= 0.115$ for silicon), ε the mean energy to create one electron hole pair ($= 3.8\,\text{eV}$ for silicon) and E the deposited energy. For a $10\,\text{keV}$ event $2.355 \cdot \sqrt{\epsilon F E}$ equals approx. $150\,\text{eV}$.

The second term σ_n represents the intrinsic noise of the detector and preamplifier. Statistic fluctuations in all electronic parts and circuits cause variations in voltages and currents which is called (electronic) noise. Sources of these fluctuations are e.g. thermal motions of the electrons, leakage currents, quantum effects or the production and recombination of electron hole pairs. Also external sources can induce noise. In the following section only the most dominant noise sources in a detector-preamplifier-filter-system are considered.

- Parallel noise caused by detector leakage current: Noise sources which produce parallel noise (or current noise) are connected in parallel and act like current sources. The leakage current I_L of the p-i-n diode is such a source. The uncertainty in the signal is not caused by the current itself but by its fluctuations. The current I_L is Poissonian distributed and therefore causes an uncertainty of

$$\sigma_{L,D}^2 \propto I_L \tau \tag{4.11}$$

  Parallel noise can be reduced by decreasing the shaping time of the DAQ.

- Serial noise caused by thermal noise in the JFET: Noise sources which produce serial noise (or voltage noise) are connected in series and act like voltage sources. Such a noise source is located at the gate of the JFET induced by random thermal motions. These varying motions are superimposed with the current. The directly observable results are variations in the signal. That statistical effect decreases if the shaping time increases. The variance ($\sigma_{T,FET}^2$) of the JFET current depends on the input capacity C_D and the shaping time of the DAQ τ.

$$\sigma_{T,FET}^2 \propto e_n \frac{C_D^2}{\tau} \tag{4.12}$$

  where the noise coefficient e_n is device specific and usually given by the manufacturer. Due to its statistical nature serial noise can be reduced by increasing the shaping time of the DAQ.
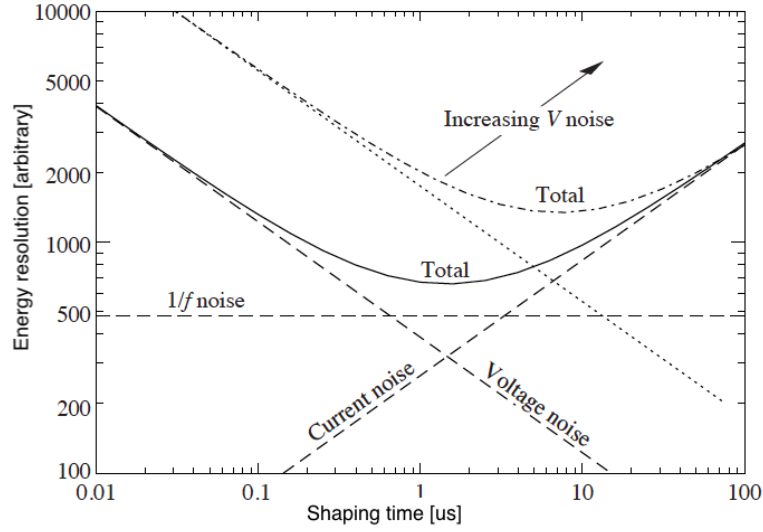
Figure 4.9:   Energy resolution as a function of shaping time. Changing the voltage or current noise contribution shifts the minimum of total noise (solid line). For example increased voltage noise is shown. Taken from [Ber12], changed by the author.

- 1/f noise in the transistor channel: Trapping and detrapping processes in the source drain channel of the JFET introduce additional fluctuations which power spectral density is inversely proportional to the frequency f of the signal. The variance also depends on the input capacity C_D

$$\sigma^2_{f,FET} \propto A_f C_D^2 \tag{4.13}$$

where the noise coefficient A_f is device specific and usually given by the manufacturer. Note: The shaping time does not have any influence to 1/f noise.

The total uncertainty arising from the main noise sources is then given by

$$\sigma^2_n = \sigma^2_{L,D} + \sigma^2_{T,FET} + \sigma^2_{f,FET} \tag{4.14}$$

The two terms in Eq. 4.8 result in a perfect Gaussian peak shape. But additional effects can broaden the peak and cause deviation from the Gaussian shape e.g. pseudo random noise, electromagnetic interference and imperfect charge collection in the detector. Section 4.6.1 deals with the calibration of the detector and includes a line shape analysis as well as the determination of the energy resolution of the detector.

The dependency of Eq. 4.11 and 4.12 on the shaping time leads to optimal shaping time for the best energy resolution (compare Fig. 4.9).

4.4.2   Dead layer

As discussed earlier the dead layer of semiconductor detectors is a region in which charge is, at best, partially collected. For example, electrons with $10\,\mathrm{keV}$ primary energy lose in

a 500 nm-thick dead layer approx. 1.5 keV on average. The lower the primary energy the larger the mean energy loss. As a result the detection thresholds for photons and electrons do not match. Furthermore, a larger mean energy loss is related to a broader distribution which results in a broader peak with the typical pronounced low-energy tail. To keep these effects small the dead layer must be as thin as possible.

The impact of the dead layer onto the detector response needs to be understood and taken into account when predicting or analyzing spectra.

4.4.3 Efficiency

The intrinsic efficiency $\varepsilon_i = N_C/N_D$ of a detector is defined by the ratio of the number of counts N_C in the detector to the number of particles N_D striking its entrance window. For the p-i-n diodes used for the FBM the following effects need to be taken into account:

Reflected particles (ε_r) Due to the interaction of particles with matter the particles can be part-wise reflected from the entrance window. For electrons with energies up to 30 keV a fraction of approx. 22 % is reflected which is derived from numerical simulations (see Sec. 7.3).

Transmitted particles (ε_t) If the interaction probability is too low the particle might not interact with the detector at all. For electrons measured with a semiconductor diode this effect does not occur.

Threshold (ε_{th}) Particles which signal does not exceed the noise threshold remain unregistered.

Dead layer (ε_d) Due to the energy loss in the dead layer a fraction of electrons will not reach the active volume (or their remaining energy will not exceed the noise threshold).

The full intrinsic efficiency is then given by

$$\varepsilon_i = \varepsilon_r \cdot \varepsilon_d \cdot \varepsilon_t \cdot \varepsilon_{th}. \tag{4.15}$$

Interaction cross sections depend on particle type and energy, therefore ε_i depends on these parameters, too.

4.4.4 Pile-up

Pulse pile-up happens when two (or more) pulses arrive closer in time than the shaping time τ_{s} of the DAQ. Two (or more) primary particles will then be detected as one particle with an energy deposit which is larger than the energies of single particles but in maximum the sum of the single energies. Pile-up will therefore adulterate the recorded intensity.

There are two methods how to handle that issue: **1.)** Pile-up rejection is a method where pile-up events are identified by the pulse processor and all pulses involved are rejected. The disadvantage is that there is no guarantee that all or only pile-up events are removed. The involved uncertainties to the count rate and the spectrum are not known and can not be simulated. It is not recommended to use pile-up rejection for the FBM. **2.)** The fraction of pulses involved in pile-up events is given in first order by

$$P_{\text{pu}} = 1 - e^{-(R_{\text{p}} \cdot \tau_{\text{s}})} \tag{4.16}$$

where R_{p} is the number of pulses per second. Keeping the pile-up rate quantity P_{pu} below $10\,\%$ will guarantee that the added uncertainty on small rate changes of $0.1\,\%$ will be kept under $0.01\,\%$ such that in first order pile-up can be neglected for relative flux measurements with small changes but must be taken into account in a more detailed post analysis.

4.5 The FBM detector

4.5.1 *p-i-n* diode detector chip

Due to their wide fields of application, *p-i-n* diodes are available in various specifications and shapes. Photodiodes are of the most interest because they are already optimized to act as photon detectors. In order to find the appropriate *p-i-n* diode for the FBM following requirements need to be taken into account:

Count Rate In the measurement plane of the FBM an electron flux in the order of $O(10^6\,\text{mm}^{-2}\text{s}^{-1})$ is expected. To achieve the required precision of $0.1\,\% = N^{-1/2}$ within $100\,\text{s}$ a minimum count rate of $R = (10^{-6} \cdot 100\,s)^{-1} = 10^4\,\text{cps}$ is needed. On the other side, to keep background effects (e.g. pile-up) as low as possible, the maximum event rate of $O(10^5\,\text{mm}^{-2}\text{s}^{-1})$ should never be exceeded. From basic calculation one gets a rough estimate on the ideal size of the diode which is in the order of $O(10^{-1}\,\text{mm}^2)$. During commissioning tests of KATRIN smaller amounts of tritium are injected such that suitable larger sizes are needed of similar type. An advantage of such small diodes is a low capacitance and low dark current and therefore good energy resolution (compare with Sec. 4.4.1).

Geometry In monitoring position the FBM should not cover any pixel of the FPD and is therefore not allowed to enter the inner flux tube. From the outer flux tube to the inner flux tube is a $7\,\text{mm}$ wide rim. Only within this so-called "outer rim" the FBM is allowed to operate during monitoring. Therefore the casing of the diode must be small i.e. the distance from the diode's center to the most outer edge must be small.

Dead layer The dead layer must be thin enough such that at least half of the beta spectrum can be detected.

Low dark current Lower dark current results in better energy resolution.

Mounting The bare diodes (possibly including a carrier) need to be easily removable from the casing such that they can be mounted onto the board.

Material The p-i-n diodes need to fulfill the material restrictions for UHV and tritium appliance.

Availability For future replacements of the p-i-n diodes a prospect of long term availability is of importance.

Many p-i-n diodes from several manufactures were reviewed and the following two were short-listed:

The p-i-n diode chips AXUVHS11 and AXUVHS5 from the manufacturer "Opto Diodes" have a very thin dead layer of just 10 nm what would enable the FBM to measure very low electron energies. But the diodes are offered in only two different sizes and neither of them are the correct size for nominal tritium operation. Additionally it turned out that it is difficult to remove the bare diode from its casing without damaging it. These diodes are kept as an option in case a lower energy threshold for electrons is desired in future.

The p-i-n diodes 5971, 5972, 5973 series and S9055 series from Hamamatsu come in different sizes which makes the FBM more flexible during commissioning phase when e.g. only fractions of the nominal tritium amount or gaseous Krypton is injected into the source (see Sec. 5.3). Also for the nominal tritium amount a suitable size is available. These commercial "off the shelf" photo diodes come in a TO-18 casing which Hamamatsu offered to be delivered in a customized cap-tapped version where the lid is already removed. It turned out that removing the lid from the off-the-shelf diodes is easy such that the diodes can be purchased from several basic electronic shops at low costs. The bare diodes are mounted on a ceramic carrier which is glued to the TO-18 socket. The carrier can be removed mechanically such that it is ready to be mounted onto the FBM detector board.

Diode type	Sensitive area [mm^2] data sheet	C [pF] (at 10 V)	I_{dark} [pA] (at 10 V)	d_{dead} [nm] data sheet	measured
S9055-01	0.0078	0.5	2		
S9055	0.031	0.8	2		
S5973	0.12	1.6	1.9	<1000	300-500
S5972	0.5	3	10		
S5971	1.1	3	70		
AXUVHS11	0.28	-	-	100	-
AXUVHS5	1	-	-		

Table 4.1: Parameters of the FBM p-i-n diodes. Capacitance C and dark current I_{dark} are taken from the data sheets. The thickness of the dead layer d_{dead} was measured for this thesis (see Sec. 5.2.2).
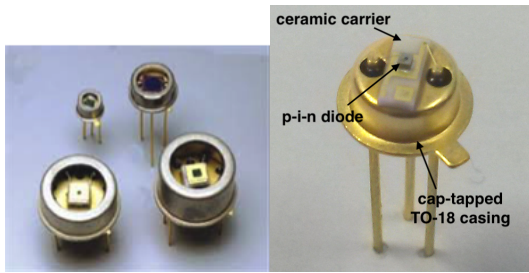
Figure 4.10: Picture of different Hamamatsu p-i-n diodes in TO-18 casings as delivered (left) and the model S9055 with the lid removed (right). The silicon diode itself is mounted on a ceramic carrier which can be taken out of the casing.
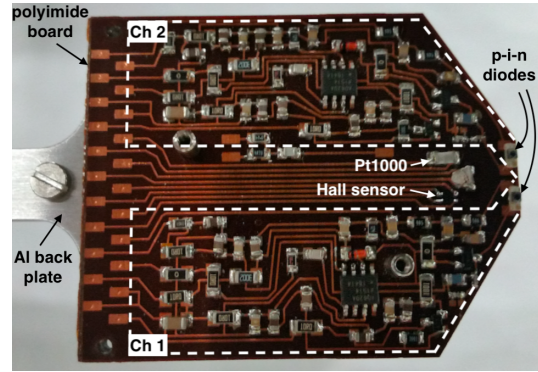
Figure 4.11: The FBM detector board is made of polyimide and equipped with SMD parts. The two p-i-n diodes are glued to the tip of the board and their signals are amplified by two separate transimpedance amplifiers. Close to the p-i-n diodes a Pt1000 temperature sensor and a Hall sensor are located.

4.5.2   Front end electronics

Detector board and back plate

The printed circuit board (PCB) is made of polyimide. Polyimide boards meet the vacuum and material requirements and are less expensive than ceramics which was used for the prototype. At first a 1 mm-thick rigid PCB (Board V1) was tested but it was found that the thermal conductivity of the board was too low to dissipate the heat produced by the electrical components (see Tab. 4.2) The new PCB (Board V2) is a flexible, very thin (0.2 mm) multilayer board which consists of alternating polyimide and copper layers. The PCB is equipped with standard SMD components.

The board is mounted on an 5 mm-thick aluminum back plate. Board V2 is glued to the back plate with a UHV compatible two-component adhesive to ease the mounting of the electrical parts and for a better thermal conductivity. Two distance holder screws additionally fix the board onto the back plate and at the same time serve as mounting points for the stainless steel cover. The cover shields the whole board from the electron flux (and RFI) but features two holes which allow electrons to reach the detectors.

Preamplifiers

The board comprises two detector channels i.e. two preamplifier circuits. Each preamplifier combines two amplification stages where the first is a common-source FET circuit which means that the signal enters the gate of a JFET and exits the drain. The signal can be tapped amplified and with low impedance from the drain and being post processed in the second stage, an operational amplifier (op-amp) integrator. The feedback of the op-amp

consists of a $0.5\,\text{pF}$ capacitor and a resistor of $1\,\text{G}\Omega$. That matches a CSP in static clear mode (see Sec. 4.3) with a feedback time of

$$\tau = C \cdot R = 0.5\,\text{ms}. \tag{4.17}$$

In order to reduce power consumption the JFET current was reduced by replacing the standard $1\,\text{k}\Omega$ drain resistor by $4\,\text{k}\Omega$. This countermeasure decreased the energy resolution but was necessary to reduce the heat production which in turn increases the energy resolution.

The detector chips are glued along with their ceramic carriers between the corresponding electrodes (pads) located at the tip of the board (using two-component adhesive). The cathodes and anodes of the diodes are connected to the corresponding board pads with bonding wires. The bonding is done by the IPE.

The detector board is equipped with additional devices. A Pt1000 temperature gauge measures the board temperature close to the detector chips. It is two wired meaning that the read out resistance has to be corrected for the feeding cables. Additionally a Hall probe is located close to the detectors to measure the magnetic field in the CPS and hence in the detector as well. Both sensors are operated with constant current power supplies (CC supplies) for different reasons. The temperature dependency of Hall sensors are generally lower with CC supplies while the read out of the Pt1000 can be done by reading out the voltage with an ADC. Finally, a LED is attached for alignment measurements. Table 4.2 lists the operation parameters of all components.

Component	Voltage [V]	Current [mA]	Power [mW]
diodes (bias)	+5	-	
op-amps (2x)	±5	4.7	47
JFETs (2x)	+10	1	10
Hall sensor*	≈ ±5	3.45	34.5
Temperature gauge*	≈ +0.4	0.337	0.135
Total power dissipation			148.635

Table 4.2: Operating parameters of preamplifier and sensors. Sensors marked with an Asterix (*) are operated with a constant current power supply. The maximum reverse bias voltage for the diodes given by the manufacturer is $20\,\text{V}$. Since there is no significant performance gain above $5\,V$ it was set to this value. By lowering the currents for Hall sensor and Pt1000 as well as increasing the drain resistor, the power consumption could be reduced by a factor of 2.3 ($340\,\text{mW}$ before). These countermeasure were done to reduce heat production after measuring temperatures above $50\,°\text{C}$ during commissioning.

Electrical feeding

The 22 pads of the board are connected with a special connector which was designed for this work. Common electrical connectors are made of materials which are not UHV compatible due to their strong outgassing behavior. For UHV applications ceramics is commonly used but these are too brittle for small structures. Polyether ether ketone (PEEK) is a

semicrystalline thermoplastic with excellent mechanical and chemical resistance properties and relatively low outgassing values. As illustrated in Fig. A.14 the connector consists of two parts. The bottom part has bores for the contacts matching the footprint of the board pads. As connectors, spring loaded contacts (pogo pins) are used to ensure reliable connections. The cables are soldered to the ends of the pogo pins. The top half of the connector clamps the cables and the contacts for holding them on position. The connector is pressed onto the board by two screws. Because of the pogo pins it is not necessary to tighten the screws too much.

The cable harness is laid from the PEEK connector through the frond end's main cylinder and the 2 m long tube and ends in the back end at two electrical feedthroughs. For the signals two thin (outer diameter =1.45 mm) coaxial cables are used which are fed through a BNC feed through while all other cables for power supply, Hall sensor, Pt1000 and LED are single strand and fed through a D-Sub25 feed through. All vacuum sided cables are polyimide insulated.

Outside vacuum, the BNC signal cables are connected to their corresponding DPPs while the D-Sub25 cable is connected to an interface box which splits the signals from the power lines. A ±15 V power supply and voltage regulators (in the interface box) are used for the preamplifier and bias voltages (compare Tab. 4.2). Hall sensor and Pt1000 are operated with CC supplies and the signal voltages are read out with ADCs.

4.6   Evaluation of the detector (Part 1)

4.6.1   Energy calibration and resolution

In gamma-ray spectroscopy the most commonly used fit function to find a photo-peak is the Gaussian, in best case, with a linear background, which is normally sufficient for high energies. But in semiconductor detectors the photo peak has a more complicated structure, which becomes important for low-energy photons and in small detectors. Figure 4.12 shows the typical shape of the 59.5 keV photon peak in the ^{241}Am spectrum measured with one of the FBM's *p-i-n* diodes. The low-energy tail of the Gaussian leads into a plateau which is essentially flat. Mainly the following two effects cause the distorted peak shape:

Escape Peak Escape peaks are caused by escaping Si K photons after photo-electric K-shell excitations of silicon atoms near to edge regions of the detector. The energy deposited in the detector is reduced by the Si K-photon's energy. The escape peak is $E_s = 1.742$ keV below its parent peak. A peak fit with single gaussian leads to wrong results. The effect is negligible for high energy gamma spectroscopy but becomes important for lower energies. The escape peak can not be seen by eye in Fig. 4.12 because the detector cannot resolve it and its intensity is low. Nevertheless, it broadens and shifts the peak.

Partial Charge Collection In the edge regions of the detector (e.g. doped regions, dead layer) not all the charge created by the incoming radiation is collected due to diffusion or recombination precesses. This results into the flat plateau on the low-energy side of the peak.
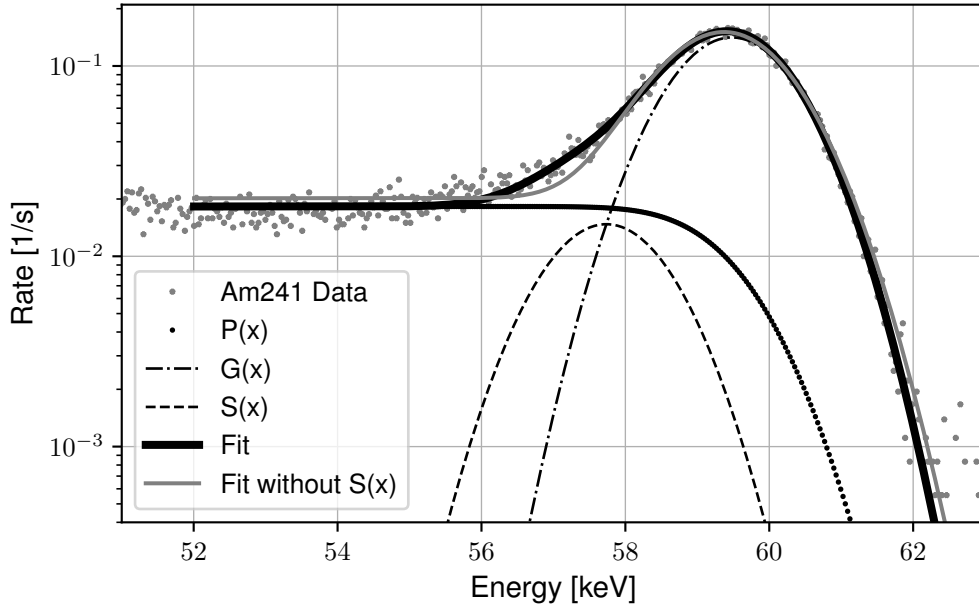
Figure 4.12: Data and fit of the 59.54 keV γ-peak of ^{241}Am measured with the FBM detector. The peak shape differs from the standard Gaussian: Its low energy flank falls into a flat plateau. Furthermore a low intensity escape peak (Si K) is located $E_s = 1.742$ keV below its parent peak. Good fit results (black) can be obtained with a sum of two Gaussians $(G(E), S(E))$ and one error function $(P(E))$. Not considering the escape peak $S(E)$ leads to a slightly worse result (grey).

In Ref. [Cam85] several line shape models are described containing all these features. The following model describes the FBMs detector response sufficiently :

$$R(E) = G(E) + P(E) + S(E) \tag{4.18}$$

where

$$G(E) = \quad A_G \exp[-(E - E_0)^2/(2\sigma^2)] \qquad \text{Full energy peak}$$

$$P(E) = \quad \frac{1}{2}A_P \text{erfc}[(E - E0)/\sqrt{2} * \sigma] \qquad \text{Plateau from partial charge collection}$$

$$S(E) = \quad A_S \exp[-(E - E_0 - E_S)^2/(2\sigma^2)] \quad \text{Escape peak}$$

with the K shell excitation energy $E_s = 1.742$ keV.

In order to evaluate the quality of different line fits, the 59.54 keV peak of ^{241}Am was fitted with three different function and the reduced χ^2_{red} calculated. The fit results are listed in Tab. 4.3. Neglecting the upper effects can lead to a shift of the determined position of up to approx. 0.2 keV (0.1 %) and an overestimation of the FWHM up to approx. 0.4 keV (2 %). Comparing the χ^2_{red} values it therefore appears that the effect of the escape peak is of minor effect which could be neglected in favor to reduce fit parameters in the global ^{241}Am spectrum fit. The full ^{241}Am spectrum includes several characteristic peaks as described and listed in Tab. A.4. Due to the relatively large $\sigma_{\text{FWHM}} \approx 2$ keV (see Sec.
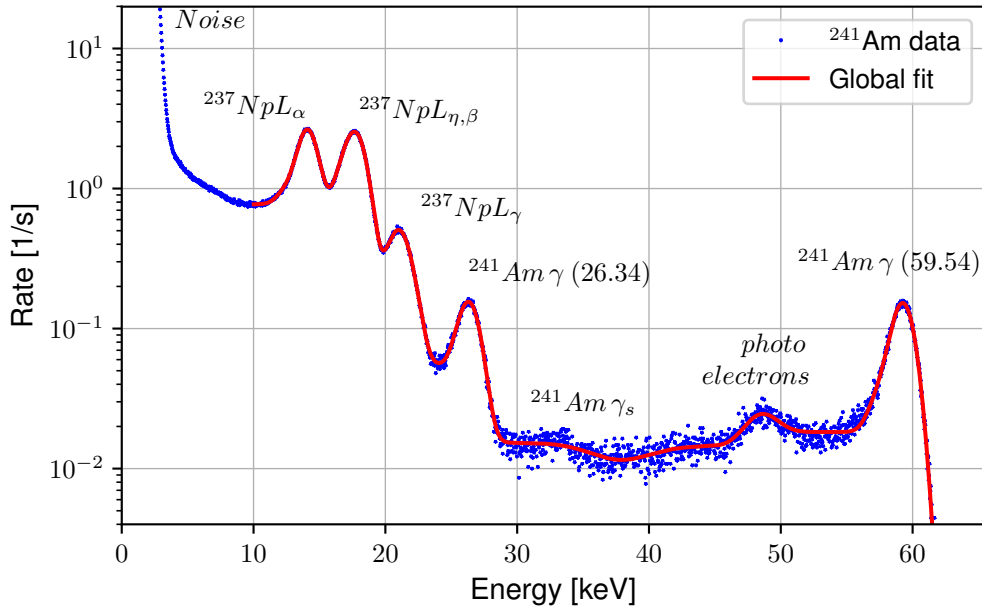
Figure 4.13: Data and fit of the full ^{241}Am spectrum. The spectrum is recorded with the FBM detector (Board 4, Ch.2) with an energy resolution of $\sigma_{FWHM} \approx 2\,\mathrm{keV}$. The positions of all ^{241}Am lines are identified and labeled. The full fit function consists of several peak functions for each visible peak. Each peak function includes a combination of Gaussians and error functions for each (strong) ^{241}Am line in the peak. The global fit comprises 33 free fit parameters. Just the Gaussians parts of the fits of the strongest lines are used for calibration.

4.4.1) of the detector not all lines can be resolved such that several lines are located within one peak.

The ^{241}Am spectrum displayed in Fig. 4.13 is recorded with the FBM detector. The positions of all lines are identified and labeled. There is a trade-off: including all lines into the fit in principle increases precision but also increases the number of fit parameters. Too many fit parameters in a dense region lead to bad fits in which e.g. weak peaks are not found or non existing peaks are found. Therefore, only the strongest lines in the peaks are included as listed in Tab. 4.4[6]. To reduce the number of fit parameters further, the Gaussian and plateau heights (A_G, A_P) of each line are related among lines within one peak with regard to their relative intensities I. Additionally the escape peak $S(E)$ is only considered for the 59.54 keV peak. That way the fit parameter number was reduced from 109 to 33. For the final linear calibration fit only the positions of the strongest lines are used. Exemplary, the calibration fit for the first tritium measuring campaign is shown in Fig. 4.14 and is listed in Tab. 4.3. Figure 4.13 displays the global fit of channel 2.

4.7 Temperature dependance

The amplifiers of particle detectors are in general sensitive to temperature changes because their capacitor and transistor parameters depend on temperature. As a result the

---

[6]A complete table listing all ^{241}Am lines can be found int the appendix

Figure 4.14: Example of typical calibration plot for the FBM (Board 4 (V2), Ch 2).

Fit methods	Centroid [keV]	FWHM [keV]	χ^2_{red}
$G(E)$	59.33(1)	2.38(1)	7
$G(E) + P(E)$	59.456(6)	2.154(14)	4.8
$R(E)$	59.522(6)	2.003(14)	4.9

Table 4.3: Fit results for the 59.54 keV γ-peak of ^{241}Am. Three different fit functions are tested and evaluated by the reduced χ^2_{red}. $G(E)$ is a single Gaussian, $P(E)$ an error function modeling the plateau and $R(E) = G(E) + P(E) + S(E)$ includes the Si K escape peak $S(E)$. Centroid and FWHM are always obtained from $G(E)$.

amplification factor and noise behavior changes resulting in a so-called detector drift which includes a shift of the spectrum and a change in energy resolution. The energy calibration of the FBM can only be done in parking position at atmosphere (vented system) where the detector temperature is around 30 °C.

The temperature of the detector will be different when the detector is inserted in UHV into the cooled down CPS. Upstream at the cold gate valve of the CPS (see Sec. 2.2.2) the temperature of the beam tubes (BTs) increase from 4 K (BT5) to 77 K (BT6). On the downstream side, at the transition from the CPS to the spectrometer section, an increase from 77 K (BT7) to room temperature (SDS) is located. The detector is positioned approximately in the middle of this temperature scenario. While the detector electronics produce heat it exchanges heat with the long detector arm via heat conduction and the CPS via heat radiation. In the following the temperature impacted on the detector response is investigated. The results of thermal simulations, which were performed for this work, can be found in the appendix (see Sec. A.1).

The test setup was cooled down with a refrigerator in a dark and dry environment to -40 °C and warmed up again afterward. During this procedure the detector continuously took spectra from a ^{83}Rb source with 20 s runs. The position of the 12 keV X-ray line is determined for each run. The detector drift in the 12 keV region is $(-1.69 \pm 0.07) \frac{\mathrm{eV}}{\mathrm{°C}}$ as shown by a fit in Fig. 4.15.

Peak	E [keV]	rel. I	Function	cal	FWHM [keV]	
					Ch1	Ch2
γ-peak ^{241}Am (59.54)	59.5412	35.9	$R(E)$	✓	2.01(5)	1.91(4)
γ-peak ^{241}Am (26.34)	26.3448	2.4	$G(E) + P(E)$	✓	1.90(4)	1.82(4)
γ-peak ^{241}Am$_s$	33.1964	0.126	$G(E) + P(E)$		-	-
X-ray peak ^{237}Np L$_{\alpha 1,\alpha 2}$	13.761	1.07	$G(E) + P(E)$		1.70 (1)	1.65(2)
	13.946	9.6	$G(E) + P(E)$	✓		
X-ray peak ^{237}Np L$_{\beta 1,\beta 2}$	17.751	5.7	$G(E) + P(E)$	✓	1.72(4)	1.721(4)
	16.816	2.5	$G(E) + P(E)$	✓		
X-ray peak ^{237}Np L$_{\gamma 1-3,\gamma 6}$	20.784	1.39	$G(E) + P(E)$	✓	1.6(1)	1.8(3)
	21.099	0.65	$G(E) + P(E)$			
	21.342	0.59	$G(E) + P(E)$	✓		
	21.491	0.29				
Photo electrons peak	48-50	-	$G(E)$		-	-

Table 4.4: Overview of the ^{241}Am lines which are included in the global fits and the used fit functions. The centroids of $G(E)$ which are used for the calibration fit are marked (✓).

A drift causes a change in count rate above the set and fixed cut. For example a temperature change of $\pm 5\,°$C causes an energy drift of $\pm 8.45\,$eV which results in a change in rate of $0.16\,\%$ which is already larger then than the required stability of the FBM.
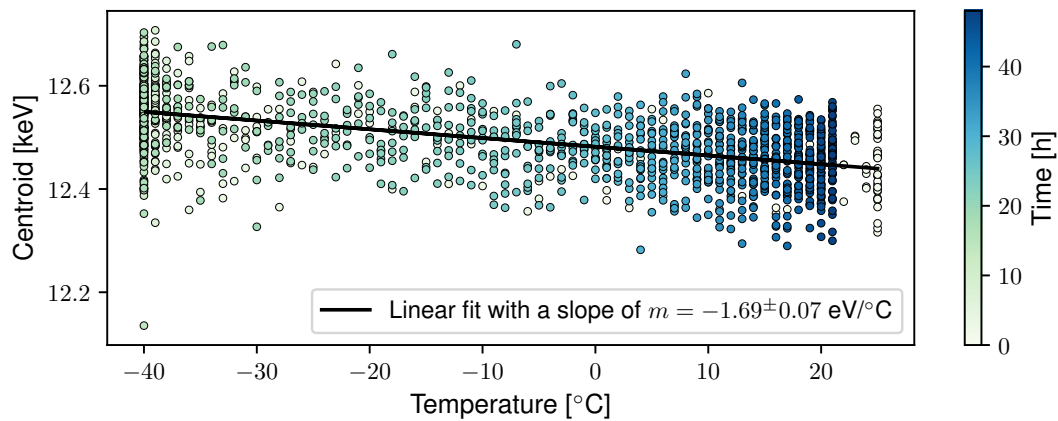
Figure 4.15: Detector drift due to temperature changes. Plotted is the position (centroid) of the $12\,\text{keV}$ X-ray peak of ^{83}Rb for different board temperature. The detector drifts linearly with the temperature by $(-1.69 \pm 0.07)\,\frac{\text{eV}}{^\circ\text{C}}$.

4.8 Stability

As described earlier, the major design goal of the FBM is the ability to measure the relative stability of the electron flux in the CPS with a precision of $0.1\,\%$ within 60 to 90 seconds. The rate is measured by counting events which occur above a certain energy threshold. For non-perfect detectors (noise threshold above zero) which measure a beta spectrum, this threshold must be located within the spectrum (compare with Fig. 4.17). This fact is the main source of systematic errors since the count rate strongly dependents on the stability of the detector response which includes:
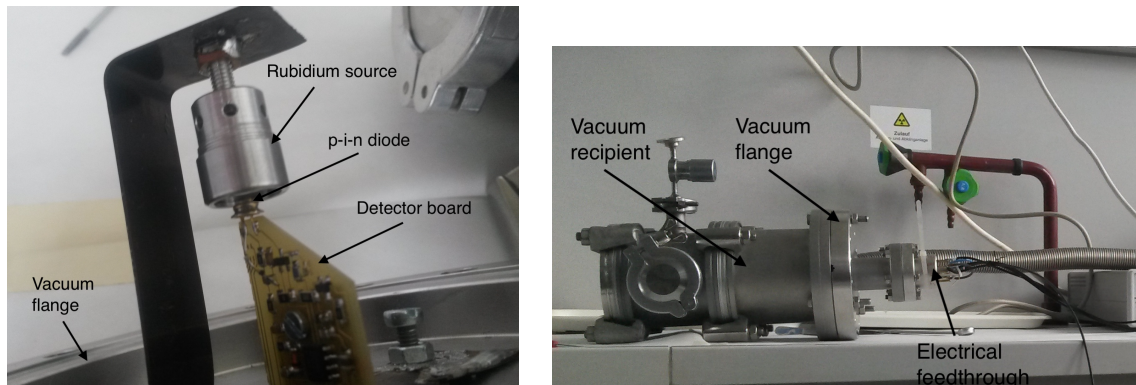
Figure 4.16: The experimental setup for detector tests in Wuppertal. The ^{83}Rb source can be exchanged by ^{241}Am.

Energy resolution: A change of the noise level can change the energy resolution (FWHM) of the detector and thus the widths of the measured peaks. This leads to an exchange of events between the low and high energy sides of the threshold. If the threshold is located at a slope of the spectrum, this exchange is unbalanced.

69

Energy calibration: In case of a detector drift the spectrum is shifted or stretched such that the energy calibration, which was performed beforehand, is no longer valid. Hence the position of the threshold within the spectrum is shifted resulting in a change of count rate.

Noise events: In case of a detector drift or a change in the noise level, noise events can exceed the threshold, which was set beforehand.
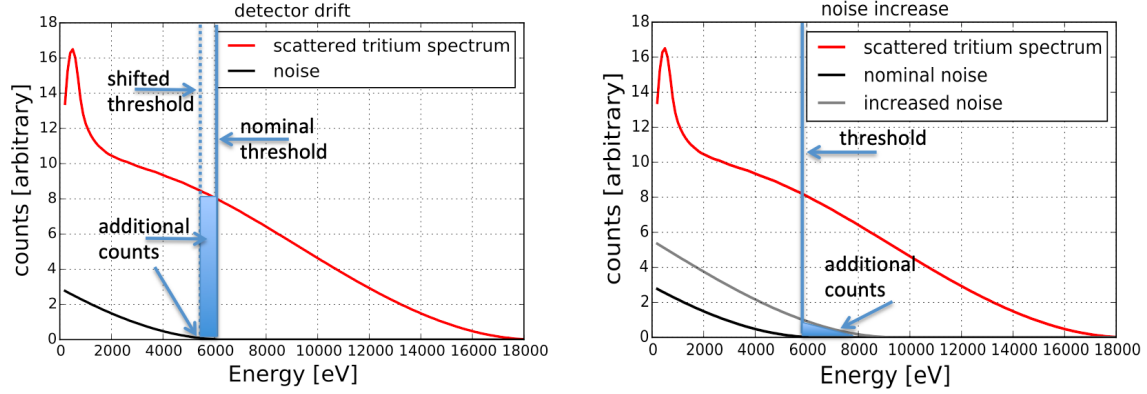
Figure 4.17: In the left plot the noise threshold shifts to lower energies due to a detector drift resulting in a higher count rate. The left plot shows how noise counts exceed the threshold after the noise level increases.

As discussed earlier a detector drift, e.g. due to temperature changes, can be one source of instability. Further sources can include radiation damage and charge up effects in the p-i-n diodes. Therefore for a meaningful conclusion on the detector stability all these components must be included in a test. Furthermore the electron source for the test must be stable at least within 0.1% and emit electrons with similar energies as in the tritium beta spectrum. The isotope ^{83}Rb is such a source (see Sec. 5.1.2).

The half time of ^{83}Rb is relatively short such that approximately 0.1% of the isotope decays every 3 hours. Thus for long term measurements the decay must be considered. Since the lifetime τ of ^{83}Rb is accurately known one can correct for the decay by utilizing the radioactive decay law for the rates $R(t) = R_0 \exp(-\lambda \cdot t)$ where $R(t)$ is the measured rate at time t, R_0 is the rate at time $t = 0\,s$ and λ is the decay constant. To correct for the change, "rate loss" $\Delta R = R_0 - R(t)$ must be added to the measured rate. The corrected rate is then given by

$$R_{corr}(t) = R(t) + R_0 - R(t) = R(t) \cdot \exp(\lambda \cdot t). \qquad (4.19)$$

Due to the Poissonian nature of nuclear decay the error is given by

$$\Delta R_{corr}(t) = \sqrt{N_{corr}(t)}/t_{run} = \sigma \qquad (4.20)$$

where t_{run} is the run time and the frequency with which a rate is measured follows a Gaussian distribution with the standard deviation σ. Once corrected, the data is fitted

with a linear or constant and the reduced chi-squared test applied to test the "goodness" of the fit.

Figure 4.18 illustrates the result of a long term measurement of about 4 days with run lengths of $t_{run} = 300\,s$. The slope of the linear fit is within the error consistent with 0 and the χ^2_{red} value close to one. The frequency distribution is Gaussian and its standard deviation equals the counting statistic error $\Delta R_{corr}(t)$.

This measurement proves that the FBM is able to measure the relative stability of an incoming electron flux with a precision of $0.17\,\%$ within 300 seconds which can be translated into $0.1\,\%$ within 900 seconds. The verifiable precision depends on the measured rate and is therefore limited by the activity of the available source. At the University of Wuppertal the handling of sources of higher activity is forbidden. To allow proving $0.1\,\%$ precision within 60 to 90 seconds a at least $900/90 = 10$ times more active source is needed. Such a source was manufactured and provided (see Sec.5.1.2) for this work and for the use at TLK. By now it was not possible to redo this test and keeps therefore outstanding. The author of this thesis recommends to perform this measurement in the near future.
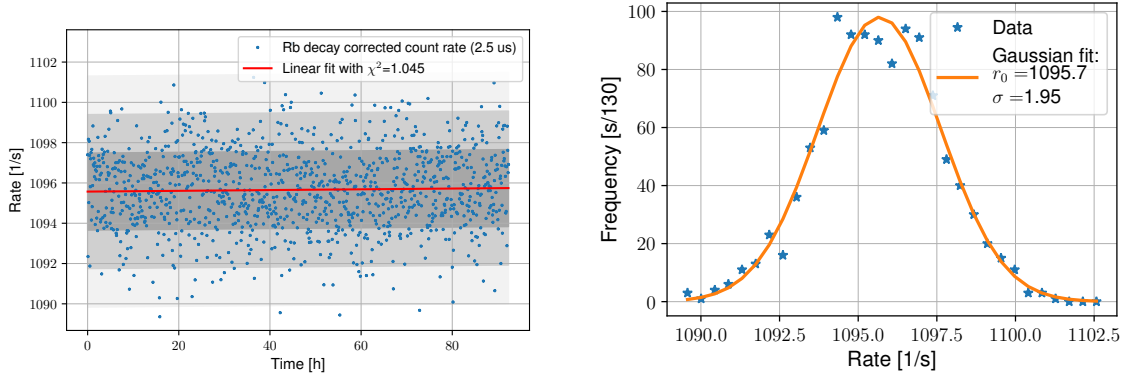
Figure 4.18: Illustration of the stability of the FBM. **Left:** The slope of the linear fit of the rate trend is consistent with zero. **Right:** The frequency distribution of the same measurement follows a Gaussian distribution with the standard deviation σ which equals the counting statistic error.

5 Measurements

This section presents the results of the measurements performed with the FBM during the commissioning phases in Wuppertal and Karlsruhe as well as the first KATRIN measurement campaigns. Some of the data is already analyzed and presented in terms of hardware alignment and detector evaluation in chapter 3 and 3, respectively.

In the first section the properties of the gamma and electron sources, which are used for the measurements, are described. Measurements during the commissioning phases, which basically serve as an evaluation of the detector, are presented in Sec. 5.2. The first results from the gaseous ^{83m}Kr and the first tritium measurements campaigns are given in Sec. 5.3 and 5.4, respectively. The first measurements with the rear section electron gun (RS e-gun) are analyzed in Sec. 5.5. The sections 5.7 and 5.8 comprise two subsequent measurements and analyses, e.g. a shape comparison between magnetic and electron flux.

In some cases the data is compared to the results of numerical simulations of the detector response which are not further explained at this point but described in detail in chapter 7.

5.1 Radiation sources

5.1.1 X-ray sources

X-ray sources allow an energy calibration which is independent of dead layer effects. It is also used to determine detector characteristics such as the energy resolution.

In Americium sources, ^{241}Am nuclei decay with a half time of 432.2 years only via α-decay into the daughter nuclei ^{237}Np which remain with 99.65 % probability in excited states. These nuclear states and also the excited electron shell of ^{237}Np decay over several cascades by emitting discrete γ-ray and X-ray lines, respectively. The most intense lines up to 60 keV are listed in the appendix (see Tab. A.4). Figure 4.13 shows a ^{241}Am spectrum measured with the FBM.

The ^{241}Am source which is used in Wuppertal has an activity of about 350 kBq, while the one at KIT has an activity of 18.5 MBq. However, the used p-i-n diodes have relatively small entrance windows and are very thin. The first property limits the number of photons reaching the detector while the latter reduces the efficiency for photons strongly. In addition the minimum distance between source and p-i-n diode at KIT is limited by the detector's cover. The count rates are therefore in the 100 cps regime for the largest diodes and 10 cps for the small diodes such that especially for the small diodes long calibration measurement times are needed.

5.1.2 Electron sources

Electron sources are used to investigate the dead layer effects and hence the detector response to mono-energetic electrons. The dead layer thickness can be determined and the sources are used to examine the stability of the detector.

Rubidium 83 (^{83}Rb)

Nuclei of the isotope ^{83}Rb decay with a half time of 86.2 days only via electron capture into excited ^{83}Kr* which emits both gamma-rays as well as conversions and Auger electrons to reach its stable ground state. In Tab. A.5 the energies and relative intensities of the emitted electrons and gamma particles from 5 to 32 keV are listed and Fig. 5.2 shows ^{83}Rb spectra recorded with the FBM.

Three custom ^{83}Rb sources were produced with our collaborators. The sources were produced by implanting ^{83}Rb ions into a metal target at the Bonn University[7] mass separator using ^{83}Rb produced at the NPI Rež[8] cyclotron.

Source (i) and (ii): Two sources were produced for the use in the Wuppertal laboratory. The ^{83}Rb is implanted into 100 μm-thick polycrystalline aluminum foils with 4 keV implantation energy and a maximum activity of 1 MBq, which is the maximum allowance under the permission on radiation protection for the University of Wuppertal. The sources are delivered as bare metal sheets and put in a casing in Wuppertal. Figure 4.16 shows such a source and how it is positioned in front of the test detector setup.

Source (iii): This source will be used in the tritium laboratory at KIT. The ^{83}Rb with a maximum activity of 15 MBq is implanted into a polycrystalline aluminum block. For the use in KATRIN much stricter regulations to the casing of the source need to be complied in order to guarantee radiation safety and prevent contamination. The two-piece casing (Fig. 5.1, left) is easy and quick to assemble and the cover flap can be opened easily with a long tool. The source holder in Fig. 5.1 (right) allows the positioning of the source within the FBMs six-way-cross such that the detectors movement mechanism can be used to align the source with the desired *p-i-n* diode.

Electron guns

Unlike natural isotopes, an electron gun (e-gun) can provide mono-energetic electron beams with a freely selectable energy within a certain range.

Wuppertal field emission e-gun   As part of this work an e-gun has been developed fitting the requirements for the purpose of detection of low energy electrons with *p-i-n* diodes. The e-gun produces electrons via the field emission effect and accelerates them to any desired energy between 4 and 20 keV with a flux in the 10^4 cps regime. It's main purpose is the study of the detector response, e.g. the characterization of dead-layer losses. For detector stability tests the e-gun is insufficiently stable. Chapter 6 describes the development of the e-gun.

---

[7]Helmholtz - Institut für Strahlen- und Kernphysik, Bonn
[8]Nuclear Physics Institute of the Czech Academy of Sciences, Rež
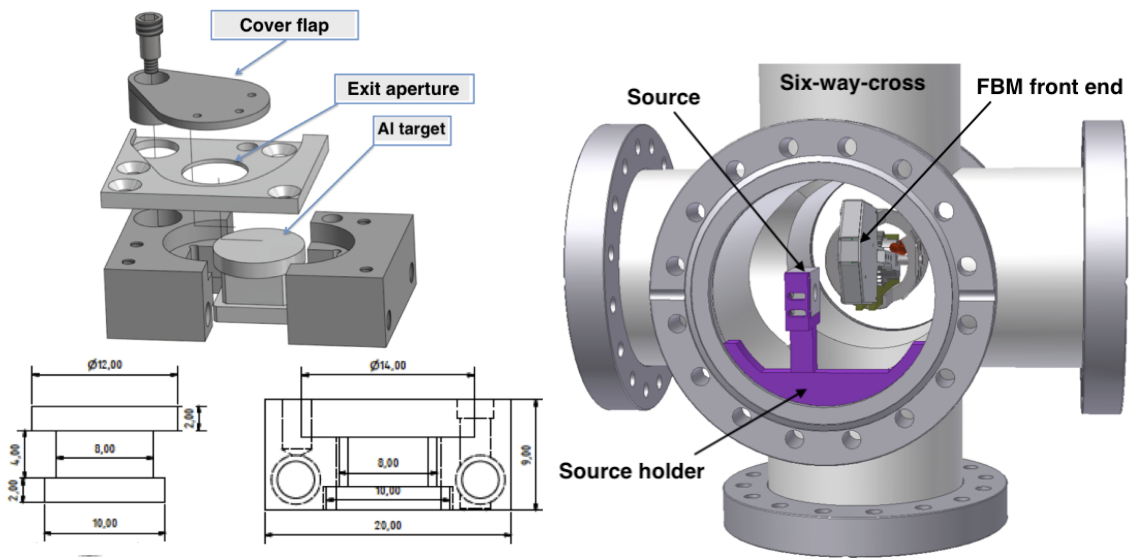
Figure 5.1:   Rubidium source (iii) (left) and source holder (right) for the use in the FBM setup at KIT.

Rear section e-gun   The RS e-gun is introduced already in Sec. 2.3.3. In addition to the characteristics of the Wuppertal e-gun it allows angle selection, better stability and precise positioning. It can be used for studying the energy-dependent detector response, in-situ detector drift tests, alignment and stability tests.

5.2   Evaluation of the detector (Part 2)

In section 4.6 the detector is evaluated with regard to its energy resolution, temperature dependence and stability. In this section the influence of hight rates and the determination of the dead layer thickness are addressed.

5.2.1   Influence of high rates (pile-up)

With the ^{83}Rb sources several spectra are obtained at different rates as they are shown in Fig. 5.2. Because of the high intensity of the Bonn ^{83}Rb source, it is possible to achieve high count rates. The maximum registered rate was 50 kcps. Although these measurements were taken with the pile-up rejection (PUR) enabled, a huge pile-up background can clearly be seen in region C and B (green), which also features a pile-up peak at about 60 keV. In region A the relative intensities among the peaks change if the rate changes.

This example shows that the PUR of the DAQ does not work sufficiently. The PUR can only reject events which occur within the peaking time of the fast channel which is maximum 400 ns resulting for example in approximately 2 % not rejected pile-up events at a rate of 50 kcps (Eq. 4.16). Due to its short peaking times the fast channel is noisier compared to the slow channel and hence has a higher noise threshold. Events not exceeding the slow channel but the fast channel threshold, are not rejected. Additionally it can be

observed that a change of the noise level in the fast channel, such that noise events exceed the formerly set noise threshold, has the following effect: electron events, which pile-up with these "new" noise events, are additionally rejected which leads to a dropping count rate.

Therefore the author of this thesis recommends not using the pile-up rejector of the DAQ since it adds more unknown systematics than it removes. A better approach is choosing the right electron intensity to diode size combination to keep the uncertainties, which are caused by pile-up effects, below 0.1 % (compare with Sec. 4.4.4) and if necessary correct for it afterwards with adequate tools, either analytically (e.g with Eq. 4.16) or with dedicate numerical simulations (e.g DRIPS software).
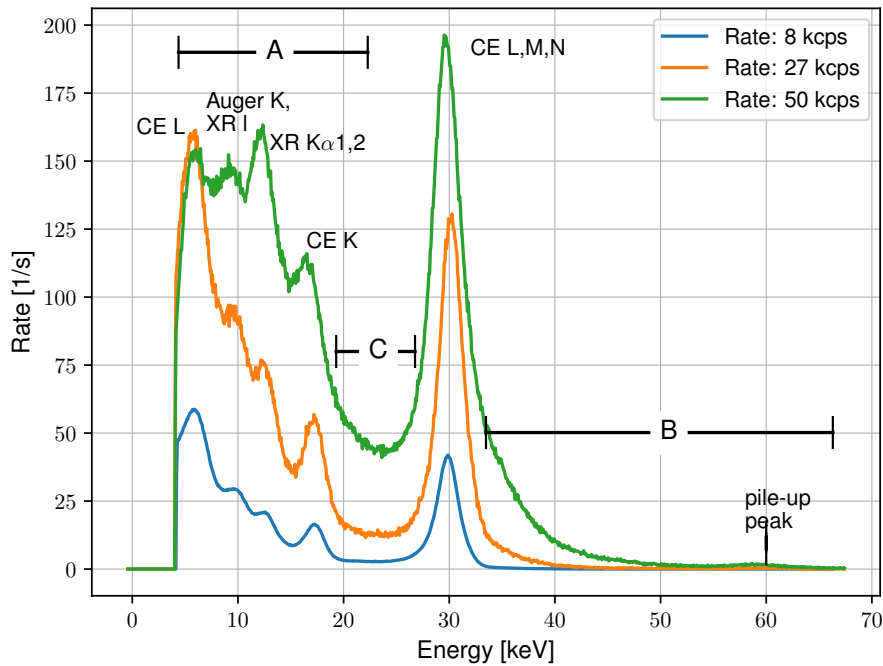
Figure 5.2: ^{83}Rb spectra with low, medium and high event rate measured with enabled pile-up rejection. The positions of the strongest conversion electron, auger electron and X-ray lines are identified and labeled. In region B and C pile-up effects can still clearly be seen for the 27 and 50 kcps spectra. In region A the relations between the intensities of the peaks changes if the rate changes.

5.2.2   Dead layer

Each electron passing the dead layer loses a certain amount of energy before it reaches the detection volume. The mean energy loss of the electrons results in a shift of the observed peak in the spectrum to lower energies. The mean energy loss depends on the dead layer thickness and the electron's initial energy. Electron spectra were taken with the *p-i-n* diode model S5972 at different acceleration voltages with the Wuppertal e-gun. The peak positions are plotted in Fig. 5.3 as a function of initial electron energy. In a detector without a dead layer all data points would lay within the identity function. But the used
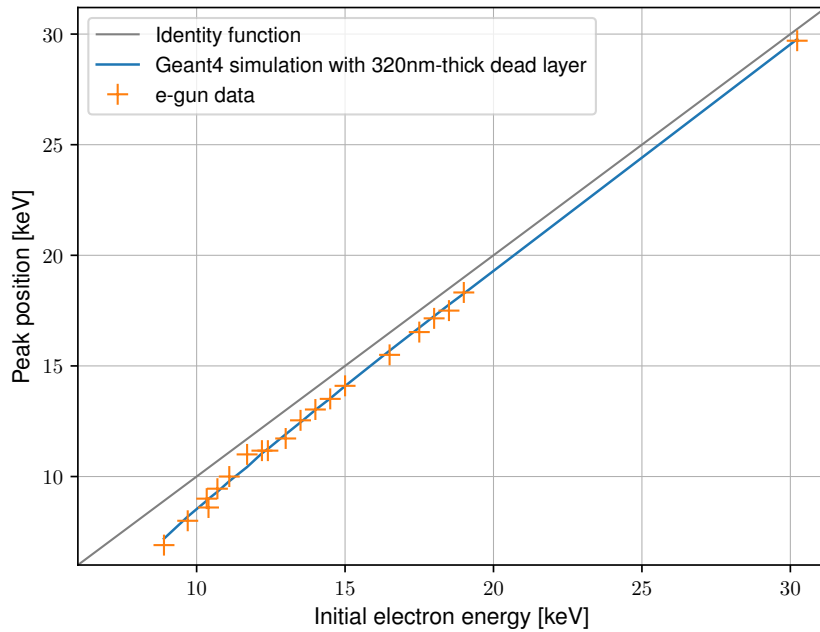
Figure 5.3: Dead layer measurement of the S5972 *p-i-n* diode with the Wuppertal e-gun. The measured peak positions as a function of the initial electron energy are shown. For an ideal detector (no dead layer) and data acquisition all measurements must be within the identity function but due to the energy loss the measured peaks are shifted towards lower energies. The best simulation results were achieved using a 320 nm-thick dead layer.

p-i-n diode features a dead layer such that the mean energy loss (distance between identity function and data points) is none-zero and increases towards lower initial energies.

This measurement has also been simulated for several dead layer thicknesses (see Ch. 7 for details) and the best-fitting simulation is chosen according to the χ^2 value. The best fits are obtained with a 320 nm-thick dead layer. The data is shown in Fig. 5.3 together with the simulation result.

5.3   Gaseous ^{83m}Kr campaign

Gaseous ^{83}Kr was for the first time induced into the WGTS without any additional carrier gas. The purpose of this campaign was to test the KATRIN setup in terms of high-voltage operation and temperature-dependent source properties. The excited gaseous Krypton 83 (^{83m}Kr) was injected into the WGTS with the so-called "Krypton Generator". The conversion electrons from ^{83m}Kr decays were detected with the FBM, the FPD and indirectly with the BIXS detector. The FBM's noise level was relatively high during this campaign such that the lower energy threshold had to be set to 14 keV. Therefore only the 18 and 30 keV peak can be identified in the observed spectrum in Fig. 5.4.
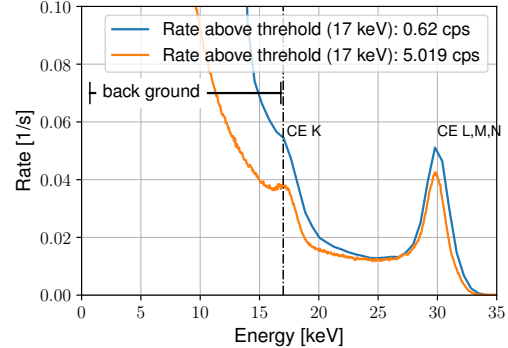
Figure 5.4:   Krypton spectrum recorded during the gaseous ^{83m}Kr campaign.

Nevertheless, constant monitoring of the ^{83}Kr* was performed. The normalized relative count rates are compared with the FPD and the BIXS system which is shown in Fig. 5.5. The vertical lines indicate hardware changes in the KATRIN setup. All three detector systems observe an increase in count rate by a factor of about 5 when the intensity of the krypton source was increased (green line). When the magnetic field of the WGTS was lowered (grey lines) the FBM and FPD measured a decrease in the count rate by 50 % and 20 %, respectively. The reason for the lower count rate is a combination of two effects: first, the acceptance angle for electrons from the source is lower and second, the flux tube is smaller and more focused. The latter effect strongly decreases the flux at the FBM's monitoring position which is at the rim of the flux tube. The BIXS system is not sensitive to the magnetic field setting.

5.4   Tritium measurement phase

In preparation for the nominal tritium operation, for the first time tritium was injected into the WGTS on 19th of May 2018 with a gas mixture of 0.5 % tritium in deuterium. This was a crucial milestone of the KATRIN experiment. The campaign allows the characterization of the hardware, systematic effects and the overall stability of the systems including the FBM. A disadvantage of this step is that from now on it is more complicated, time consuming and at some point impossible to maintain the systems due to tritium contamination. In contrast to the DPS and the WGTS the procedures are a bit easier for the FBM since the system is classified as tritium free from the V1 downstream. Still, for maintenance purposes, e.g. a front-end change, the fume hud and the system have to be opened which needs contamination measurements and supervision by the radiation office. In addition, only qualified persons can do the work.

During this very first tritium measurement the FBM manipulator was equipped with the faraday cup to perform ion and electron measurements. The interested reader is referred
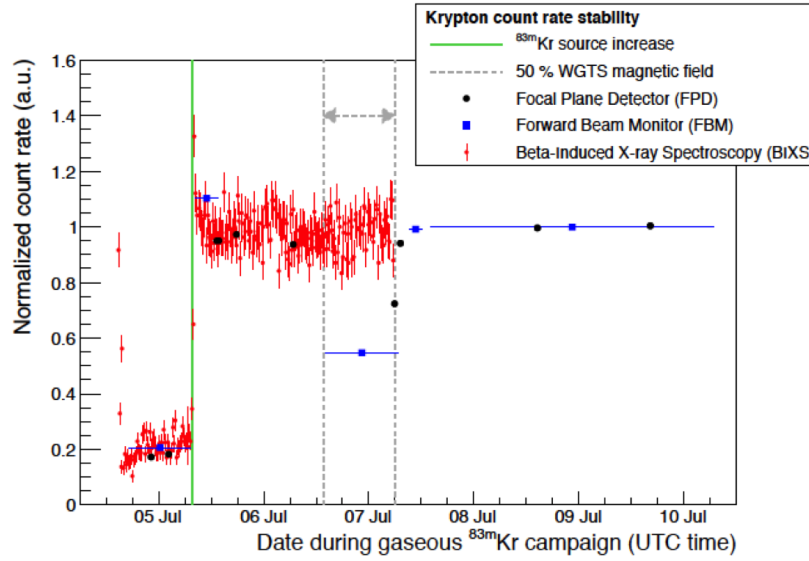
Figure 5.5: Normalized relative count rates observed by the FBM (blue squares), the FPD (black circles) and the BIXS detector (red dots) during the gaseous ^{83m}Kr campaign. The vertical lines indicate hardware changes. The count rate increased by a factor of 5 in all three detectors when the ^{83m}Kr source intensity was increased (green line). When the magnetic field in the WGTS was lowered (gray lines), the FBM and FPD measured a decrease in count rate by approximately 50 % and 20 %, respectively while BIXS is insensitive to the WGTS magnetic field. Taken from [Are18].

to [Kle18]. The FBM detector measurements started two weeks later on 7th of June during the so-called "first tritium measurement campaign" which took place from the 5th to the 20th of May 2018. A list of the monitoring runs, which are analyzed for this work, can be found in table 5.2. In the following sections the results of this very first data-taking period with tritium are presented.

5.4.1   Configuration and acceptance test

With 0.5 % tritium purity an electron flux of only about $5000\,\mathrm{s}^{-1}\mathrm{mm}^{-2}$ is expected. Therefore the largest p-i-n diodes are chosen ($1.1\,\mathrm{mm}^2$, Board no. 5) to optimize counting statistics. The peaking time of the DAQ for booth channels was $6.4\,\mu$s resulting in a pile-up rate of about 3 % which can be neglected for stability analyses (see Sec. 4.4.4).

Acceptance tests were performed prior to the campaign to extract the backgrounds, calibrations, energy resolutions and noise thresholds of the detectors. These measurements were taken with the Karlsruhe ^{241}Am source in the vented system with the FBM in parking position. The source is put directly in front and between the two diodes. The desired diode can then be chosen by using the standard movement mechanics (manually) and be adjusted to find the maximum count rate. Section 4.6.1 describes the analysis method and Fig. 4.13 shows one of the ^{241}Am spectra extracted from these measurements. The obtained calibration parameters are listed in Tab. 5.1.

78

Channel	τ_{pt} [μs]	slope m [eV/channel]	offset b [eV]
1	6.4	31.859 ± 0.031	-497.230 ± 0.016
2	6.4	32.006 ± 0.045	-516.935 ± 0.023

Table 5.1: Calibration parameters for the first tritium campaign.

5.4.2 Cool down

For the first time it was possible to test the thermal properties of the new detector board type V2, which was designed to reduce the board temperature, directly within the CPS. The cool down time determines how long it takes before the FBM detector is operational for stability measurements. The final temperature needs to be below room temperature and above the operation parameters of the electrical components.

The detector is inserted into the CPS from room temper-
ature environment. The powered detector board (ther-
mally optimized board type 2) has an initial temperature
of 38 °C and reaches the equilibrium of -15 °C after about
25 hours which is shown in Fig. 5.6. The vertical line
indicates when the detector reaches the temperature at
which the expected change in rate due to a temperature
related detector drift is less than 0.1 % (compare with
Sec.4.7) which is after 11 hours.
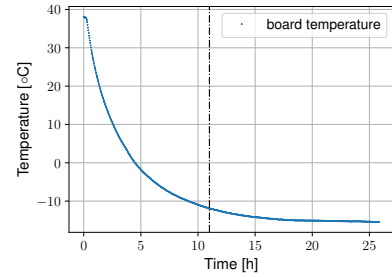
Figure 5.6: Cool down of the de-
tector.

5.4.3 Tritium spectrum

The noise corrected spectrum shown in Fig. 5.7 is the first tritium spectrum recorded with the FBM. Between 8 and 20 keV the spectrum agrees with the expectation, but below 8 keV the steepness of the slope was unexpected since it further decreases. This is probably due to background counts from noise and edge effects from the diode (see Sec. 5.5.1 and 7.2). This may also explain why the spectra of the two channels do not match for lower energies. But the most likely source for this mismatch, which is also the reasons for a about 2 % lower rate in channel 1 than in channel 2 during the whole campaign, is the uncertainty in the energy calibrations.

5.4.4 Flux tube scans

Several scans of the flux tube's cross section were performed recording the tritium count rate, the magnetic field, and the temperature. As an example, Fig. 5.22 illustrates all measured quantities, including the detector positions, during such a scan. During a scan, the temperature usually drops by about 1 °C, which happens when the detector is moved

79
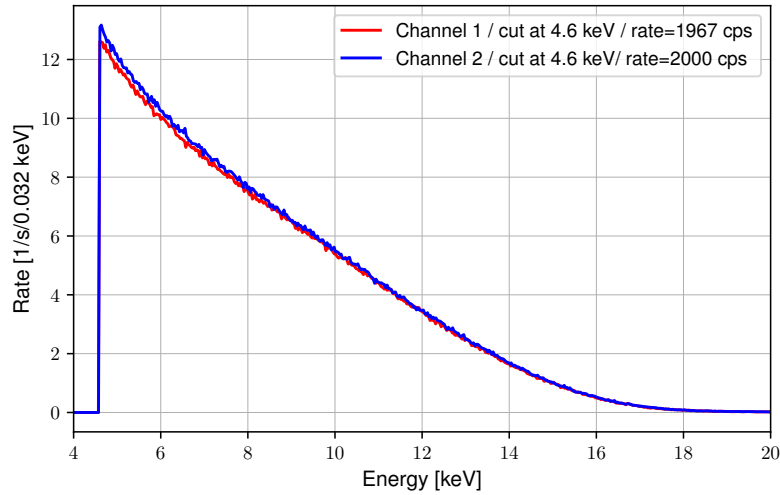
Figure 5.7: Tritium spectrum measured with both channels of he FBM detector during the first tritium campaign. The rate of channel 1 was approximately 2 % lower compared to channel 2 during the whole campaign. This is probably because of uncertainties in the calibrations which cause the deviations among the channels for lower energies.

further into the cold CPS where the detector directly faces the 4 K cold beam tube of the CPS in which the argon frost layer is prepared.

Since the motors induce noise only sub-runs are analyzed in which the motors are switched off. Figures 5.8 and 5.21 show for both detector channels the results of one cross scans (RUN164) for the tritium rate. The tritium flux shows the expected Gaussian shape where the rate drops from the center to the outer rim by approximately 10 % as predicted by simulations [Hau19]. It can be seen that the event rate for identical positions changes during the scans which affects the extracted mean of the fits. Nevertheless, the means are comparable to the results of the alignment measurements (see Sec. 3.4). The magnetic field data of the same scan (see Fig. 5.9) has smaller uncertainties and the Gaussian fits better to the data.

In Fig. 5.9 the result of the magnetic field data during the same scan is shown. Due to the fact that the magnetic field can be considered as constant the analysis includes no unknown systematic error. The scans fit to a high degree and confirm the result of the magnetic field scans performed in July 2017. Only the y_0^e encoder value changed which corresponds to a movement of the lever of approximately $0.5\,°$. This small movement can be explained by the mechanical temperature drift.
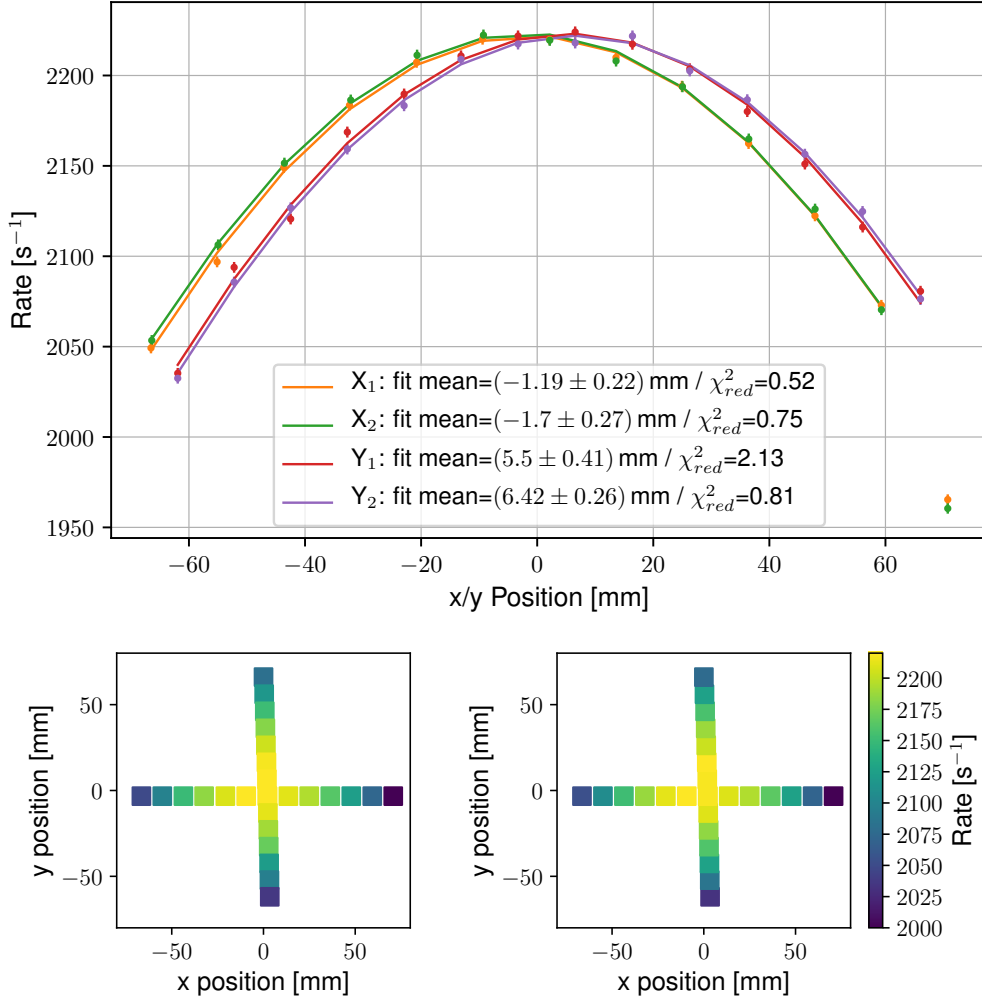
Figure 5.8: Radial dependence of the count rate derived from a cross scan during the first tritium campaign (channel 1). **Top:** 1D Gaussians are fitted to the data for each horizontal ($X_{1,2}$) and vertical ($Y_{1,2}$) scan. The Gaussian means are comparable with the results from magnetic field measurements. One can clearly see that for same positions different rates are measured e.g. the rate increased during the x- scans such that the mean of the X_2 fit is lower than for X_1. The Gaussian standard deviations are approximately $\sigma = 165$ mm. **Bottom:** Scattered 2D-plot of the same data. The scans for y are not perfectly on a vertical line due to the chosen scan pattern which explains the larger uncertainties in the fits.
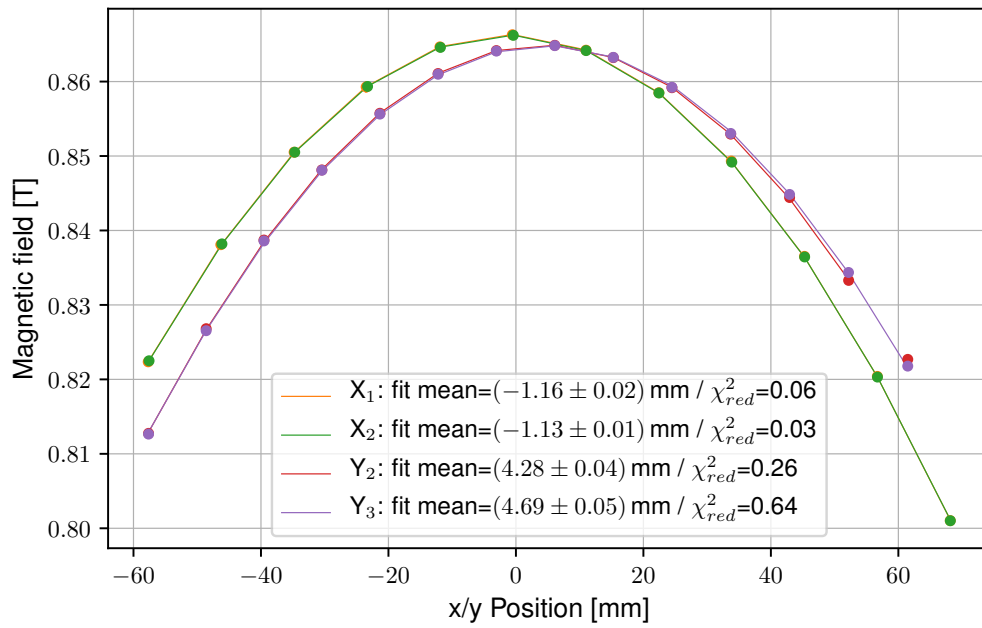
Figure 5.9: Radial dependency of the magnetic field within the CPS derived from a double cross scan during the first tritium campaign. 1D Gaussians are fitted to the data for each horizontal (x) and vertical (y) scan. The Gaussian means are comparable with the results from other magnetic field measurements. The error bars are smaller than the graph symbol size.

5.4.5 Rate stability

In section 4.8 it was shown that the FBM is able to monitor an electron flux with $0.17\,\%$ precision within 300 seconds which can be translated into $0.1\,\%$ within 900 seconds. However, these values were obtained in the Wuppertal laboratory. During the installation of the FBM at KIT the electrical feeding of the detector underwent several changes and a second stage preamplifier was added between detector board and DAQ. To keep the noise as low as possible the new amplifier is positioned right after the signal is fed through from vacuum to the ambient-air.

During the two weeks of campaign the FBM was mainly monitoring the flux in the CPS at position $x_{\mathrm{FBM}} = 65\,\mathrm{mm}$ ($x_{\mathrm{e}} = 420263558$). The whole monitoring time is separated into 6 time intervals (regions) as listed in table 5.2. Time by time background measurements were taken slightly out of the beam at $x_{\mathrm{FBM}} = 80\,mm$ ($x_{\mathrm{e}} = 421833798$). The full rate trend graphs are shown in Fig. 5.10 for both diodes including selected linear fits to the data. There is a long term drift of approximately $0.2\,\%/h$ which spreads over the regions while for single regions the drift is generally smaller, especially for the longer regions 2, 3, 5 and 6, hence the reason for the long term drift must mainly originate from events which happened between the regions.
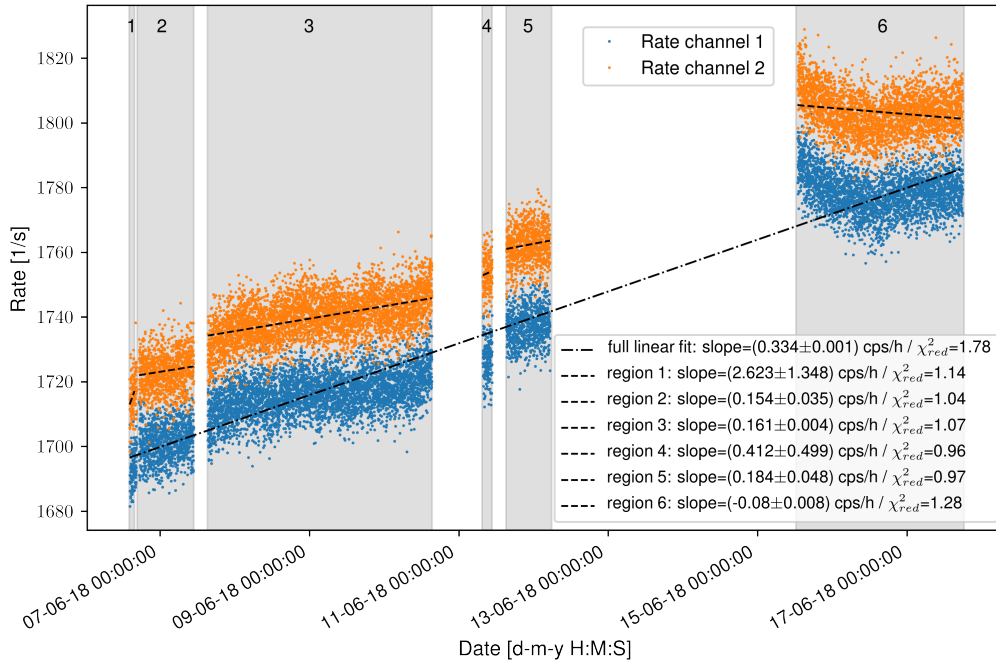
Figure 5.10: Rate trend summary of the whole tritium campaign. Plotted is the full available data from the stability measurements at monitoring position for both channels. The count rates for channel 1 are approximately 0.7 % smaller compared to channel 2 using the same energy threshold (here 5.3 keV). Apart from that, the channels follow same trend. The full linear fit reveals a mean relative change of about 0.2 % per hour while for the single regions this value is smaller than 0.1% per hour.

To investigate the reasons for the instabilities, the tritium spectra taken at different times are compared. In Fig. 5.11 the integrated spectra of the first and the last hour of the

72 hours time interval (region 3) are plotted with the residuals. It is visible that the shape of the spectrum changed. This observation is representative for both channels and all regions and the change in the shape happens continuously over the whole data-taking period. Therefore the rate change cannot be explained by a simple change in the intensity of the flux as it would be the case if the tritium purity changes. Also a simple change in the detector's gain can be ruled out since it is not possible to match the shapes with a linear recalibration. Note that it is still possible to have a combination of two or more effects such that the former mentioned effects cannot be completely ruled out.
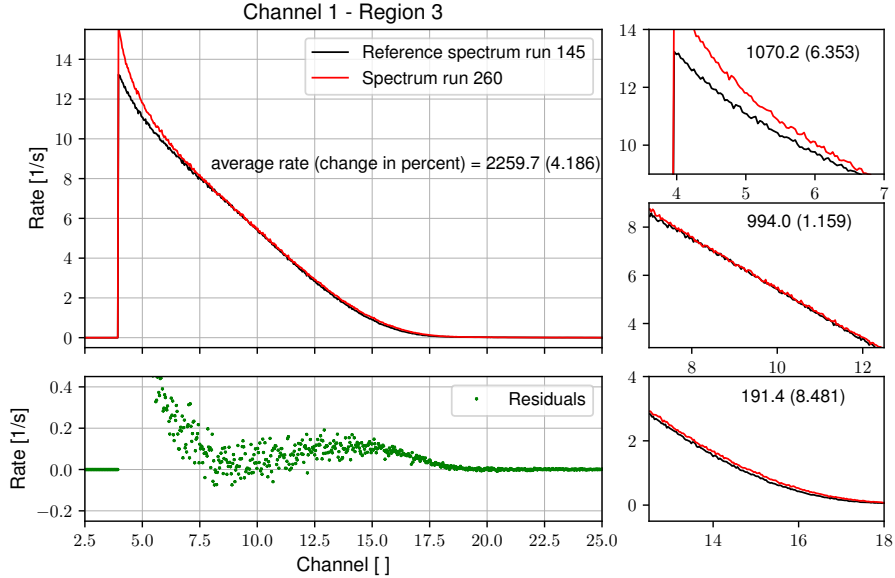
Figure 5.11:   Change of the measured shape of the tritium spectrum during the first tritium campaign. As an example the first and the last run of region 3 are compared revealing a change of the tritium spectrum measured with the FBM. This change develops continuously over time causing the continuously increasing rates during the whole campaign. In this region the rate changes by 4.2 % within 72 hours. Different to the nominal threshold here a lower threshold of 4 keV is chosen to illustrated how the effect increases with lower energies.

FBM Runs	Run length	Duration	Region
145-146		$2.2\,h$	1
150-167		$17.5\,h$	2
169-240	$1\,h$	$72\,h$	3
248-250		$3\,h$	4
253-266		$13\,h$	5
348-400		$53\,h$	6

Table 5.2:   Monitoring run list for the first tritium data-taking. The monitoring position for all runs is $x_{\mathrm{FBM}} = 65\,\mathrm{mm}$. Approximately 159 hours $\approx$ 6.6 days of monitoring data is available. The regions correspond to the shaded regions in Fig. 5.10.

In order to find the source of the instabilities the count rates are compared to all quantities with possible correlations by calculating the Pearson correlation coefficients. This is done
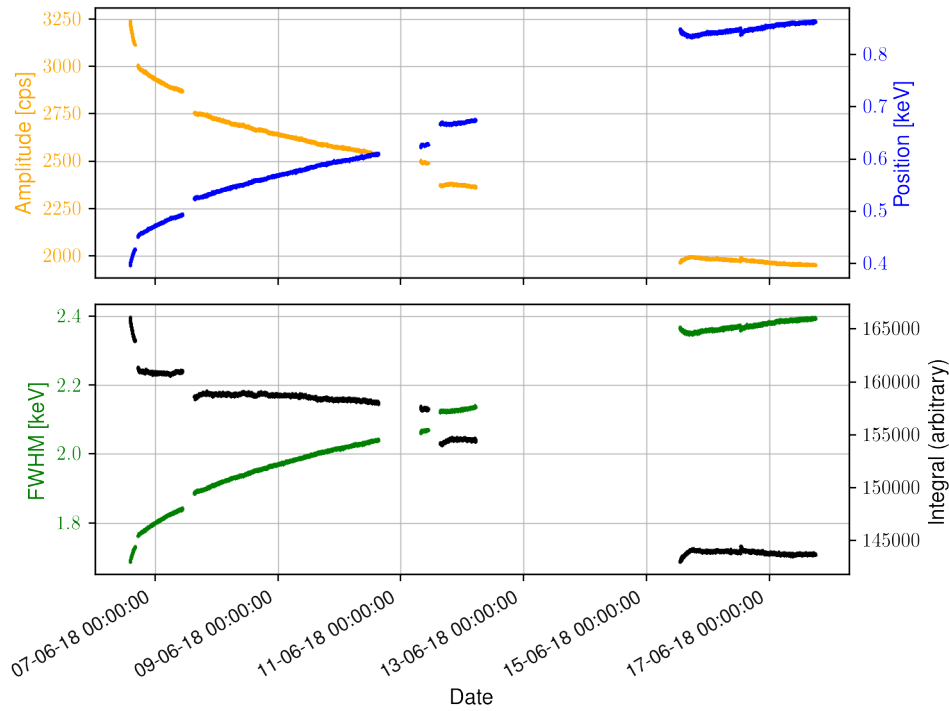
Figure 5.12:   The development of the noise peak parameters during the first tritium campaign. The properties are obtained from Gaussian fits to the noise peak in the sub-runs every minute. The noise peak moves toward higher energies and gets broadened while the amplitude and the rate drop. All four quantities share a significant correlation.

for the whole campaign (long term) but also for each region (short term) separately. On the one hand, there are quantities which change the electron flux in the CPS which include the source properties such as the tritium purity and the concentration of each competent of the WGTS gas mixture (D2, HD,....) and the magnetic field in the CPS. On the other hand, quantities exist which may cause an instability of the detector e.g. the noise level, temperature or magnetic field.

The tables 5.3 and 5.4 list all correlation which have an absolute Pearson correlation coefficient larger than 0.35. As an example several correlation plots with medium and strong correlation are shown in Fig. 5.13. There is medium correlation between D2 and HD concentration which is random since a causation is ruled out by a more detailed analysis [Zel18]. The tritium purity and the coil currents of the CPS magnets were stable during the whole campaign such that for now one has to assume the flux to be stable within the CPS. There is no further correlation to external sources.

There is a strong long term correlation between the rate, the temperature and the read out magnetic field strength. On short terms (within the regions) there is a weak correlation between rate and temperature only in region 3. There are still short term correlations between noise, temperature and magnetic field read out but not in all regions and sometimes the sign of the correlation coefficient changes. Hence, there are no clear internal correlation on short terms.

Examining the noise peak in the detector channels can give hints to the detector stability. Therefore the noise peaks are fitted with a Gaussian to extract their positions, widths and amplitudes. The noise level is unstable as one can see in Fig. 5.12. The peak moves continuously during the whole campaign toward higher energies while it gets wider and the amplitude as well as the number of noise counts decreases. Reasons for this behavior can be a detector drift, charge-up effects or degrading effects, e.g., due to radiation damage. Most likely this change of the noise peak (and/or the source of it) also causes a change of the position and width of a peak from mono-energetic electrons and hence a shift and shape change in the tritium spectrum. This needs to be investigated in future in more detail.

Summary on the tritium stability analysis During the whole tritium campaign a continuous increase in the count rate in both channels was observed. Also the measured shape of the tritium spectrum changes continuously. A change in the detector gain alone cannot be the reason. It cannot be excluded that there are two or more effects superimposed. The mean long term drift is stronger than for single time intervals which hints to an additional drift between these intervals in which the detector was taking background runs or performing a scan. So far there is no evidence that the flux at the CPS was not constant. There are no correlations between the rate and the source properties. The coil currents of the CPS magnets were stable. But there is a clear long term correlation between rate, noise level, Hall sensor and temperature read out, but no clear evidence for such correlations in short terms. In addition the noise peak changes as continuously as the spectrum such that a causation is considered.

The author of this thesis recommends, to further investigate the correlation between the noise and Hall/Temperature readouts. It could be possible that the sensors induce noise into the detector since the corresponding circuit paths and sensors are located close to each other. This can be done e.g. by taking background runs with and without powered Hall and temperature sensor or by monitoring the constant current sources of these devices.

S 1		S 2	Region	Pearson
Rate	vs.	Temp	3	0.35
		D2		0.41
		HD		-0.45
		Noise		-0.41
		HD	6	-0.37
Noise		Temp	1	-0.99
		Mag		0.98
		Temp	2	0.59
		Temp	5	0.71
		Mag		0.67
		Temp	6	-0.42
		Mag		0.63
Mag		Temp	1	-0.99
			3	0.56
			5	0.74
			6	-0.81

Table 5.3: Linear correlation test between quantities which may have causal links in short term. In this table the Pearson correlation coefficients between all quantities, which may be related to the short term (within the regions) rate drift during the first tritium campaign, are listed.

S 1		S 2	Pearson
Rate	vs	Temp	-0.78
		Mag	0.94
		Noise	-0.98
Noise		Mag	-0.77
		Temp	0.81
Mag		Temp	.0.95

Table 5.4: Linear correlation test between quantities which may have causal links in long term. In this table the Pearson correlation coefficients between all quantities, which may be related to the long term (whole campaign) rate drift during the first tritium campaign, are listed.
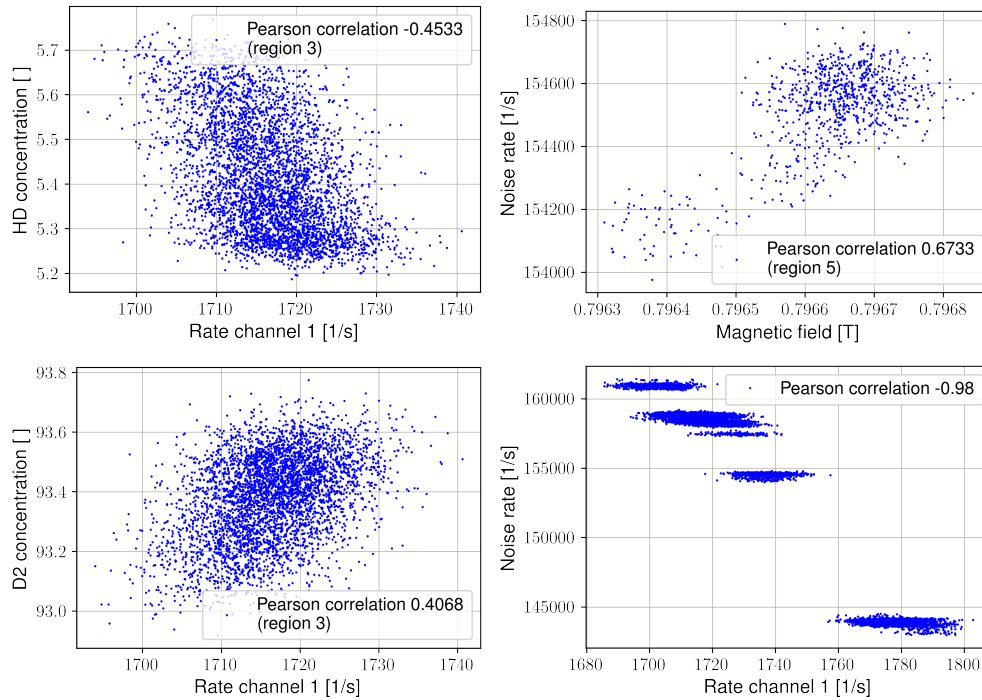
Figure 5.13: Correlation plots for selected quantities measured during tritium stability runs. The two left plots show a medium correlation between the FBM rates and the D2 and HD concentrations as they were measured with the LARA system. This correlation can only be found in short term (here region 3) but not for the full campaign. Most likely these correlations are random correlations [Zel18]. The top right panel shows an example for the medium to strong correlation between the magnetic field and the noise rate as it is observed in some regions (here region 5), see Tab. 5.3 for others. There is a strong anti-correlation between rate and noise rate in long term as one can see in the lower right panel.

5.5   RS e-gun during STSIIIa

During the STSIIIa measurement campaign, which took place from 10th September to 22nd October 2018, for the first time electrons from the rear section electron gun (RS e-gun, see Sec. 2.3.3) were detected with the FBM. The single electron peaks are investigated as well as the e-gun stability. Since there were not any changes be done to the FBM between the first tritium and the STSIIIa campaign the same calibration as given in Sec. 5.4.1 is valid.

5.5.1   Beam spot scans

The diameter of the beam at the exit of the e-gun was approximately $d_{gun} = 1\,mm$ [Beh18] and the pitch angle $0°$. The magnetic field B_{gun} at the e-gun was at 70% of its nominal value of $25\,mT$. The approximate size d_{fbm} of the beam spot at the FBMs position is then determined by the magnetic corresponding field strength B_{fbm} (compare with Eq. 2.8):

$$d_{FBM} = d_{gun}\sqrt{\frac{B_{gun}}{B_{fbm}}} = 0.14\,mm \qquad (5.1)$$

The beam size is therefore about 8.5 times smaller than the size $d_{det} = 1.2\,mm$ of the diode (type S5971). Since the beam is way smaller than the diode, one can rather speak of scanning the diode with the beams than vice versa. However, with the e-gun position fixed FBM scans were performed in a grid pattern with $0.1\,mm$ steps length to find the position of the beam spot. The result of such a scan is shown in Fig. 5.14. The scattered plots show the measured intensities in the x-y measuring plane. In the right plot the background is removed by a noise cut at $100\,cps$, i.e. only positions where electrons were detected are shown. The circles represent the entrance window (small, $\varnothing_1 = 1.2\,mm$) of the detector as it is stated in the data sheets and the visual surface (large, $\varnothing_2 = 1.3\,mm$) of the diode as it was measured. The position of the circles is such that the number of events within the circles is maximized. The center represents the actual position of the beam at $x_{FBM} = -1.2\,mm$ and $y_{FBM} = 7.6\,mm$.

As expected, within the entrance window the detection efficiency is similar at all positions. As an example the spectra obtained from one horizontal line (position 1 to 16) are shown below. Only at position 10 the detector measured a rate less than $2000\,cps$ but all spectra obtained within the entrance window (pos 4 - 14) are "good" e-gun peaks. Maybe the e-gun intensity dropped or the diode has some dirt at this position. Pos. 1 is only background. Unexpectedly, the detector responds to electrons hitting the detector outside the entrance window but in the close vicinity of 0.1 to $0.3\,mm$ around it. This regions is called "edge" from now on. The spectra obtained at these positions are distorted "bad" spectra. In case of a fully irradiated diode as it is the case during ^{83}Rb or tritium measurements the effects at the edges add a plateau-like background to the measured spectrum (see Fig. 7.3). In this scan the fraction of "bad" events is about 30%.
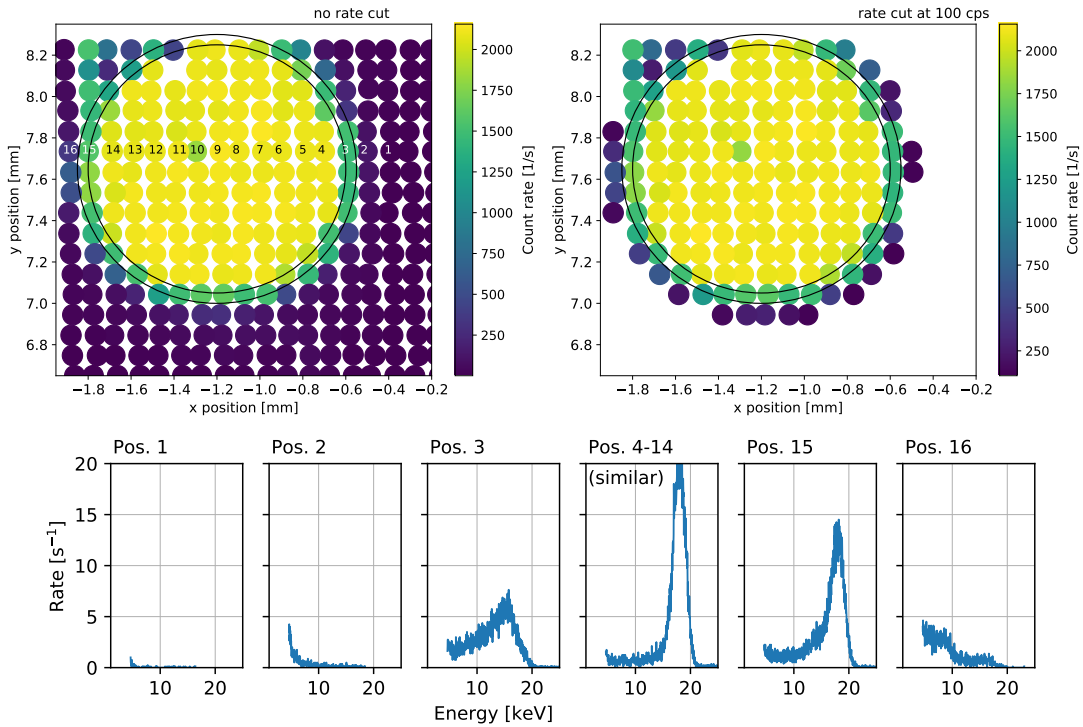
Figure 5.14: Scan of the RS e-gun beam. The beam is fixed and the FBM detector is moved through the beam in a grid with 0.1 mm step length. Each colored dot represents the measured rate at this very detector position. Note that the size of the data points is arbitrary and does not represent the size of the beam spot. The inner circle represents the active surface ($1.1\,\mathrm{mm}^2$) of the detector with the radius as stated by the manufacturer and the outer circle the visual surface of the diode. The detector profiles are positioned such that they comprise the highest rate. The spectra at the bottom were taken at the corresponding positions marked in the upper left panel.

5.5.2   E-gun peaks

With one of the scans from the last section it was ensured that the beam hits the detector in the center such that it is not expected that any electrons hit the edges of the detector. The obtained e-gun peaks in Fig. 5.15 are therefore "good" peaks in which no background from edge events are expected. As expected, the peaks are shifted toward lower energies because of the mean energy loss in the dead layer of about 0.7 keV (compare with Sec. 5.2.2) and they feature the characteristic long low energy tail. From simulations (see Sec. 7) a dead layer thickness of 340 to 345 nm and a detector resolution of FWHM = 2.35 keV are obtained. The latter value does not fit to the value (FWHM = 2 keV) obtained from the corresponding calibration measurements which is possibly caused by the change in noise level during the tritium campaign. This result needs to be verified with a further calibration measurement.
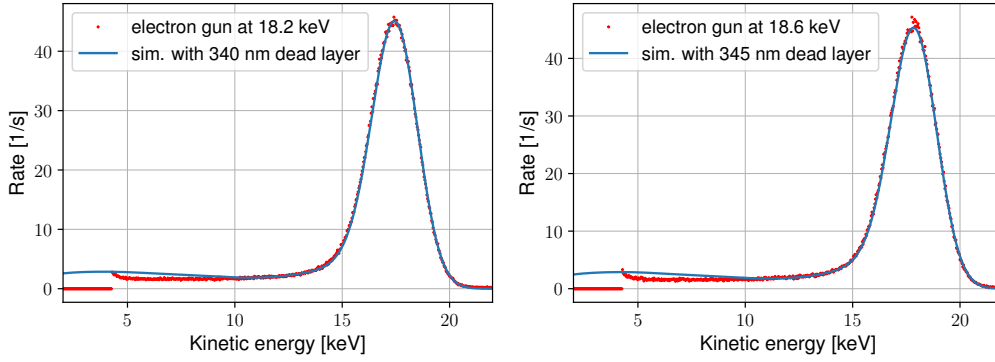
Figure 5.15:   Measured and simulated e-gun peaks obtained during the first tritium campaign. The simulation involves a detector convolution with FWHM = 2.35 keV energy resolution. The best results were obtained with dead layer thicknesses of 340 and 345 nm. The simulations overestimate the data at the low energy tail which is caused by an incomplete model which does not include the magnetic field configuration in the CPS. The bump is the result of reflected electrons which are guided back into the detector within the shaping time due to magnetic mirroring in the CPS.

5.5.3   E-gun rate stability

The long term rate stability was recorded for both light sources of the RS e-gun, the LDLS and the UV laser. The e-gun was set to approximately 18.6 keV. The rate trends are shown in Fig. 5.16.

The mean rate with the LDLS is about 2.8 kcps above the threshold of 5 keV. The rate varies within in 1 % (horizontal lines). Although with the UV laser very high rates can be achieved the rate was lowered to reduce pile-up in the FBM detector. The mean rate with the laser is about 8.9 kcps. The rate drops almost steadily during the measurement by 7 %. The positions of the single electron peaks during the measurements were stable and the shape of the peaks did not change.
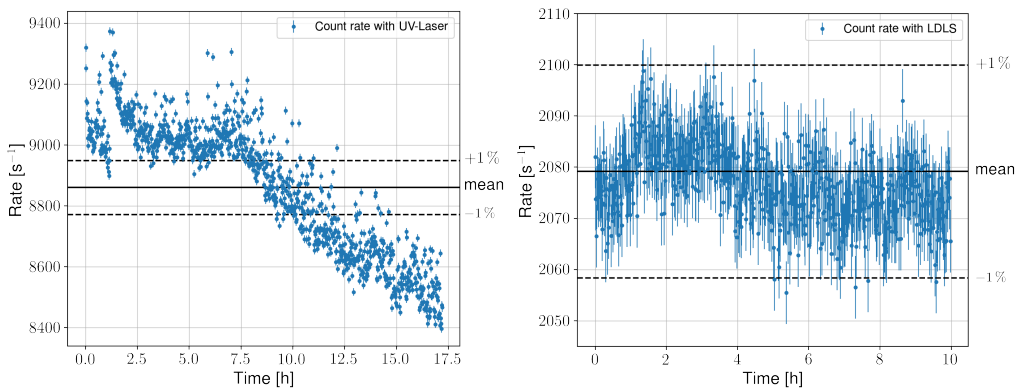
Figure 5.16:   Rate trend plot of stability measurement for the RS e-gun using the FBM. The LDLS measurement features rate variations in the 1 % regime in the [1h,4h] time interval but is stable within the statistic errors during the remaining time. The UV-Laser source is not stable and drops by approximately 7 % during the 17.5 hours measuring time.

91

5.6 Magnetic field analysis

In chapter 3 the magnetic field measurements were already utilized for the alignment by performing two-dimensional Gaussian fits to the data (global fit). In this section the data is analyzed in greater detail by analyzing the horizontal and vertical slices individually and comparing the data to numerical simulation which had been carried out by [Hau18] with Kassiopeia. Hereby the results of the global fits for the offsets x_0, y_0 and y_0^e as they are listed in Tab. 3.5 are used for the corresponding scans.

Data and simulations are compared for one scan (EnrK) in Fig. 5.17. The measured field is approximately 0.7% weaker than the simulated one, but this deviation is within the uncertainties of the Hall sensor [Sch17]. In the two lower panels the residuals are plotted with (right) and without (left) offset and y_0^e corrections. Without correction the residuals do not have the expected rotation symmetry. If corrections are applied the residuals are essentially symmetric. In the $y = 40\,\text{mm}$ region a step-like deviation can be seen which is probably caused by mechanical clamping of the y-mechanism. This can also be observed from outside at the small bellow which performs step-like jumps for large y-values. This step (or edge) can be seen in all scans and is even more dominant in a scan from bottom to top which underlines clamping as the error source.

In Figure 5.18 a more detailed analysis is illustrated in which the scan is stripped down into horizontal and vertical slices which enables the analysis at this very positions. For each slice in panel 1a separated 1D Gaussian fit is applied which is demonstrated for two slices (dashed lines) in panel 1a and 1c. The Gaussian means which represent the positions of maximum magnetic field are plotted for all slices in panel 2 and zoomed in for each direction in the panels 2a and 2b. From the residuals of the fits one can draw conclusions on the symmetry. Within the errors the field is symmetric in x while the edge causes an apparent asymmetry in y whose strength does not allow to draw conclusion about the field symmetry itself. Another systematic error is that the scans were not optimized to the position of the Hall sensor such that the vertical lines are bent.

5.7 Temperature dependance of Hall sensor

The calibration of the Hall sensor done by the author of Ref. [Sch17] includes a temperature dependence measurement. However, the experimental setup was not optimal: the detector board was cooled down with liquid nitrogen and warmed up in the ambient-air resulting in large temperature gradients in time and space which involves large uncertainties. Obtaining temperature dependence from measurements directly within the CPS is easier and more precise because the temperature range is only in the range in which the detector will operate and the temperature change is slow which lowers uncertainties in the Hall sensor's temperature determination.

The warm detector board was inserted into the cold CPS and it started immediately to cool down (compare with Sec. 5.4.2). The magnetic field settings were constant while temperature and Hall voltage were recorded during the cool down process. In Fig. 5.19 the Hall voltage is plotted as a function of temperature and reveals an essentially linear
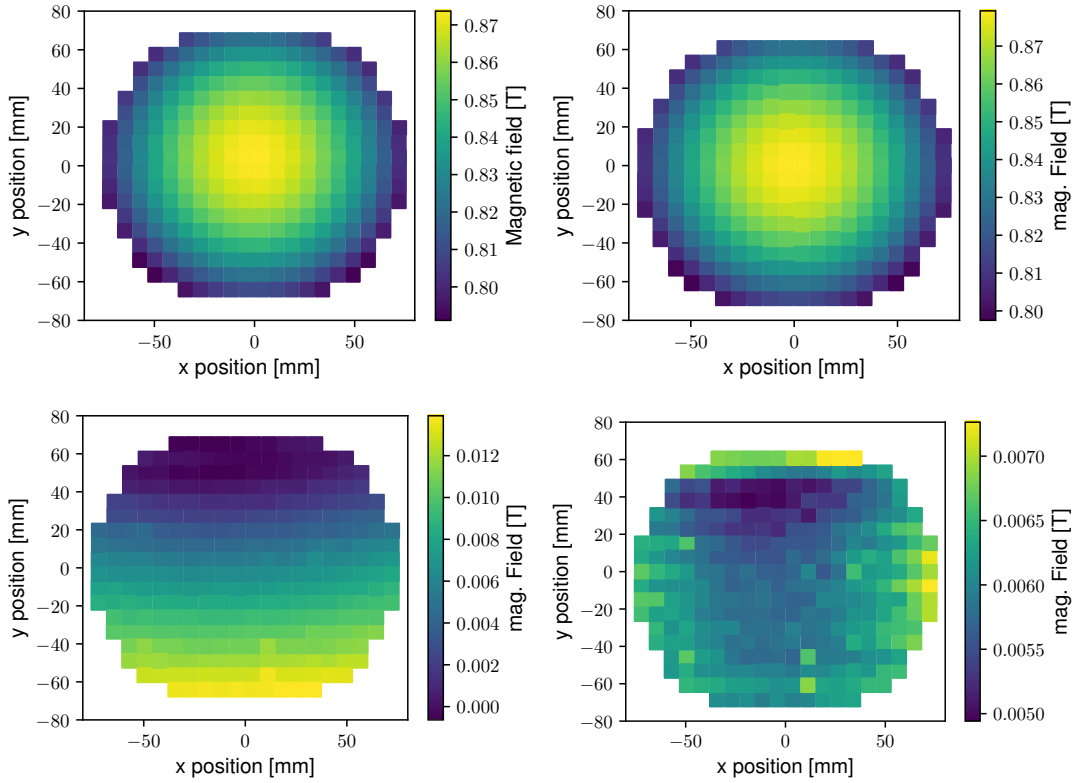
Figure 5.17: Measured and simulated z-component of the magnetic field in the CPS. **Top:** The measured field (left) is $0.7\,\%$ weaker than in the simulation. **Bottom:** Left the residuals without correcting for the offset between FBM and KATRIN coordinate system and right with correction. In the corrected plot the edge horizontally at $y = 40\,\text{mm}$ becomes visible which is caused by clamping of the y-movement mechanism.

dependence of $4.55 \cdot 10^{-4}\,\text{V/K}$ which was obtained by a linear least square fit. This value differs by a factor of 0.5 from the result in Ref. [Sch17] due to the reasons mentioned above.

5.8 Rate and magnetic field profile comparison

The electron flux in the CPS is determined by the number of tritium decays R and the magnetic flux $B_{\text{WGTS}}(r)$ in the WGTS (see Sec. 2.2.1) the acceptance angle θ at the exit of the WGTS and the ratio of the radial dependent magnetic fields at the FBM $B_{\text{FBM}}(r)$ and in the WGTS $B_{\text{WGTS}}(r_s)$:

$$R_{\text{FBM}}(r) = \frac{R}{2} \cdot (1 - \cos\theta) \cdot \frac{B_{\text{FBM}}(r)}{B_{\text{WGTS}}(r_s)} \tag{5.2}$$

Simulations reveal that B_{WGTS} is constant such that the electron flux is proportional to the magnetic field:
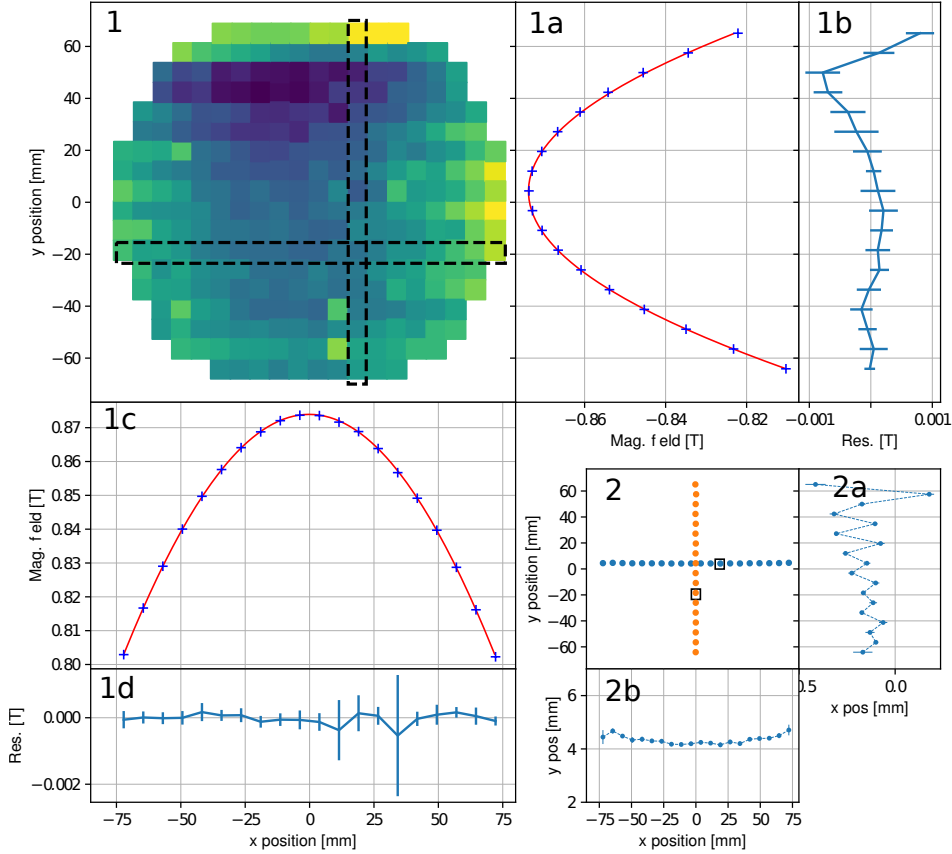
Figure 5.18: Slice analysis of the magnetic field data. The upper left plot shows the calibrated and temperature corrected magnetic flux data measured with the Hall sensor (here the residual to the simulations for visualizing edge). Horizontal (vertical) data point slices are fitted with a Gaussian to extracted the x (y) mean and the standard deviations and the residuals are calculated. This is shown for two selected slices (dotted boxes) in x and y. The residuals for x show that the field is symmetric within the uncertainties. The residual in y feature a bump where the clamping edge is located.

$$R_{\mathrm{FBM}}(r) \propto B_{\mathrm{FBM}}(r) \tag{5.3}$$

For verification the normalized Gaussian fit functions for the magnetic field and the rate from Sec. 5.4.4 are compared in Fig. 5.20. The radial rate distribution (blue) is narrower than the one for the magnetic field (orange). The discrepancy of the normalized intensity of about 1 % towards the outside of the flux tube is caused by additional effects. One effect is the dependence of the acceptance angle θ on the radial position of the electrons. In addition radial dependent reflections of the electrons at valve V0, which was closed during the measurements, explain the discrepancy sufficiently. The interested reader is referred to Ref. [Hau19].
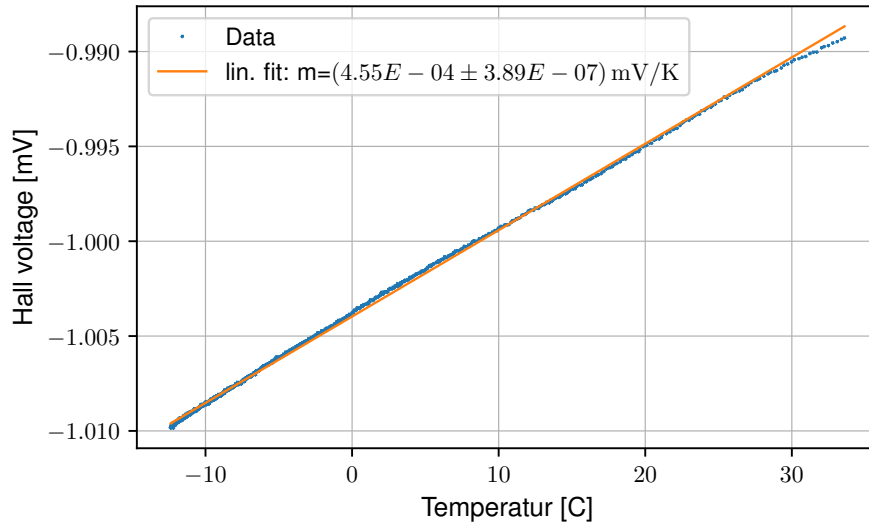
Figure 5.19: The Hall voltage as a function of temperature. There is an essentially linear but relatively weak dependency of approximately $0.045\,\%/K$.
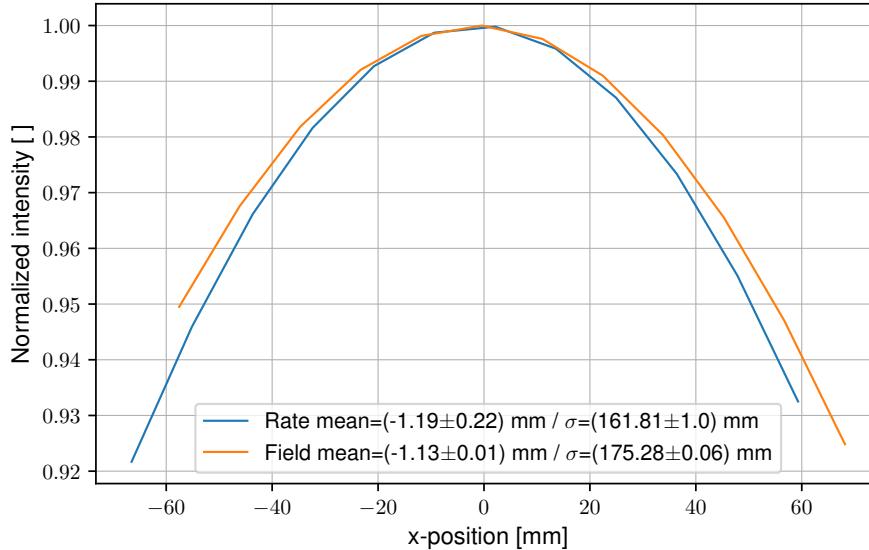
Figure 5.20: Comparison of the profiles of the electron flux and the magnetic flux. Plotted are the Gaussian fit functions derived from one of the double cross-scans (see Sec. 5.4.4). From theory the rate drops with the magnetic field which is not the case here. The rate distribution is narrower than the magnetic field distribution causing a deviation of approximately $1\,\%$ at the edges of the flux at $x = \pm 60\,\mathrm{mm}$.
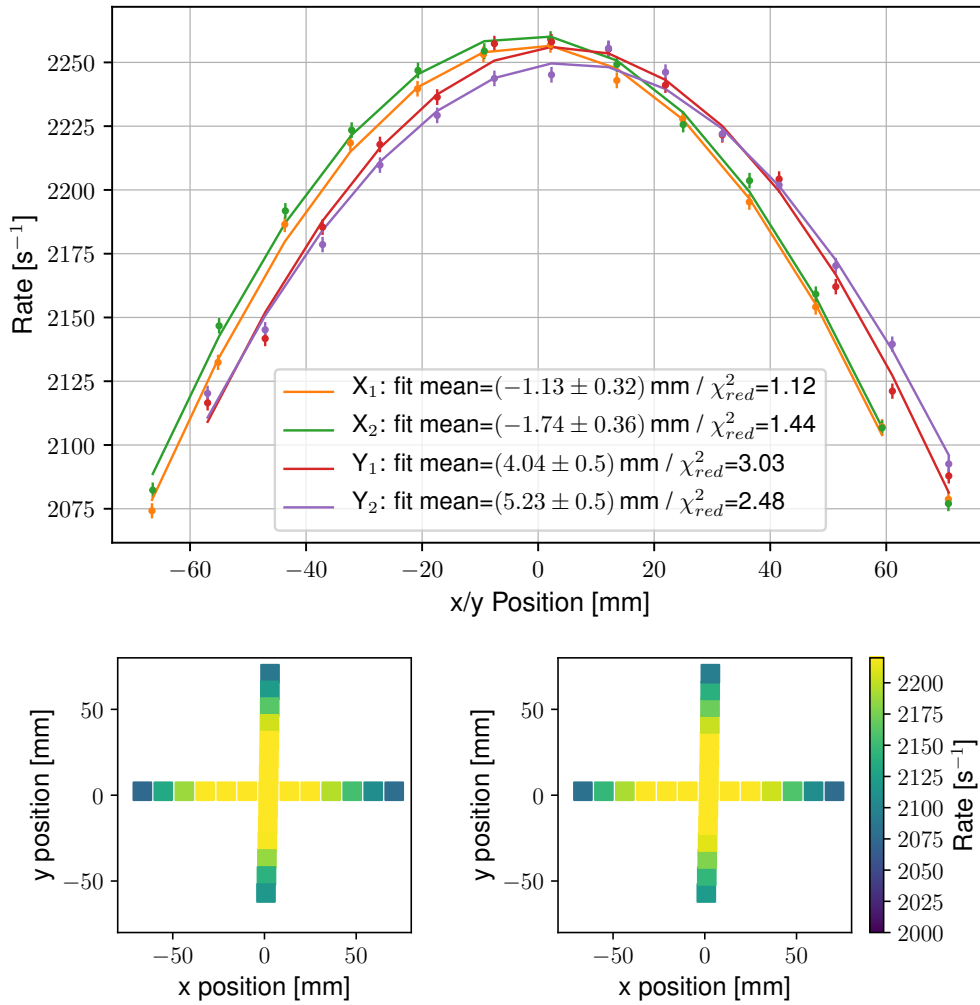
Figure 5.21:   Radial dependence of the count rate derived from a cross scan during the first tritium campaign (channel 2). The rate variations in channel 2 are larger resulting in worse fits.
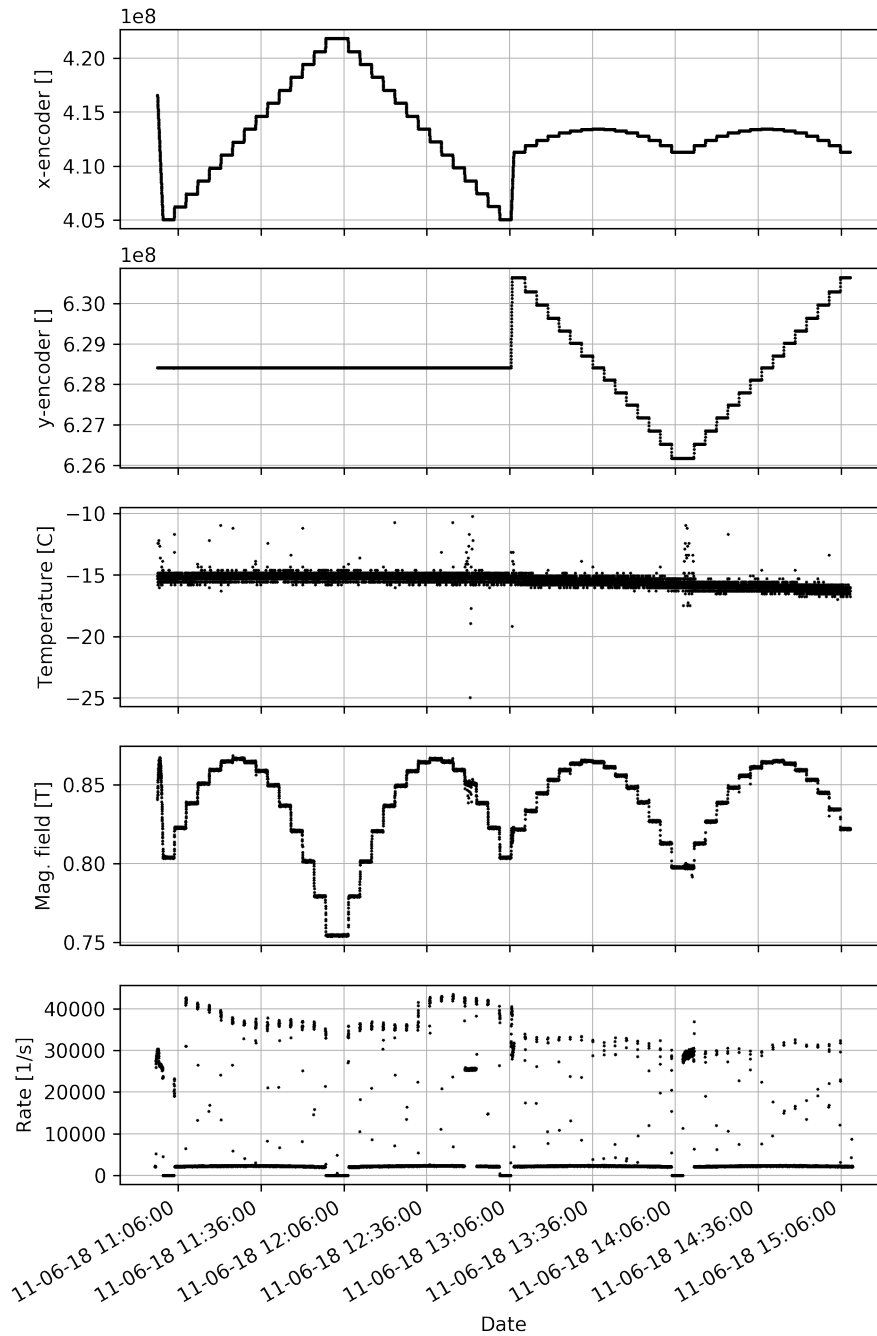
Figure 5.22: Measured quantities during a double cross scan (RUN 256). In a double cross scan the detector performs two scans for each direction: First two horizontal scans with y=0 ($X_{1,2}$) from opposite directions followed by two vertical scans ($Y_{1,2}$) with x=0. The temperature drops because during the scans the detector directly faces the 4 K cold beam tube of the CPS. The noise in the rate plot (rates above 3000 cps), which originates from the stepper motors, can be cut out since the information on the stepper motor statuses is logged, too.

6   Field emission electron gun

During the development of the FBM, electron sources were needed to perform test measurements and for characterizing the detector. Unfortunately, suitable sources were not available at the laboratory in Wuppertal. Therefore an electron gun (hereafter called "e-gun") was developed in the frame of the present work. This development is outlined in the following sections.

In section 6.1 the general working principle of an e-gun is shortly introduced and the requirements which the e-gun has to fulfill for the purpose of this work are listed. Section 6.2 gives a brief overview on the theory of the field emission effect. The following section 6.3 is about the preparation of sharp tips (radius $<100\,\text{nm}$) which are mandatory for field emission. The hardware setup of the e-gun is described in section 6.4 and the experimental setup as well as first measurements are presented in the final section 6.5.

6.1   Working principle and requirements

Electron guns allow to generate a narrow, collimated electron beam with an almost mono-energetic kinetic energy. All e-guns are formed of two basic components: an electron source (filament) and electrodes which accelerate and focus the electrons. Depending on the requirements, e-guns have different filaments and electrodes configurations.

The new e-gun must fulfill following requirements:

High electron flux The expected nominal electron flux at the FBM's monitoring position in the CPS is $O(10^6\,\text{mm}^{-2}\text{s}^{-1})$. The new e-gun should provide comparable values.

Energy The maximum expected electron energy is given by the end point of the tritium β-spectrum at $18.6\,\text{keV}$. The e-gun should provide electrons up to approximately $20\,\text{keV}$ kinetic energy.

No light emission The p-i-n diodes are extremely sensitive to visible and infrared light. Therefore the filament of the e-gun should not produce photons in this wavelength range.

Compatibility The e-gun must be compatible with the vacuum equipment in the Wuppertal laboratory.

Low production cost Only a limited budget is available.

In a thermionic e-gun the electrons are produced by a hot cathode, which is heated to create free electrons via thermionic emission. As an unwanted side effect these hot filaments also emit photons in the infrared and visible range. Preventing such photons from reaching the detector is technically challenging and the maximum flux of such filaments is relatively low. An alternative method to produce free electrons is the field emission effect (also known as cold emission). Field emission e-guns use cold filaments such that no heat or light is
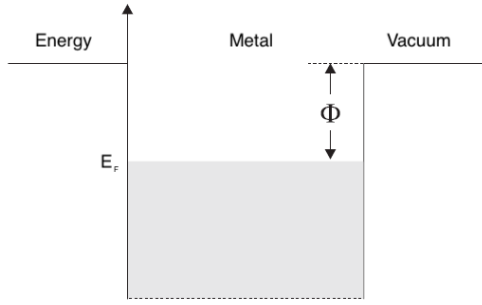
Figure 6.1: Diagram of the energy-level schema for electrons in a box-potential of a metal. The potential is filled with electrons to the Fermi level E_F. The gap between Fermi level and the vacuum level is called the work function Φ (≈ 3 to $5\,\mathrm{eV}$).
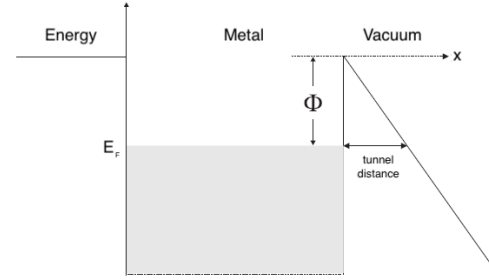
Figure 6.2: In the presence of a strong electrical field, the potential outside the metal is bent, such that an almost triangular barrier is formed allowing the electrons to tunnel though it.

produced. The electrons are extracted from the thin filament with intense electrostatic fields via the field emission process. The filaments are $O(100\,\mathrm{nm})$-thick tips (diameter of the tip) hence the electrons are accelerated from a almost point-like source such that the initial beam is thin which makes further focussing unnecessary. Since the filaments do not have to be heated the setup is rather simple, as it comprises only the emitter and an opposing anode.

6.2   Field emission

Generally an electron has to overcome the work function Φ (≈ 4 - $5\,\mathrm{eV}$) of the given material (see Fig. 6.1) in order to be emitted from a solid into vacuum. By introducing an electric field E_s at the surface of a metal, the potential barrier is bent as a result (see Fig. 6.2). For sufficiently intense fields the potential barrier becomes narrow enough allowing electrons the quantum-mechanic effect of tunneling through the barrier. This process is known as Fowler-Nordheim tunnel emission. The corresponding current density $j(E)$ is described by the Fowler-Nordheim equation for field emission:

$$j(E) = K_1 \frac{E_s^2}{\Phi} \cdot e^{-K_2 \cdot \Phi^{\frac{3}{2}}/E_s} \tag{6.1}$$

where K_1 and K_2 are material constants.

In pure metals field emission occurs in electric fields typically in order of $O(10^9\,\mathrm{V/m})$ and strongly dependents on the work function Φ.

To create such strong field for example in a plate capacitor with a plate distance of $d = 1\,\mathrm{mm}$ a voltage of $V = E \cdot d = 10^9\mathrm{V/m} \cdot 1\,\mathrm{mm} = 1\,\mathrm{MV}$ is needed. But the dielectric strength of vacuum is only 20–40 kV/mm. The solution is to utilize intense fields which

occur at sharp edges or tips of electrodes. The electric field at a tip is proportional to the squared inverse of the radius:

$$E_{tip} \propto \frac{1}{r^2} \xrightarrow{r \to 0} \infty \tag{6.2}$$

As a result: if the radius is sufficiently small, the necessary electric field for field emission can be achieved for any applied voltage. The tips of the e-gun in the scope of this work feature a radius of $r = O(100\,\text{nm})$ such that at an electrode distance in mm range only electrode voltages of several kiloelectron volts are needed to reach the necessary electric field strengths ($O(10^9\,\text{V/m})$) at the tips. As a positive side effect of the moderate voltages the hardware requirements are lower. The next section deals with the production of these thin tips.

6.3 Tip preparation

For producing sharp tips from polycrystalline wires the electrochemical etching procedures have been well established for more than 60 years and are described in several books and articles. For this work the easy to use so-called "lamellae drop-off technique" is used which is described in detail in Ref. [Kle97]. The base material is a $0.2\,\text{mm}$-thick tungsten wire which undergoes electrochemical etching to form the sharp tip. The etching of the tungsten wires has been carried out in an electrolytic solution of 2 N sodium hydroxide (NaOH). Tungsten reacts with sodium hydroxide and water producing water-soluble sodium tungstate and hydrogen. The simplified equation [Kar00] of the chemical processes is

$$\text{W} + 2\text{H}_2\text{O} + 2\text{NaOH} \rightarrow 3\text{H}_2 + \text{Na}_2\text{WO}_4. \tag{6.3}$$

The setup for the etching process is illustrated in Fig. 6.4. A ring electrode is used as a cathode in which a drop of the electrolyte forms a thin film (lamella). The tungsten wire is etched in this lamella and at the end of the process, the lower part drops into a cushioned container. The etched end of this part is very sharp and used as the e-guns filament. The tip is cleaned after the etching process in distilled water, isopropanol and acetone. But a layer of tungsten (tri)oxides remains on the tip which leads to an inhomogeneous work function. The common method to removed this layer is by heating the tip within the vacuum chamber but this is not possible with this e-gun since filament heating was not considered in favor of simplification.

6.4 The e-gun and the experimental setup

The e-gun is mounted on a DN100 to DN40 CF reducing piece. Two high voltage feedthroughs (maximum 25 kV DC voltage) on a DN40 flange are used for the electrical feeding. The e-gun is formed by three electrodes (see Fig. 6.5 and 6.7).
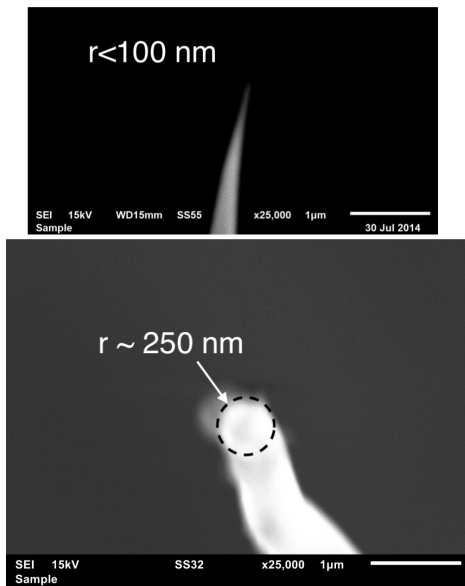
Figure 6.3: SEM picture of the sharp tungsten tips produced via electrochemical etching. The radius of the tips is in order of $O(100\,\mathrm{nm})$.
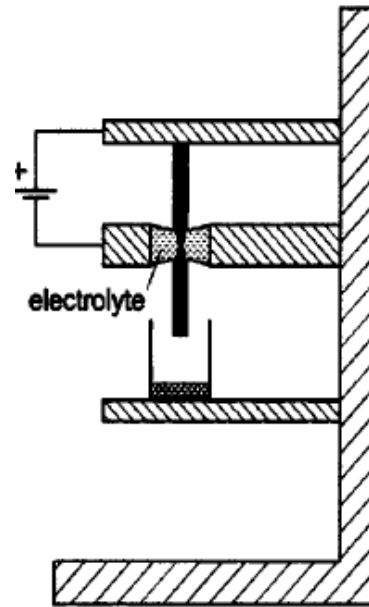
Figure 6.4: The experimental setup for electrochemical etching of the tungsten wires with the "lamellae drop-off technique". In a ring electrode a drop of the electrolyte forms a lamella in which the $0.2\,\mathrm{mm}$-thick tungsten wire is etched. The etching voltage is about 3 to 9 V and the procedure lasts about 5 to 15 minutes. The etched end of the lower part is very sharp and used as filament for the e-gun. Figure taken from Ref. [Kul03].

Back plate (K_1) To keep the high voltage part simple the back plate is directly mounted onto one of the vacuum feedthrough's electrodes which reduces the possibility of sparks and unwanted field emission. It includes a central mounting point for the tip holder. The negative voltage V_1 applied to the back plate is the final acceleration voltage.

Front plate (K_2) The front plate is the middle stage of the electrode system and is connected to the second electrode of the feedthroughs. Its voltage influences the electrical field at the tip and therefore the field emission properties.

Ground plate (K_3) The ground plate is electrically connected with the main flange (ground potential) such that the electrons have reached their final energy when passing it.

The plates are electropolished to minimize unwanted field emission. The front and the ground plate are held and separated by PEEK distance holders which are connected to the main flange. The electrodes of the feedthroughs are insulated with ceramic beads. Additionally polyimide tape covers high voltage parts which may have sharp edges such that electrons from unwanted field emission are stopped. Table 6.1 lists the setup parameters.
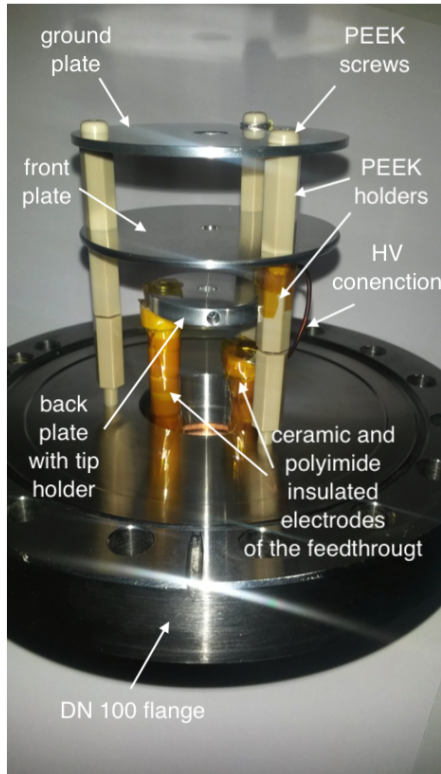
Figure 6.5: Picture of the Wuppertal field emission e-gun.
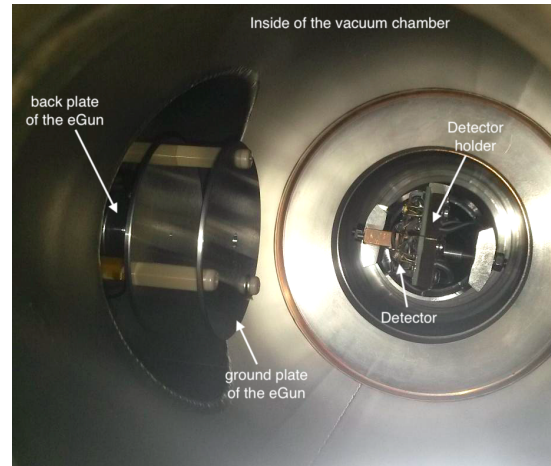
Figure 6.6: Picture of the experimental setup for e-gun measurements in Wuppertal.

For the measurements the e-gun is attached to a DN100 outlet of a DN160 vacuum chamber (see Fig.6.6). The distance between the e-gun (ground plate) and the detector is approximately 10 cm. Two separate high voltage supplies are connected to the electrodes. The best achievable vacuum for the vacuum chamber is about 10^{-6} mbar.

6.5   Measurements

A scheme of the e-gun setup is illustrated in Fig. 6.7 (also compare with Fig. 6.1) highlighting the principle functionality. Two cathodes (K_1 and K_2) and one anode (K_3) are arranged in an order such that electrons ejected from K_1, which is set to the desired acceleration voltage V_1, are accelerated to K_3 which is at zero volts. Downstream of K_3 the electrons have their final energy. The voltage V_2 at cathode K2 does not change the final energy of the electrons but determines the shape and strength of the electrical "extraction" field at the tip.

Detector response

The electron spectrum at the bottom of Fig. 6.7 is taken with the shown configuration above. The spectrum shows the typical properties of an electron peak taken with a detector

front and ground plate diameter/ thickness	64.5 mm/ 2 mm
diameter of aperture in front/ ground plate	5 mm/ 8 mm
distance between front and ground plate	20 mm
back plate diameter/ thickness	15.5 mm/ 5 mm
distance between back and front plate	13 mm
diameter on edges	0.5 mm
acceleration voltage	8 to 20 kV
extrusions voltage	2 to 8 kV
tip diameter	$< 100 - 500$ nm

Table 6.1:   Parameters of the e-gun setup.

which features a dead layer and a none zero shaping time. The peak position $E_e = V_1 e - E_{loss}$ is shifted to lower energies due to the mean energy loss E_{loss} in the dead layer, the lower energy flank descends into a plateau which is formed by partial charge collection, and a pile up peak is formed at $E_{pile} = 2 \cdot E_e$. The peaks can be fitted with a combination of a Gaussian and an error function, similar to Sec. 4.6.1 but without the escape peak since it only occurs with photons.

Stability

The field-emission process is generally unstable. The e-gun as developed in the present thesis showed several features. Not all of them were reproducible. Following behaviors were observed.

1. After setting the back (K_1) and front plate (K_2) to the desired negative acceleration voltage ($V_1 = V_2$), the voltage of the front plate V_2 is increased slowly such that voltage difference $\Delta V = V_2 - V_1$ increases i.e. the electrical field at the tip increases. The field emission process starts step-like such that the measured intensity jumps from zero to high rates which can not be measured with the detector. After this sudden increase ΔV can be lowered again to adjust the count rate to a sufficient level.

2. During the measurements the rate varies by a factor of about 2 and drops in long term.

3. The field emission process sometimes stops unforeseeably.

There is no clear rule at which voltage or voltage difference the upper features appear. Nor is there a certain time interval for how long the field emission process can be held up. Although stability was not required for the e-gun since detector stability measurements are performed with the ^{83}Rb source, an increased stability would simplify the handling of the e-gun which may be relevant for projects in the future. The reason for points 1 and 3 is possibly that the field emission takes place over a large part of the tip instead of only
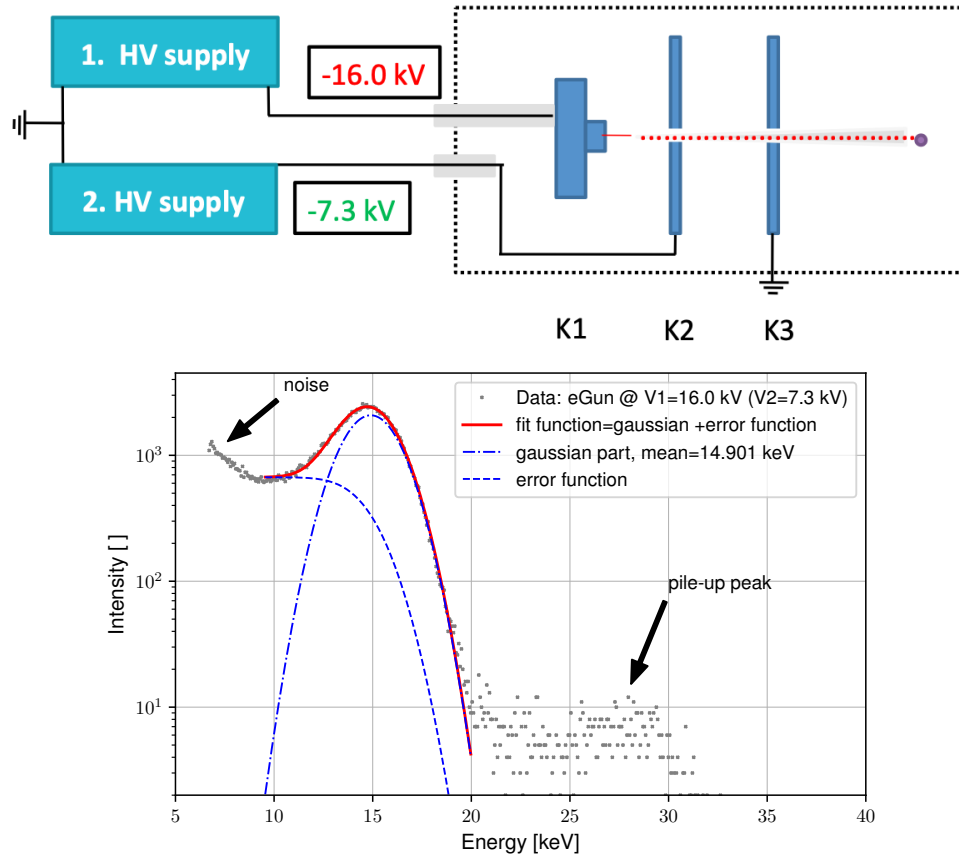
Figure 6.7: Illustration of the working principle of the e-gun. **Top:** Schematic of the e-gun setup. Two power supplies provide the cathodes K1 and K2 with negative voltages V_1 and V_2 receptively. In this example $V_1 = -16\,\text{kV}$ is chosen for the desired final electron energy of $16\,\text{keV}$. V_2 does not change the final energy but determines the electrical field at the tip. Cathode K3 is ground such that the electrons will have reached their final energy after passing it. **Bottom:** The electron peak obtained for the upper example in logarithmic scale. The position of the peak is shifted to a lower energy due to the energy loses in the dead layer. Because of the hight rate a pile-up peak is formed.

the very end of the tip. Therefore electrical field simulations (see Fig. 6.8 and 6.9) were performed with Kassiopeia to understand how the fields at the tip look like. The strong field can be limited to the very end of the tip by dipping it deeper into the detector holder. Tests are outstanding.

6.6   Summary and outlook

A field emission e-gun which emits electrons with energies of 5 - 20 keV was developed, built, tested successfully and the first use of the e-gun was the determination of the dead layer of one of the *p-i-n* diodes. However, the e-gun showed strong intensity instabilities during operation which impeded the handling. The stability can be increased in three ways:

1. Field emission gets more stable with lower pressure. This thesis proposes to use a
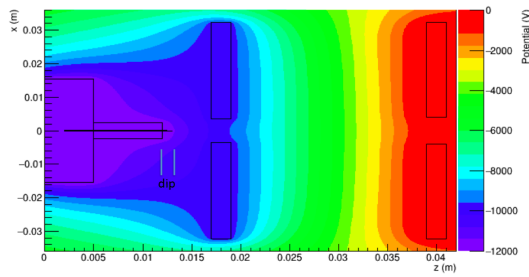
Figure 6.8: Simulated electrical field of the e-gun.
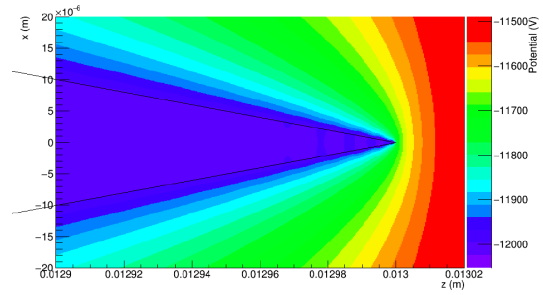
Figure 6.9: Simulated electrical field of the e-gun. (zoomed)
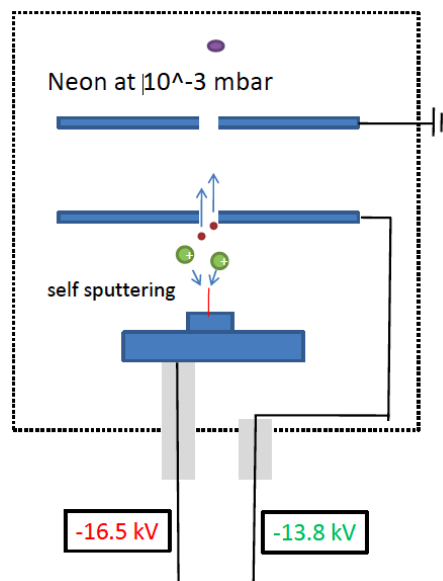
Figure 6.10:   Annealing the tip with self-sputtering.

UHV vacuum chamber to reach pressures below 10^{-7} mbar.

2. Simulations were carried out which show, that the strong field gradient comprises only the very end of the tip if it is dipped deeper into the tip holder. This limits the electron emission to a smaller area such that the e-gun may work more stable.

3. In [Ekv99] it is proposed to anneal the tip to clean and sharpen it for higher rates and more stability. The described method is called self-sputtering. The vacuum chamber is filled with neon at 10^4 mbar and the e-gun is in normal operation (see Fig. 6.9). The electrons from the field emission of the tip ionize the neon atoms. The positive neon ions get accelerated towards the tip bombarding it. During the sputtering process an increase of the count rate can be monitored. The expected annealing time is about one hour.

7   Simulations

To understand the detector response of the FBM a detailed Monte Carlo model for the passage of electrons from vacuum into a silicon detector was developed within the GEometry ANd Tracking (Geant4+PENELOPE) simulation toolkit [Ago03].

7.1   The model

The model of the detector comprises a detection volume and a fully insensitive dead layer (also known as slab-model). Within the detector the electrons undergo elastic and inelastic scattering losing their energy subsequently. As an example, in Fig. 7.1 (left) the projected electron tracks of a simulation with 30 electrons of 10 keV initial energy is shown. The electrons lose a fraction of their energy in the dead layer. Due to the scattering kinematics of similar particles (electron-electron scattering) the scattering angles can be relatively large such that the primary electrons can be reflected into the dead layer and even fully reflected out of the detector.

In the present example the mean energy loss in the dead layer is about 1 keV and approximate 17 % of the electrons are fully reflected. Only energy losses within the detection volume are added to the event. In the right panel of Fig. 7.1 a 18.6 keV electron peak, which was measured with the FBM at a detection rate of 2 kcps, is shown. The long, low energy tail, as a result of partial charge collection, can readily be identified. The low energy region (A) is predominantly produced by reflected electrons and region B mainly by the dead layer losses which also cause the shift of the main peak (C) by approximately 0.6 keV (mean energy loss in the dead layer).

The predicted energy spectra are compared to the experimental single energy electron spectra (e-gun) and ^{83}Rb spectra. The following steps are performed to obtain the best fit:

1. Electrons are simulated matching the source properties

2. For each source property, simulated spectra were generated for different dead-layer thicknesses

3. To take the electronic noise into account, the Geant4 spectra are convolved with a Gaussian probability distribution such that the experimental detector resolution is matched (typically $2 - 2.4$ keV FWHM)

4. The measured electron spectrum is compared to the library of simulated spectra with χ^2- tests. Before the comparison the simulations are normalized to the peak with the highest energy from the measured spectra.

With this method good fits (see Fig. 5.15) could be obtained for measurements in which only the center of the diode is irradiated as it was the case during the Rear Section e-gun measurements (see Sec. 5.5). The low energy tail is always slightly overestimated which is
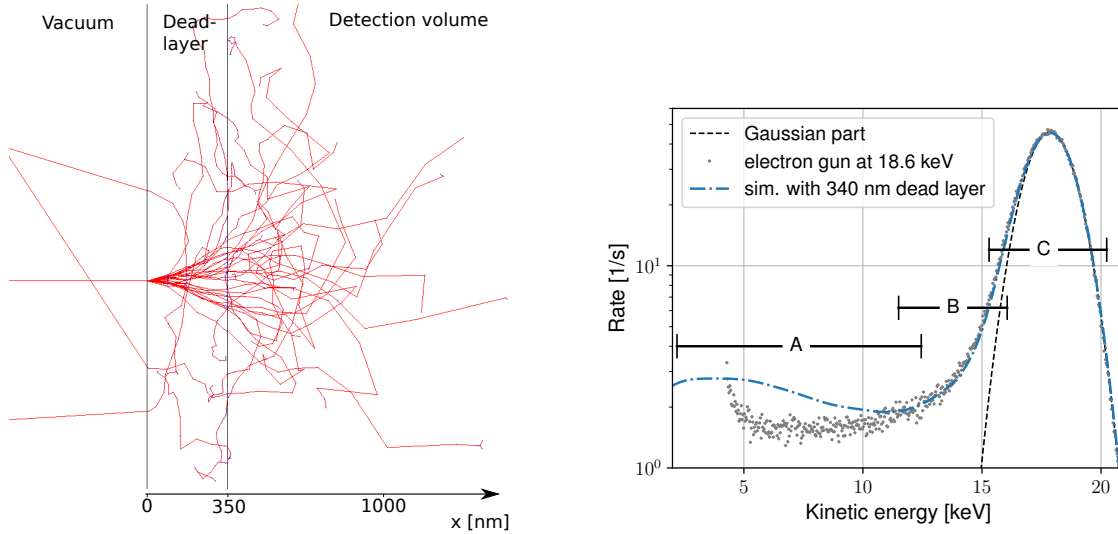
Figure 7.1: Numerical simulation of electrons entering and interacting with a silicon detector. **Left:** Thirty 10 keV initial electrons (red) are passing from vacuum from perpendicular direction into the detector. The detector model uses a 350 nm-thick dead layer, which is completely insensitive, and the detection volume which is fully sensitive. Within the detector the electrons lose energy by many subsequent elastic and inelastic scattering processes. Secondary electrons can be produced (blue). The scattering angles can be large such that electrons may leave the detector again i.e these electrons get reflected. **Right:** Electron spectrum (18.6 keV) and the best fit. The low energy tail (A and B) originates from partial energy deposit.

due to fact that electrons which get reflected from the detector are back reflected into the detector due to the magnetic fields in the CPS. This happens within the shaping time of the DAQ such that it is registered as a not reflected event which results in a less intense region A in Fig. 1.1. Magnetic mirroring is not considered in this model. The interested reader is referred to [Hau19].

7.2 The edge of the diode (edge correction)

It was never possible to achieve good fits for measurements in which the diode was irradiated completely, as it is the case for the ^{83}Rb and tritium measurements. The simulations always underestimate the data (compare with Fig. 7.4) for lower energies. The results from the e-gun scan in Sec. 5.5.1 allow the assumption, that such spectra include events from electrons which hit the detector in the narrow area of approximately 0.1 to 0.2 mm outside but in the immediate vicinity (edges) of the sensitive area. This increases the efficiency of the diode but these additional events undergo different or additional partial charge collection processes as one can see in the corresponding spectra measured at Pos. 2, 3, 15 and 16 in Fig. 5.14. This is not considered in the model as described above so far in which only a slab-model dead layer is assumed in the sensitive area and a fully non-responsive diode outside. In the following section the method for correcting this effect is described.
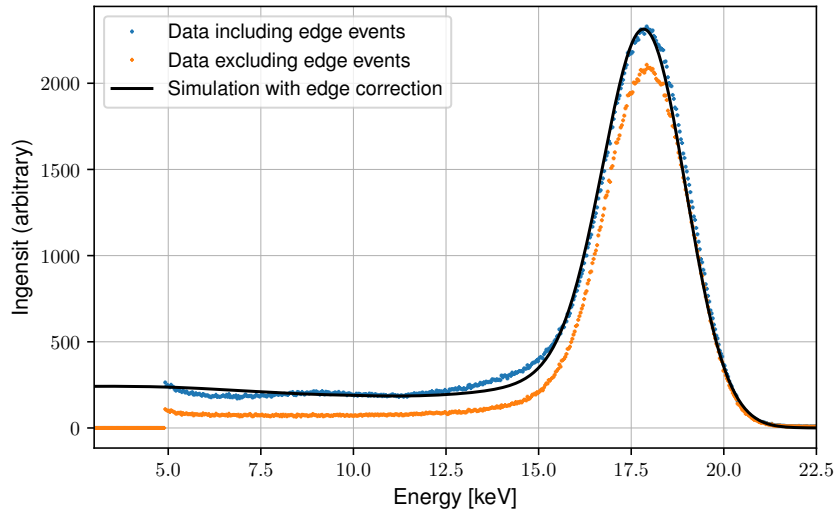
Figure 7.3: Simulation with edge correction. The orange spectrum only includes electrons which hit the detector within its sensitive area. If including events from electrons which hit the detector outside of the sensitive area (see Sec. 7.3) the response of the detector changes (blue) basically by an additional plateau left from the peak.

Edge correction

The events which occur at the edge of the diode (see Sec. 5.5.1) clearly undergo more partial charge collection than events within the sensitive area. The precise geometry of the diode's edges is unknown but it is fair to assume that its rather complex. However, to take these edge effects into account it is assumed that each event has a certain possibility to happen at the edges, which is expressed by the edge factor f_e, and undergoes further scattering after the passage through the basic dead layer. The result is a higher plateau at the low energy side of the peak. Technically this is done by adding a plateau to the low energy side of each bin after the simulation with Geant4 (between step 2. and 3.). If the number of events in the bin is I_b then the plateau has the hight $I_{plateau} = I_{bin} \cdot f$. There is no additional free parameter.
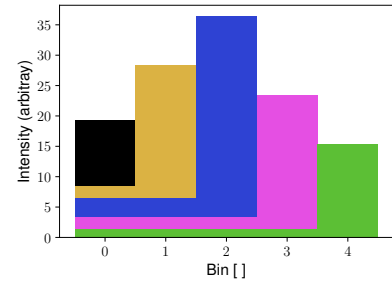
Figure 7.2: Edge correction with the bin-wise method. Bin i rides up on plateaus created by a particle charge collection of electrons in bin i+j (j=1, 2 ,3 ...).

The e-gun scan (see Sec. 5.5.1) which enables looking only into events from electrons hitting the sensitive area (e.g. Pos. 4 - 14) also allows adding events from electrons which hit the edges (e.g. Pos. 1, 2, 3, 15 and 16). Because the scan is performed in a grid-like structure this is a reasonable approximation for a completely irradiated diode as it is the case for ^{83}Rb and tritium measurements. Figure 7.3 shows the spectra obtained including (blue) and excluding (orange) edge events. The additional events lift the peak onto a plateau. The simulation includes the edge correction which leads to a good fit. As next this method is applied to the electron spectrum of ^{83}Rb.

During commission in Wuppertal several ^{83}Rb spectra were recorded. One of such a spec-
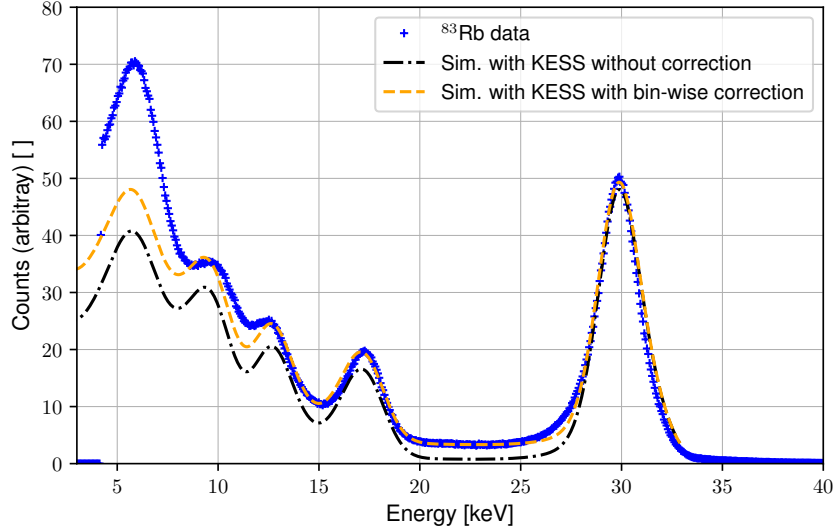
Figure 7.4:   Measured and simulated ^{83}Rb spectrum. The ^{83}Rb data (blue) is measured with a S5971 diode. Without edge correction the simulation underestimates the data (black). With edge correction (yellow) the simulation describes the data well above 8 keV but underestimates the data below this value.

trum is shown in Fig. 7.4 together with the simulation results. Without taking the edge effects into account the simulation underestimates the data below 27.5 keV. The simulation with the edge correction describes the data well down to 8 keV but still underestimates the data below that energy. A possible reason for the underestimation can be the large uncertainties (23 %, see Tab. A.5) in the relative intensity of the 7.5 keV conversion electrons. However, the bin-wise edge correction is a simple but effective approach to deal with the additional "none-perfect" events which occur at the edges.

The edge factor obtained from the best fit is $f_e^{Geant4} = 1.41$ for Geant4 and $f_e^{KESS} = 0.0019$ for KESS. KESS [Ren11] is a further Monte Carlo simulation toolkit commonly used in the KATRIN collaboration for dead layer simulations [Wal14, Hau19].

7.3   Efficiency of the detector

To determine the intrinsic efficiency of a detector, the number D_D striking the entrance window needs to be known. In practice, large uncertainties are involved to determine D_D for small detectors which are close to a radioactive source or if using an e-gun of which the flux is not properly known. In addition, the experimental setup for detecting reflected electrons or electrons which are not transmitted through the dead layer, is complex. Therefore numerical simulations are performed to obtain these quantity. The probabilities for electrons for getting reflected before reaching the sensitive volume (P_r), stopped in the dead layer (P_d) and for not exceeding the energy threshold of 5 keV ($P_d(5\,keV)$) are determined for initial electron energies from 3 to 20 keV.

The efficiency can be calculated by $\varepsilon_x = 1 - P_x$ ($x = r, th, d$). The intrinsic efficiency of the detector is then given by $\varepsilon_i(5\,keV) = \varepsilon_r \cdot \varepsilon_d \cdot \varepsilon_{th}(5\,keV)$. The results are shown in
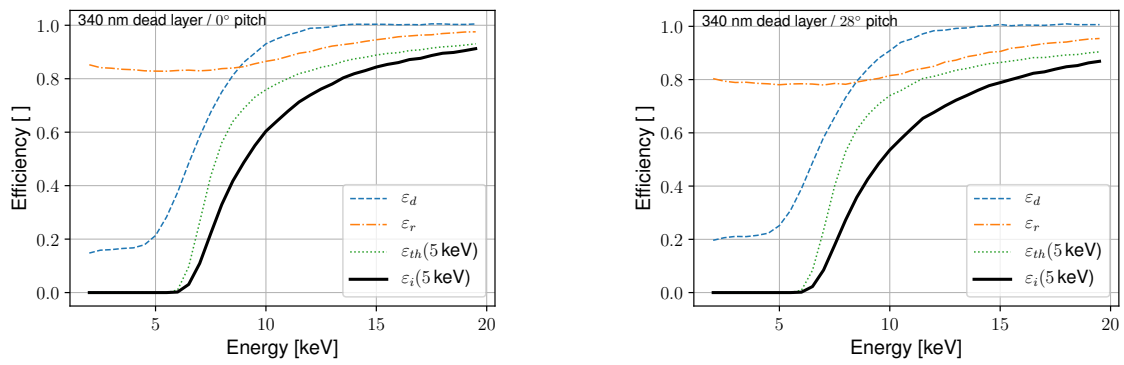
Figure 7.5:   The simulated efficiency of the p-i-n diode with a $340\,\text{nm}$-thick dead layer as they are used for the FBM.

Fig. 7.5 for the inclination angles of $0°$ (electrons velocity perpendicular to the diode) and $28°$ (maximum for nominal tritium runs). Applying this result to the simulated tritium spectrum ([Hau19], electron flux in the CPS) results in a counting efficiency for tritium of approximately $40\,\%$ i.e. the FBM sees $40\,\%$ of the spectrum at a threshold of $5\,\text{keV}$.

8 Summary and outlook

The work presented in this thesis is the development, investigation and integration of the Forward Beam Monitor (FBM) into the KATRIN experiment. The experiment aims for a precise measurement of the shape of the tritium beta spectrum at its end-point region in order to determine the mass of the electron antineutrino with a sensitivity of $0.2\,\mathrm{eV/c^2}$ at $90\,\%$ confidence level. One of the major systematic uncertainties in this measurement arises from instabilities related to the high luminosity tritium source. An unaccounted shift of the column density, for example, would result in a shift of the observed neutrino mass. In order to reach the design goal of KATRIN, the fluctuation of the column density must be measured on the per-mil level. Therefore the source is continuously monitored by several monitoring systems, one of which is the FBM.

Within the scope of this thesis a UHV compatible vacuum manipulator was developed. It is able to place the detector board directly into the beta electron flux originating from the tritium source. Although the mounting position of the apparatus demands a movement mechanism with a working stroke of $1.8\,\mathrm{m}$ the FBM is able to reach any position within the electron flux cross-section with a precision of $0.1\,\mathrm{mm}$ which can be determined with magnetic field measurements.

Furthermore the detector board, which is situated at the tip of the FBM manipulator, was developed which measures the electron flux with two silicon p-i-n diodes. The FBM detector reaches an energy resolution of about $\sigma_{\mathrm{FWHM}} = 2\,\mathrm{keV}$ at an energy threshold of $5\,\mathrm{keV}$. The readout electronic was optimized to be able to register electron events at a rate of $O(10^4\,\mathrm{cps})$ and thus to measure relative changes in the electron flux with $0.1\,\%$ precision in about $100\,\mathrm{s}$.

The entrance window (dead layer) of the p-i-n diodes has a great impact on the detector response when measuring electrons. To understand the related effects in order to reach the required precision for the FBM numerical simulations were performed. From these simulations it was found that the p-i-n diodes used for the FBM have a $350\,\mathrm{nm}$-thick dead layer causing an energy dependent shift of the measured peak of 0.5 to $2\,\mathrm{keV}$ for electron energies up to $20\,\mathrm{keV}$. The peak itself widens and develops a long low energy tail descending in a basically flat plateau.

After commissioning, the FBM was deployed for several KATRIN measurement campaigns including the very first measurement with tritium. The capabilities of the FBM detector could be confirmed as well as the positioning accuracy of the manipulator. A long term (days and weeks) drift of the rate was observed which correlates to a drift of the noise level. In short terms (hours) the FBM is stable to the per-mil level.

For the commissioning of the FBM, electron sources were needed to test the detector. Besides the provision of an ion implanted rubidium source, an electron gun was developed for this work. It takes advantage of the field emission effect and provides a narrow electron beam with energies from 5 to $20\,\mathrm{keV}$.

To summarize, the work presented in this thesis led to the realization of a monitoring device which reaches all design goals.

Based on these findings the following items should be addressed in future works.

- During the first tritium measurements a low pile-up rate (in the order of a few percent) was expected such that the data is used for tritium analysis without any pile-up corrections. In nominal KATRIN pile-up rates above 10 % can occur such that this effect may not be neglected anymore. Therefore a dedicated study on the pile-up behavior of the DAQ is proposed. Simulated beta spectra, which already considered the dead layer effect, were carried out in Ref. [Hau19]. These spectra can be used to predict the impacted pile-up e.g. by performing simulations utilizing Eq. 4.16 or using the simulation software DRIPS which is included in Kasper, KATRIN's simulation framework.

- By now only the AC part of the preamplifier signal is processed (events, spectrum) which is decoupled from the DC part in the second preamplifier. However, the DC offset is a measure of the mean energy deposited in the detector and hence can also be used for stability analysis. This has not been tested yet but a read-out channel is already provided as well as the cabling. A new preamplifier with outputs for the DC signal would easily provide this new feature which usefulness still needs to be investigated. In addition the second stage preamplifier would benefit from a temperature sensor.

- During first measurement campaigns a shift of the noise peak was observed. At the same time a shift in the spectrum and hence in the count rate was measured. A lot of effort was invested to understand if there is a causal link between the two and if the gain of the detector might have drifted. This could not been answered before opening and recalibrating the detector. The analysis of the FBM data would benefit from a repeated calibration measurement with the RS e-gun performed in certain time intervals. This thesis proposes three electron energies 10, 15 and 18 keV.

- In case the FBM is opened for maintenance (e.g to place new cables into the tube for the FBM-TRISTAN project) it is recommended:
  - to exchange the long aluminum rod by a stainless steel rod to decrease y-movements of the detector due to temperature changes.
  - to check for abrasion at all movement parts, especially at the toothed rod and the groove which were coated with tungsten disulfide. If in doubt one must consider to revise the part.

- In case the field emission e-gun will be used for future projects it is proposed to revise the high-voltage system. In addition, the vacuum setup should be upgraded to be UHV compatible and the tip annealing method with gaseous neon must be tested. In addition the handling of the e-gun would benefit from a read out of the emission current.

A major detector upgrade for the FBM is already planned. The TRISTAN project (Tritium Beta Decay to Search for Sterile Neutrinos) will take advantage of the high luminosity tritium source of KATRIN after the nominal neutrino mass data-taking has ended. It aims to confirm the existence of the sterile neutrinos which has been predicted in numerous

theories. Therefore the KATRIN main detector will be replaced by a new silicon multi-pixel detector system. The TRISTAN detector utilizes novel silicon drift detectors with a dead layer only $100\,\mathrm{nm}$ thick. It records spectra with an energy resolution of about $\sigma_{\mathrm{FWHM}} = 140\,\mathrm{meV}$ and features a energy threshold less than $2\,\mathrm{keV}$. The interested reader is referred to Ref. [Mer18]. One of these detector chips will be tested in the FBM at the end of 2019 and if this test is successful the FBM might be operated permanently with the TRISTAN upgrade such that the neutrino-mass runs of KATRIN can already benefit from its excellent performance.

A Appendix

A.1 Thermal simulations

Typically the energy resolution of a silicon detector decreases if the temperature of the detector rises which is mainly caused by thermally activated charge carriers into the conduction band. The dark noise of the detector chip rises which increases the voltage noise. Hence one tries to keep the temperature low, at least below room temperature. The temperature scenario in which the detector board is located during nominal operation in the CPS is rather complex and already described in Sec.4.7. Although the FBM detector is surrounded by cold beam tubes (at temperatures at least 77 K) its temperature was found to be unexpected hight up to 50 °C during the first measurements in the CPS. Therefore numerical simulations were performed using the simulation framework COMSOL multi-physics.

Besides three parts of the front end, namely the backplate, the front end lever arm and the cover, all other components are simplified in the geometric model. The long bellows, the vacuum components of PP2 and the interior of the CPS are idealized by cylindric shapes. This measure not only eased the modeling but also speeds up the simulation time. The thermal conductivity and emissivity coefficients for each component are set corresponding to their material:

Component	Material	λ [Wm^{-1}K^{-1}]	ϵ [ ]
Detector board	polyimide/ ceramic	0.12/18	0.86/0.9
back plate	aluminum	237	0.08
CPS	stainless steel/ gold plated	14.4/345	0.55/0.02
electrical comp.	plastics	0.2	0.95
Inner rod			
Bellows			
Long tube	stainless steel	14.4	0.055
PP2 components			
CPS			
stainless steal			

Table A.1: List of materials and thermal properties as they are used for thermal simulations. Given are the thermal conductivity λ and the emissivity ϵ coefficients.

In the simulations the inside surfaces of the outer boundary are set to a fixed temperature. Here the walls of the CPS are at 77 K while the bellows and PP2 are at room temperature. The electrical components of the detector board can be set to produce a certain thermal power. Both heat conduction and heat radiation are included into the simulation. For the latter some small and cold ($\propto$ T^4) surfaces are excluded to reduce computation time.

In figure A.2 the resulting temperature contribution of the FBM is shown for the case of a not gold plated (left) and a gold plated CPS beam tube (bottom). Two-thirds of the

interior of the FBM remain at room temperature while the other one-third features a large temperature gradient down below $0\,°\text{C}$. Due to its high reflexivity the gold coating of the CPS beam tube acts as an insulator resulting in a $25\,°\text{C}$ higher temperature than calculated with a stainless steel surface. This is one of the reasons why the board temperature is higher than expected. Another reason arises from the board itself as one can see in Fig. A.3. With the $1\,\text{mm}$-thick polyimide board V1 the electrical components reach temperatures up to $50\,°\text{C}$. With a ceramic board, which features a thermal conductivity 15 times greater, this temperature can be lowered by $30\,°\text{C}$. Hence, to reduce the temperature of the electrical components it is recommended to increase the heat flow from the electrical components to the back plate and reducing the power consumption of the preamplifier circuit.

Instead of using ceramics for the new detector board V2 a thinner ($0.2\,\text{mm}$) multilayer board, which consists of alternating polyimide and copper layers, is used. To further increase the heat flow the new board is contacted through from the FET ground contacts to the back layer of the board (made of copper), and then glued directly to the backplate. Additionally the power consumption was reduced (see Sec. 4.5.2). These countermeasures reduced the board temperature below $0\,°\text{C}$ (compare with Sec. 5.4.2).
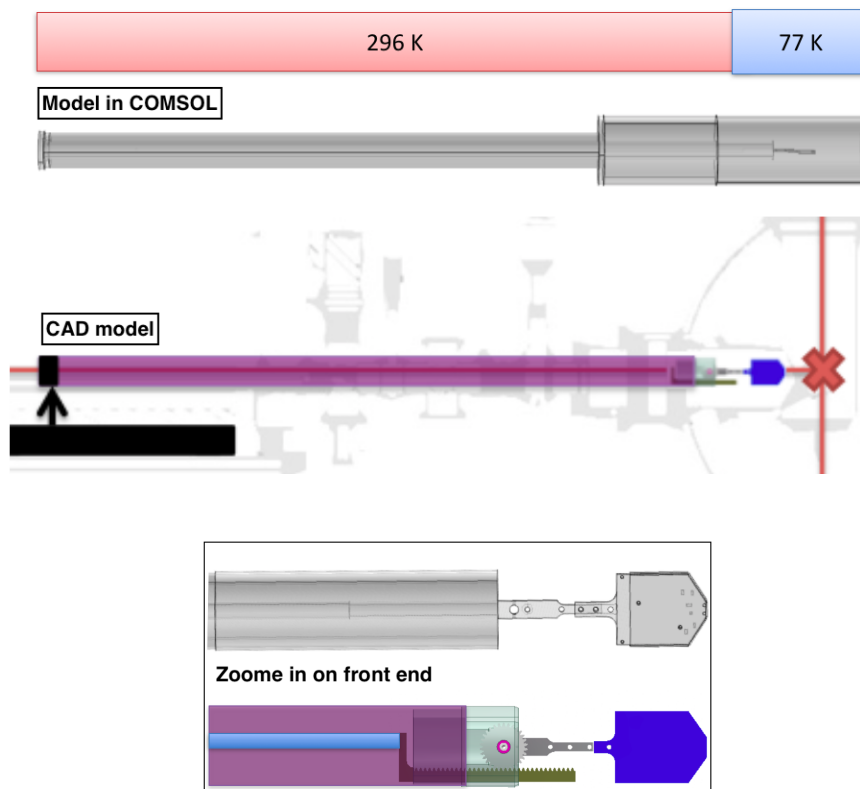
Figure A.1:   The geometric model of the FBM in the thermal simulations. To shorten the simulation times, the long bellow, the vacuum parts of PP2 und the CPS chamber are idealized by cylindric shapes. The complete back end is removed as well as the toothed wheel and rod of the frond end. The walls of the setup are set to $77\,\text{K}$ or room temperature for walls located inside or outside the CPS chamber, respectively.
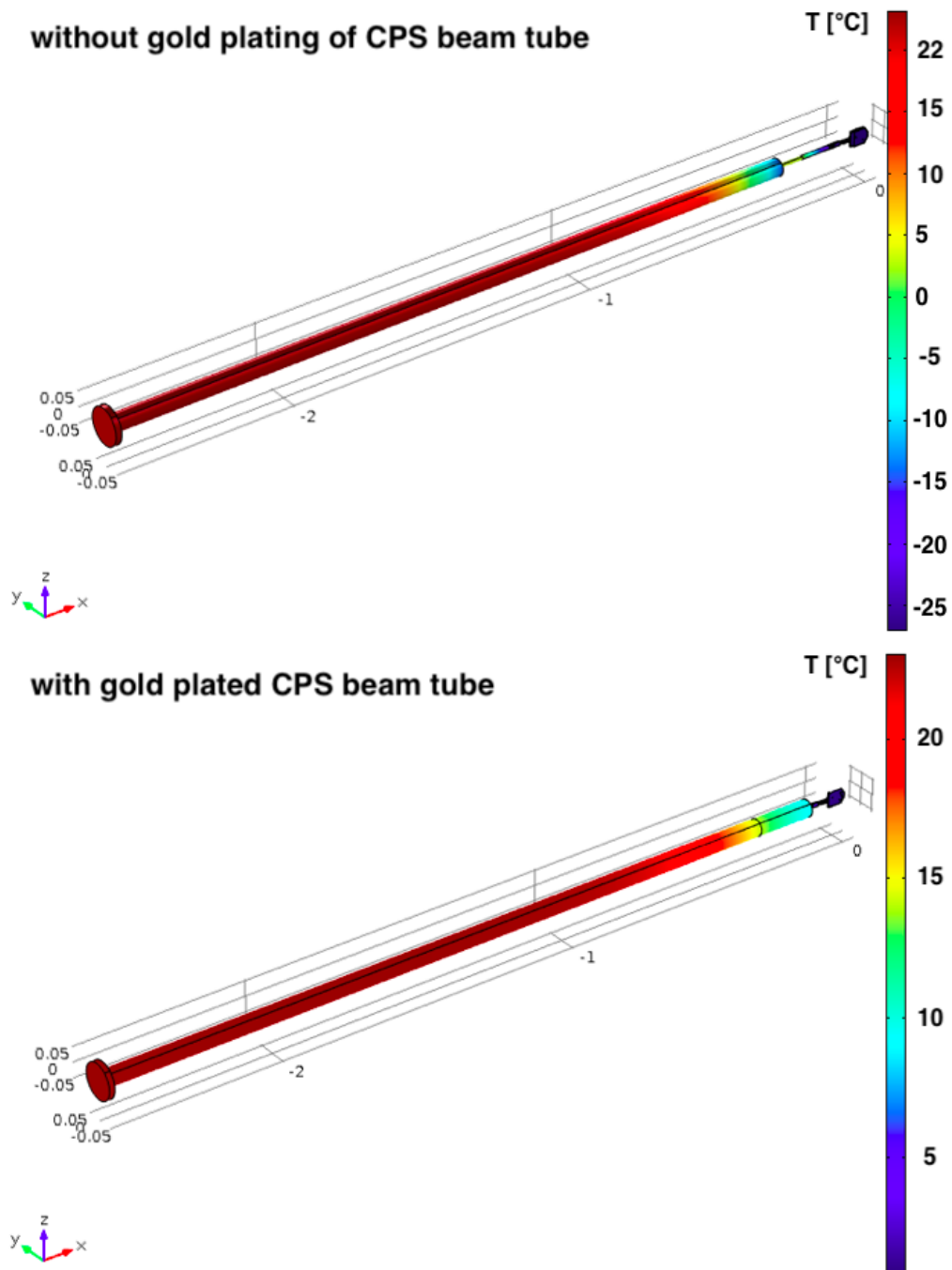
Figure A.2: Thermal simulations of the FBM with and without gold plated CPS beam tube. In general about two-thirds of the inner parts of the FBM remain at room temperature and the front end features the lowest temperature. Due to its hight reflectivity the gold plating in the CPS acts like an insulator for the heat radiation such that the final temperature of the FBM is about 25 °C higher than for a beam tube which is not gold plated.
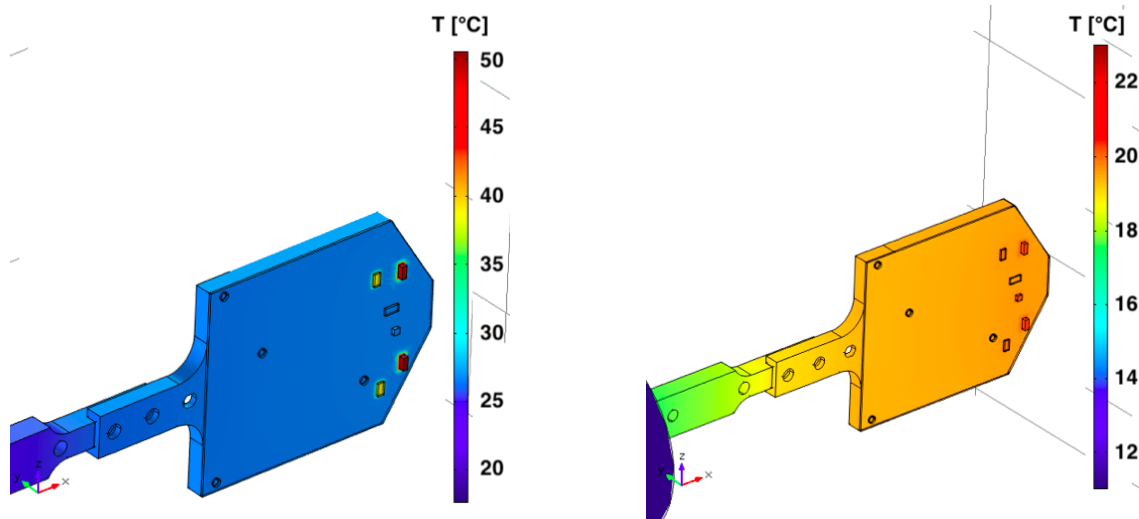
Figure A.3:   Thermal simulations of the FBM front end. The temperature of the electrical components reaches up to 50 °C with the polyimide board (left, board V1). The same simulation but with a ceramic board instead results in a reduction of these temperature of about 30 °C.

A.2   Detector boards

Channel	Location	Hardware number	Analysis number	ID	DAQ
1	bottom	322-RRP-8-5000-00	322-CHN-0-5000-00	1	PX 5 (322-EBU-0-2010-00)
2	top	322-RRP-8-5100-00	322-CHN-0-5001-00	0	DP 5 (322-EBU-0-2000-00)

Table A.2: Allocation and KATRIN numbers of the DAQ.

Board	Channel 1 diode	Channel 2 diode	type	Measurement time
1			V1	Test
2			V1	Test
3	S9055 ($0.031\,\mathrm{mm}^2$)	S5972 ($0.5\,\mathrm{mm}^2$)	V1	Krypton measurement campaign, July 2017
4	S5971 ($1.1\,\mathrm{mm}^2$)	S5971 ($1.1\,\mathrm{mm}^2$)	V1	Test
5	S5971 ($1.1\,\mathrm{mm}^2$)	S5971 ($1.1\,\mathrm{mm}^2$)	V2	First tritium, May 2018 and STSIIIa, Sep 2018
6	S9055 ($0.031\,\mathrm{mm}^2$)	S5973 ($0.12\,\mathrm{mm}^2$)	V2	NxT tritium, from Feb 2019

Table A.3:   An overview of the different FBM boards used for different measurement campaigns. The main differences between the boards are the size (and type) of the p-i-n diodes and the type of the PCB. Board V1 is a 1 mm-thick polyimide PCB which is only fixed with screws to the back plate while board V2 is a 0.2 mm-thick polyimide PCB which is additionally glued to the back plate for better thermal conductivity.

A.3   Radiation sources

Peak	E [keV]	rel. I	decay mode/assignment
γ-peak ^{241}Am (59.54)	59.5412	35.9	α
γ-peak ^{241}Am (26.34)	26.3448	2.4	α
γ-peak ^{241}Am$_s$	31.4	-	α
	32.183	0.01746	α
	33.1964	0.126	α
X-ray peak ^{237}Np L$_l$	11.871	0.66	^{237}Np L$_l$
X-ray peak ^{237}Np L$_{\alpha1,\alpha2}$	13.761	1.07	L$_{\alpha1}$
	13.946	9.6	L$_{\alpha2}$
X-ray peak ^{237}Np L$_{\eta,\beta1-\beta2}$	15.861	0.153	L$_{\eta}$
	17.751	5.7	L$_{\beta1}$
	16.816	2.5	L$_{\beta2}$
	17.992	1.37	L$_{\beta3}$
	17.061	1.5	L$_{\beta4}$
	17.505	0.65	L$_{\beta5}$
	16.109	0.184	L$_{\beta6}$
X-ray peak ^{237}Np L$_{\gamma1-3,\gamma6}$	20.784	1.39	L$_{\gamma1}$
	21.099	0.65	L$_{\gamma2}$
	21.342	0.59	L$_{\gamma3}$
	21.491	0.29	L$_{\gamma6}$
Photo electrons peak	48-50	-	-

Table A.4:   An overview of the strongest ^{241}Am gamma and x-ray lines below 60 keV[SC].

Electron	Energy [keV]	Intensity
CE L	7.4847 8	81 % 19
CE M	9.1177 12	13 % Z
CE N	9.3817 10	1.3 % 3
Auger K	10.8	36.5 % 21
CE K	17.8260 9	17.3 % 24
CE L	30.2306 8	44 % 6
CE M	31.8636 11	7.4 % 10
CE N	32.1276 9	0.55 % 7

X-ray	Energy [keV]	Intensity
XR l	1.59	5.5 % 5
	9.4057 6	5.9 % 14
XR k2	12.598	19.9 % 13
XR k1	12.651	39 % 3
XR k3	14.104	2.77 % 19
XR k1	14.111	5.4 % 4
XR k2	14.311	0.71 % 5
	32.1516 5	

Table A.5:   An overview of the strongest ^{83}Rb lines below 33 keV.

A.4   Electronic schematics and board layouts
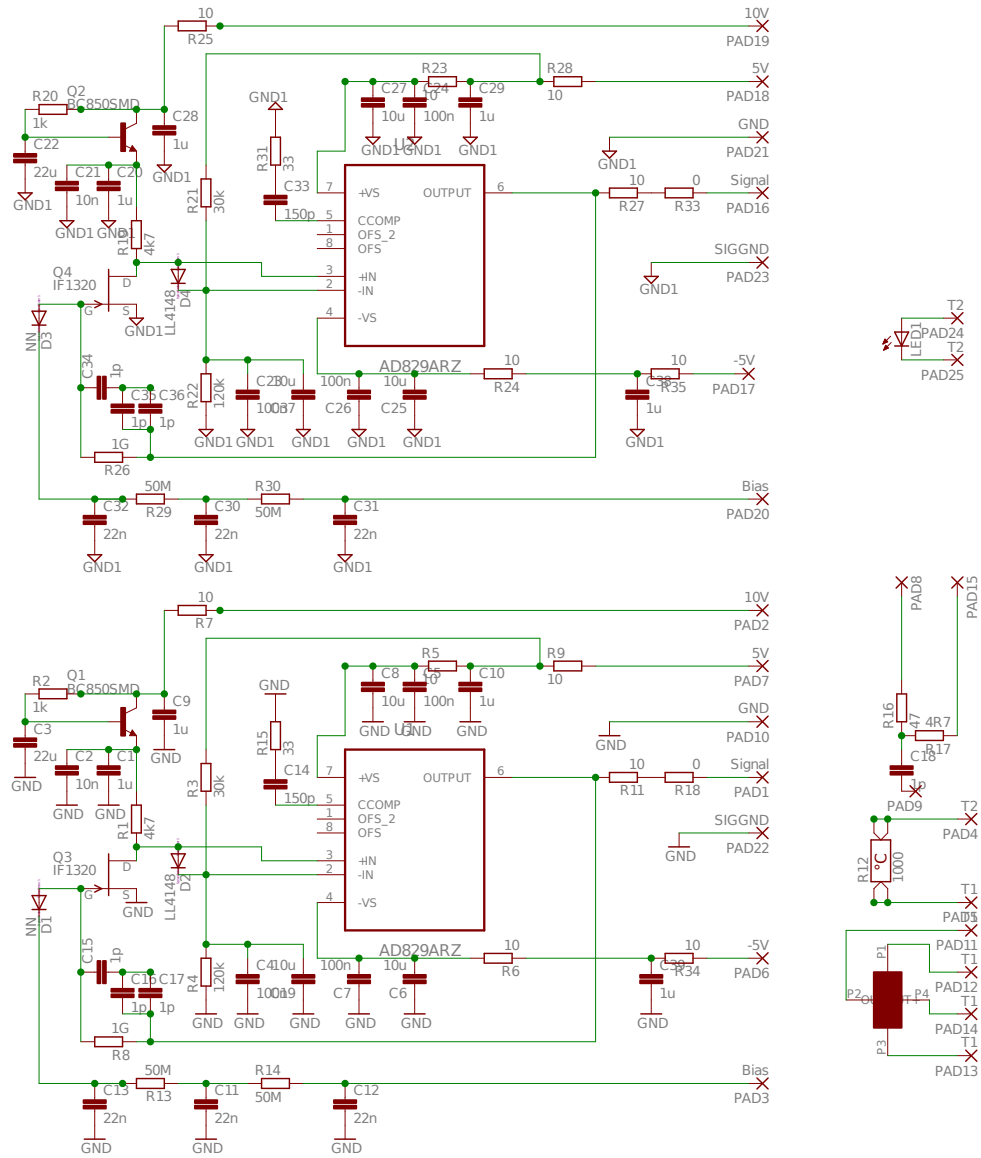
Figure A.4: The circuit layout of the detector board. The drawing shows the electronic layout of the two equivalent charge sensitive preamplifiers as well as the Hall-sensor, the temperature gauge and LED circuits.
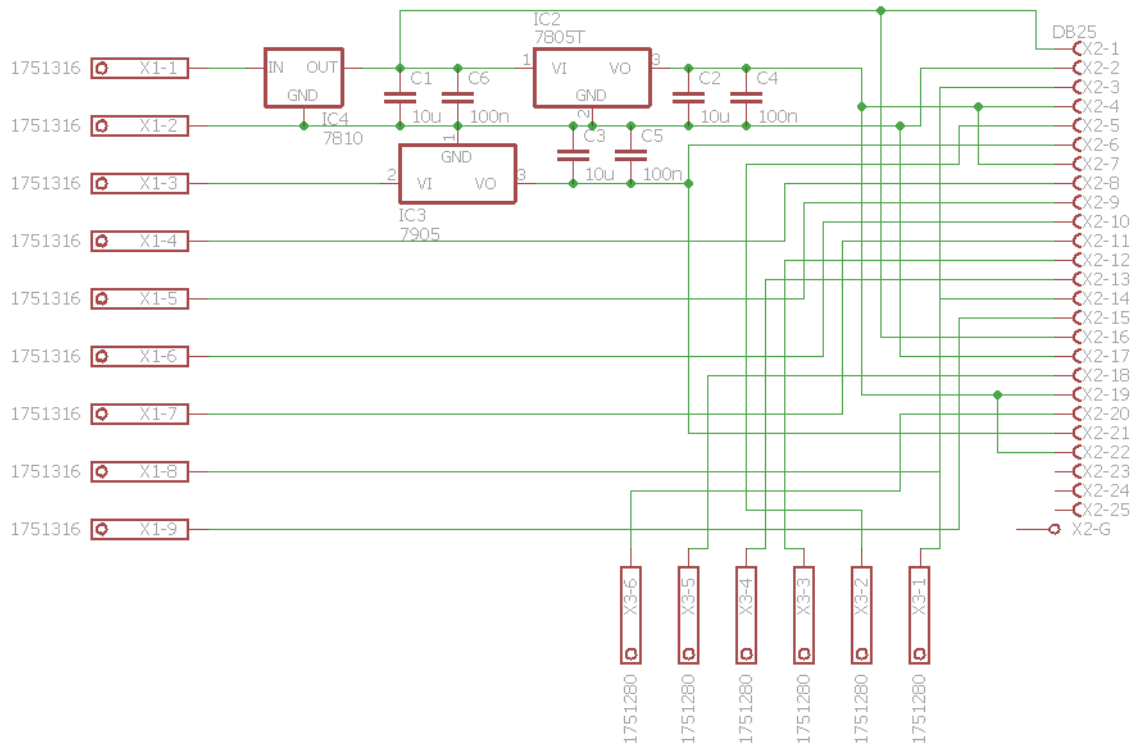
Figure A.5:   The circuit layout of the interface board. The circuit provides voltage to voltage converters and splits the data and power lines.
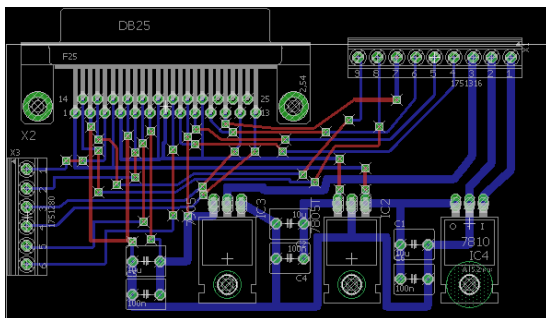
Figure A.6:   The board layout of the splitter circuit.
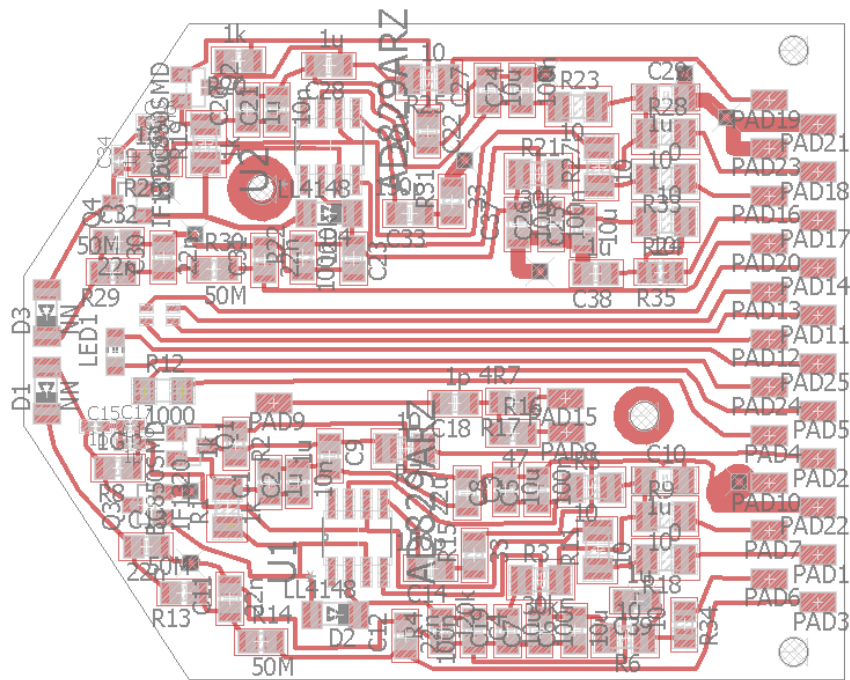
Figure A.7: The board layout of the preamplifier circuit. The connector for the 22 pads is a specially designed PEEK connector (see Fig. A.14 and A.13).

The bonding of Hamamatsu *p-i-n* diodes on the FBM detector board
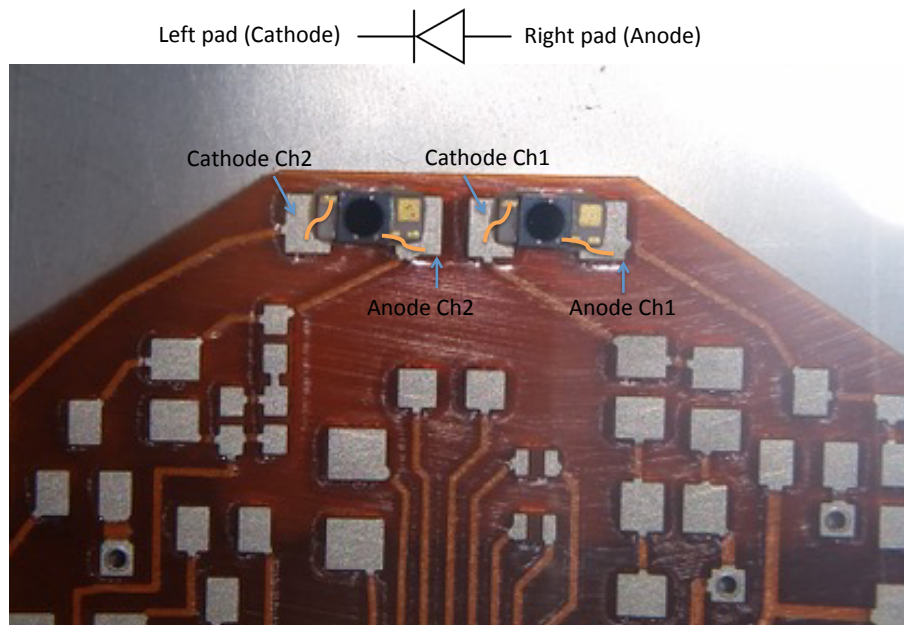
Figure A.8: The bonding of the *p-i-n* diodes. The figure shows the *p-i-n* diodes as they are positioned between their corresponding pads (cathode and anode pad).
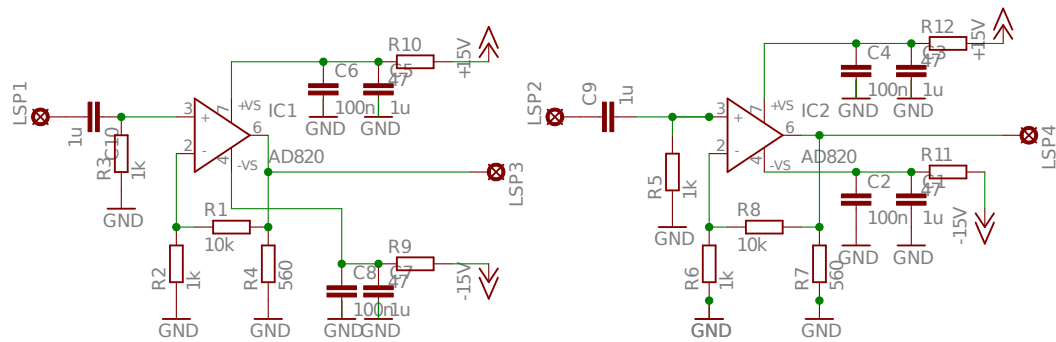
Figure A.9: The circuit layout of the second stage preamplifier. The drawing shows the electronic layout of the two equivalent amplifiers which are installed outside the vacuum chamber to further amplify the signal originating from the charge sensitive (first stage) preamplifiers.

A.5 Technical drawings

All technical drawings of the FBM are stored in Wuppertal and Karlsruhe and can be viewed upon request. Since the Wuppertal e-gun is not a part of the FBM its technical drawing are given below. Further more three-dimensional CAD drawings of the PEEK connector and the detector holder are shown to help the reader understanding how the front end is assembled.
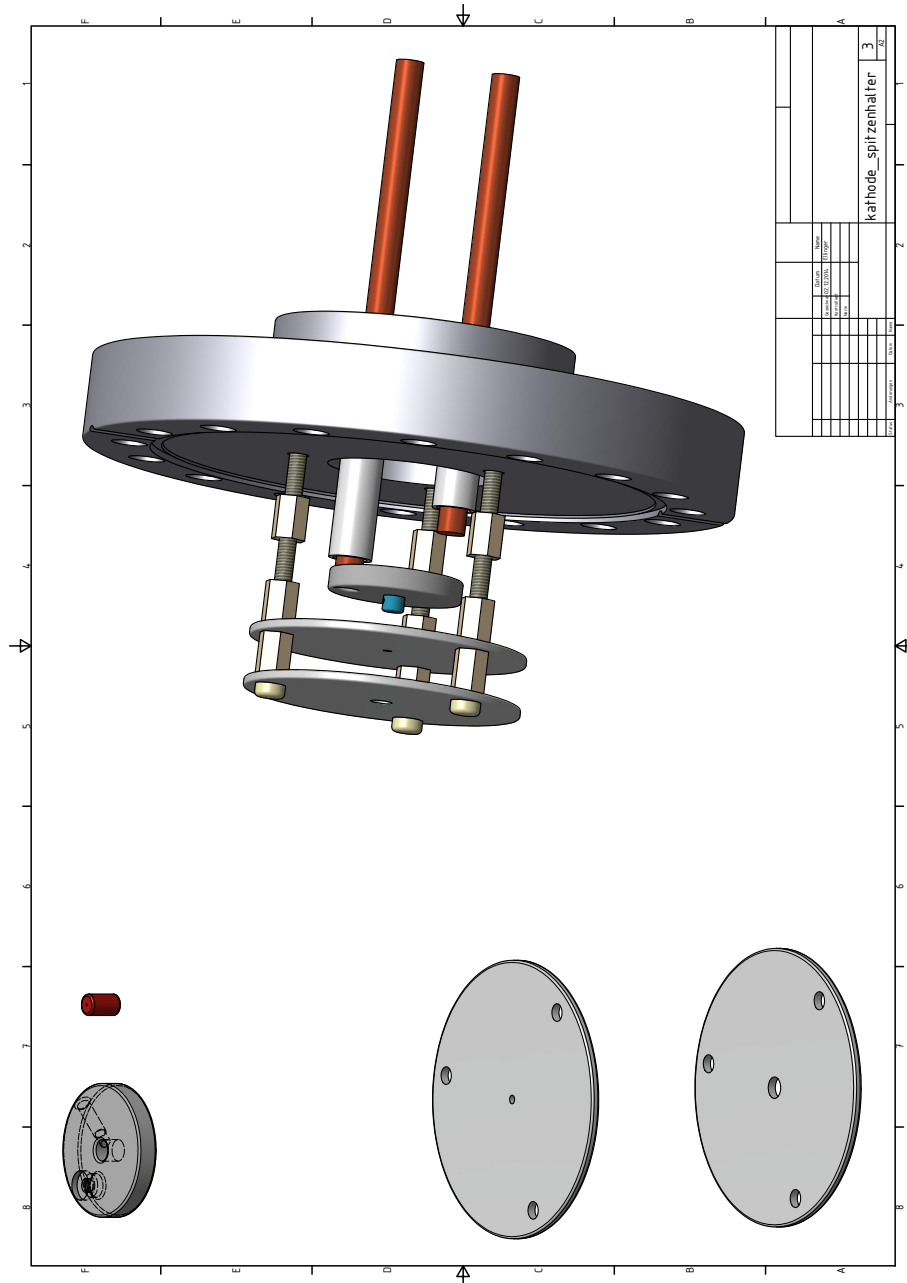
Figure A.10: Three-dimensional CAD drawing of the Wuppertal e-gun.
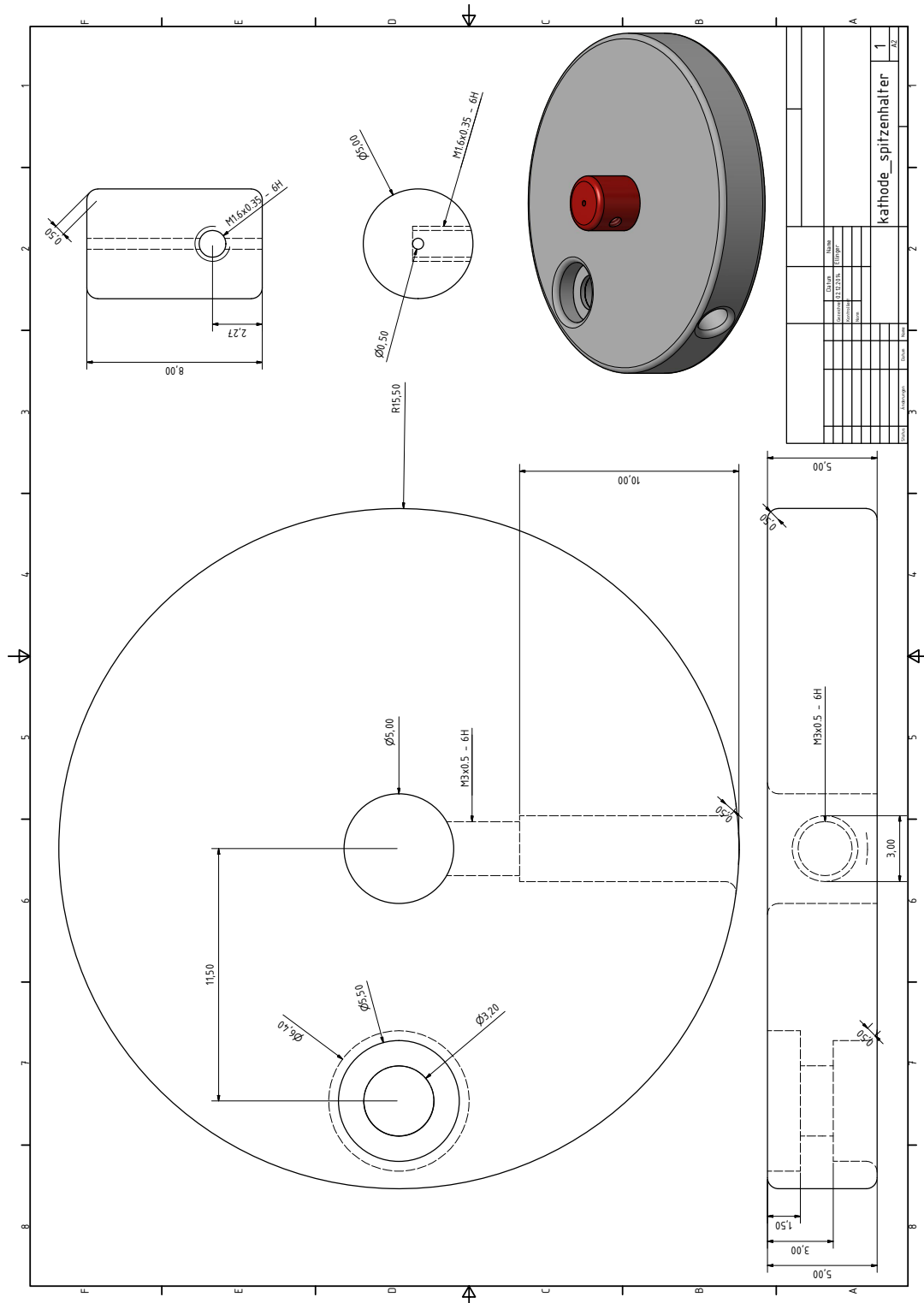
Figure A.11: Technical drawing of the cathode K1 und the tip holder of the Wuppertal e-gun. The cathode is directly attached to one of the electrical feed throughs. The tip holder as well as the tip itself are fixed from the side with grub screws.

Figure A.12: Technical drawing of the electrodes K2 und K3 of the Wuppertal e-gun.

Figure A.13:   Three-dimensional CAD drawing of the assembly of the front end. The detector board is glued to the back plate and fixed with two distance holders which also serve as mounting points for the cover. The polyimide insulated wires are soldered to the pogo pins which are situated in the PEEK connector. The connector itself is mounted by pressing it against the pads and tightening it with two screws. Due to the pogo pins the connection to the pads is ensured.

Figure A.14: The vacuum sided detector board connector is made of PEEK which is a organic thermoplastic polymer.

References

[Abd02] J. N. Abdurashitov et al. (SAGE), Solar neutrino flux measurements by the Soviet-American Gallium Experiment (SAGE) for half the 22 year solar cycle. *J. Exp. Theor. Phys.*, 95:181–193 (2002), doi:10.1134/1.1506424, [Zh. Eksp. Teor. Fiz.122,211(2002)], astro-ph/0204245 (cit. on p. 6)

[Abe08] Abe, S. et al. (KamLAND Collaboration), Precision Measurement of Neutrino Oscillation Parameters with KamLAND. *Physical Review Letters*, 100:221803 (2008), doi:10.1103/PhysRevLett.100.221803 (cit. on p. 7)

[Ada13] Adamson, P. et al. (MINOS Collaboration), Measurement of Neutrino and Antineutrino Oscillations Using Beam and Atmospheric Data in MINOS. *Physical Review Letters*, 110:251801 (2013), doi:10.1103/PhysRevLett.110.251801 (cit. on p. 7)

[Adu] Adundovi, Pn-junction-equilibrium-graph (cit. on p. 51)

[Agh18] N. Aghanim et al. (Planck), Planck 2018 results. VI. Cosmological parameters (2018), 1807.06209 (cit. on p. 11)

[Ago03] Agostinelli, S. et al., Geant4 - a simulation toolkit. *Nuclear Instruments and Methods in Physics Research Section A: Accelerators, Spectrometers, Detectors and Associated Equipment*, 506(3):250–303 (2003), doi:10.1016/S0168-9002(03)01368-8 (cit. on p. 106)

[Ago13] Agostini, M. et al. (GERDA Collaboration), Results on Neutrinoless Double-β Decay of ^{76}Ge from Phase I of the GERDA Experiment. *Physical Review Letters*, 111:122503 (2013), doi:10.1103/PhysRevLett.111.122503 (cit. on p. 12)

[Ahm02] Q. R. Ahmad, R. C. Allen, and T. C. e. a. Andersen (SNO Collaboration), Direct Evidence for Neutrino Flavor Transformation from Neutral-Current Interactions in the Sudbury Neutrino Observatory. *Phys. Rev. Lett.*, 89:011301 (2002), doi:10.1103/PhysRevLett.89.011301 (cit. on p. 7)

[Are16] M. Arenz, M. Babutzka, and M. B. et al., Commissioning of the vacuum system of the KATRIN Main Spectrometer. *Journal of Instrumentation*, 11:P04011 (2016), doi:10.1088/1748-0221/11/04/P04011, 1603.01014 (cit. on p. 41)

[Are18] M. e. a. Arenz (KATRIN), First transmission of electrons and ions through the KATRIN beamline. *JINST*, 13(04):P04020 (2018), doi:10.1088/1748-0221/13/04/P04020, 1802.04167 (cit. on pp. 25 and 78)

[Ase11] V. Aseev, A. Belesev, A. Berlev, E. Geraskin, A. Golubev, N. Likhovid, V. Lobashev, A. Nozik, V. Pantuev, V. Parfenov, A. Skasyrskaya, F. Tkachov, and S. Zadorozhny, Upper limit on the electron antineutrino mass from the Troitsk experiment. *Physical Review D*, 84:112003 (2011), doi:10.1103/PhysRevD.84.112003 (cit. on p. 14)

[Aug12] M. Auger, D. J. Auty, and P. S. e. a. Barbeau (EXO Collaboration), Search for Neutrinoless Double-Beta Decay in ^{136}Xe with EXO-200. *Phys. Rev. Lett.*, 109:032505 (2012), doi:10.1103/PhysRevLett.109.032505 (cit. on p. 12)

[Bab10a] M. Babutzka, Untersuchung eines verfahrbaren Monitordetektors zur Überwachung der Aktivität des β-Zerfalls in der kryogenen Pumpstrecke des KATRIN-Experiments. Diploma thesis, Karlsruher Institut für Technologie (KIT) (2010) (cit. on p. 54)

[Bab10b] M. Babutzka, Untersuchung eines verfahrbaren Monitordetektors zur Überwachung der Aktivität des -Zerfalls in der kryogenen Pumpstrecke des KATRIN Experiments. *Diplomarbeit* (2010) (cit. on pp. 9, 25, 43, and 47)

[Bab12] M. Babutzka, M. Bahr, and J. B. et al., Monitoring of the operating parameters of the KATRIN Windowless Gaseous Tritium Source. *New Journal of Physics*, 14(10):103046 (2012), doi:10.1088/1367-2630/14/10/103046 (cit. on p. 24)

[Bab14] M. Babutzka, Design and development for the Rearsection of the KATRIN experiment. Ph.D. thesis (2014), doi:10.5445/IR/1000045598 (cit. on pp. 22 and 24)

[Bah05] J. N. Bahcall, A. M. Serenelli, and S. Basu, New Solar Opacities, Abundances, Helioseismology, and Neutrino Fluxes. *The Astrophysical Journal*, 621(1):L85–L88 (2005), doi:10.1086/428929 (cit. on p. 5)

[Beh18] J. Behrens, Beam size and magentic field of the RS e-gun during the STSIIIa campaign of KATRIN. Private conversation (2018) (cit. on p. 89)

[Ber12] Beringer, J. et al. (Particle Data Group), Review of Particle Physics. *Physical Review D*, 86:010001 (2012), doi:10.1103/PhysRevD.86.010001 (cit. on p. 58)

[Bes11] B. Beskers, Messung und Optimierung der Eigenschaften des Monitordetektors fur keV-Elektronen in der kryogenen Pumpstrecke bei KATRIN. *Diplomarbeit* (2011) (cit. on p. 25)

[Bog00] J. Boger et al. (SNO), The Sudbury neutrino observatory. *Nucl. Instrum. Meth.*, A449:172–207 (2000), doi:10.1016/S0168-9002(99)01469-2, nucl-ex/9910016 (cit. on p. 6)

[Cam85] J. Campbell, B. Millman, J. Maxwell, A. Perujo, and W. Teesdale, Analytic fitting of monoenergetic peaks from Si(Li) X-ray spectrometers. *Nuclear Instruments and Methods in Physics Research Section B: Beam Interactions with Materials and Atoms*, 9(1):71 – 79 (1985), ISSN 0168-583X, doi:https://doi.org/10.1016/0168-583X(85)90780-3 (cit. on p. 65)

[Chi10] S. Chilingaryan, A. Beglarian, A. Kopmann, and S. Vöcking, Advanced data extraction infrastructure: Web based system for management of time series data. *Journal of Physics: Conference Series*, 219(4):042034 (2010), doi:10.1088/1742-6596/219/4/042034 (cit. on p. 35)

[Cle98] B. Cleveland, T. Daily, J. R. Davis, J. Distel, K. Lande, C. Lee, P. Wildenhain, and J. Ullman, Measurement of the Solar Electron Neutrino Flux with the Homestake Chlorine Detector. *The Astrophysical Journal*, 496(1):505 (1998), doi:10.1086/305343 (cit. on p. 5)

[Cow56] C. L. Cowan, F. Reines, F. B. Harrison, H. W. Kruse, and A. D. McGuire, Detection of the free neutrino: A Confirmation. *Science*, 124:103–104 (1956), doi:10.1126/science.124.3212.103 (cit. on p. 4)

[Dan62] G. Danby, J.-M. Gaillard, K. Goulianos, L. M. Lederman, N. Mistry, M. Schwartz, and J. Steinberger, Observation of High-Energy Neutrino Reactions and the Existence of Two Kinds of Neutrinos. *Phys. Rev. Lett.*, 9:36–44 (1962), doi: 10.1103/PhysRevLett.9.36 (cit. on p. 4)

[Ekv99] I. Ekvall, E. Wahlstrom, D. Claesson, H. Olin, and E. Olsson, Preparation and characterization of electrochemically etched W tips for STM. *Measurement Science and Technology*, 10:11 (1999), doi:10.1088/0957-0233/10/1/006 (cit. on p. 105)

[Fer34] E. Fermi, Versuch einer Theorie der β-Strahlen. *Zeitschrift für Physik*, 88(3–4):161–177 (1934), doi:10.1007/BF01351864 (cit. on p. 3)

[Fuk98] Y. Fukuda, T. Hayakawa, and E. e. a. Ichihara (Super-Kamiokande Collaboration), Evidence for Oscillation of Atmospheric Neutrinos. *Phys. Rev. Lett.*, 81:1562–1567 (1998), doi:10.1103/PhysRevLett.81.1562 (cit. on p. 6)

[Fuk03] Y. Fukuda et al. (Super-Kamiokande), The Super-Kamiokande detector. *Nucl. Instrum. Meth.*, A501:418–462 (2003), doi:10.1016/S0168-9002(03)00425-X (cit. on p. 6)

[Fur17] D. Furse, S. Groh, and N. T. et al., Kassiopeia: a modern, extensible C++ particle tracking package. *New Journal of Physics*, 19(5):053012 (2017), doi:10. 1088/1367-2630/aa6950 (cit. on p. 32)

[Gan16] A. Gando et al. (KamLAND-Zen), Search for Majorana Neutrinos near the Inverted Mass Hierarchy Region with KamLAND-Zen. *Phys. Rev. Lett.*, 117(8):082503 (2016), doi:10.1103/PhysRevLett.117.109903,10.1103/ PhysRevLett.117.082503, [Addendum: Phys. Rev. Lett.117,no.10,109903(2016)], 1605.02889 (cit. on p. 12)

[Gol58] M. Goldhaber, L. Grodzins, and A. W. Sunyar, Helicity of Neutrinos. *Phys. Rev.*, 109:1015–1017 (1958), doi:10.1103/PhysRev.109.1015 (cit. on p. 5)

[Ham99] W. Hampel et al. (GALLEX), GALLEX solar neutrino observations: Results for GALLEX IV. *Phys. Lett.*, B447:127–133 (1999), doi:10.1016/S0370-2693(98) 01579-2 (cit. on p. 6)

[Hau18] N. Haußmann, Simulation of the magentic field in the CPS. Private conversation (2018) (cit. on p. 92)

[Hau19] N. Haußmann, Simulation and measurement of the Forward Beam Monitor detector signal in KATRIN. Ph.D. thesis, Bergische Universität Wuppertal, Unpublished doctoral dissertation (2019) (cit. on pp. 80, 94, 107, 109, 110, and 112)

[How04] M. Howe, G. Cox, P. Harvey, F. McGirt, K. Rielage, J. Wilkerson, and J. Wouters, Sudbury Neutrino Observatory neutral current detector acquisition software overview. *IEEE Transactions on Nuclear Science*, 51(3):878–883 (2004), doi:10.1109/TNS.2004.829527 (cit. on pp. 34 and 54)

[Inc18] C. Inc., Circuit diagrams of charge sensitive preamplifier (2018), online; accessed October 14, 2018 (cit. on p. 53)

[Jan15] A. Jansen, The Cryogenic Pumping Section of the KATRIN Experiment - Design Studies and Experiments for the Commissioning. Ph.D. thesis, Karlsruher Institut für Technologie (KIT) (2015) (cit. on p. 20)

[JP99] C. J. Powell and J. AJ, Evaluation of Calculated and Measured Electron Inelastic Mean Free Paths Near Solid Surfaces. *Journal of Physical and Chemical Reference Data - J PHYS CHEM REF DATA*, 28:19–62 (1999), doi:10.1063/1.556035 (cit. on p. 49)

[Kar00] A. K. Kar, S. Gangopadhyay, B. K. Mathur, and S. Gangopadhyay, A reverse electrochemical floating-layer technique of SPM tip preparation. *Measurement Science and Technology*, 11:1426–1431 (2000), doi:10.1088/0957-0233/11/10/302 (cit. on p. 100)

[KAT05] KATRIN collaboration, KATRIN Design Report. FZKA scientific report 7090 (2005) (cit. on pp. 13, 15, 16, 22, and 23)

[Kin13] S. F. King and C. Luhn, Neutrino Mass and Mixing with Discrete Symmetry. *Rept. Prog. Phys.*, 76:056201 (2013), doi:10.1088/0034-4885/76/5/056201, 1301.1340 (cit. on p. 10)

[Kle97] M. Klein and G. Schwitzgebel, An improved lamellae drop-off technique for sharp tip preparation in scanning tunneling microscopy. *Review of Scientific Instruments*, 68:3099–3103 (1997), doi:10.1063/1.1148249 (cit. on p. 100)

[Kle18] M. Klein, Tritium ions in KATRIN: blocking, removal and detection. Ph.D. thesis, Karlsruher Institut für Technologie (KIT) (2018) (cit. on p. 78)

[Kod01] K. Kodama et al. (DONUT), Observation of tau neutrino interactions. *Phys. Lett.*, B504:218–224 (2001), doi:10.1016/S0370-2693(01)00307-0, hep-ex/0012035 (cit. on p. 4)

[Kra05] C. Kraus, B. Bornschein, L. Bornschein, J. Bonn, B. Flatt, A. Kovalik, B. Ostrick, E. Otten, J. Schall, T. Thümmler, and C. Weinheimer, Final results from phase II of the Mainz neutrino mass search in tritium β decay. *The European Physical Journal C - Particles and Fields*, 40(4):447–468 (2005), doi:10.1140/epjc/s2005-02139-7 (cit. on p. 14)

[Kul03] M. Kulawik, M. Nowicki, G. Thielsch, L. Cramer, H. Rust, H.-J. Freund, T. P. Pearl, and P. Weiss, A double lamellae dropoff etching procedure for tungsten tips attached to tuning fork atomic force microscopy/scanning tunneling microscopy sensors. *Review of Scientific Instruments*, 74:1027–1030 (2003), doi:10.1063/1.1532833 (cit. on p. 101)

[Lob85] V. Lobashev and P. Spivak, A method for measuring the electron antineutrino rest mass. *Nuclear Instruments and Methods in Physics Research Section A: Accelerators, Spectrometers, Detectors and Associated Equipment*, 240(2):305–310 (1985), doi:10.1016/0168-9002(85)90640-0 (cit. on p. 15)

[Mer18] S. Mertens et al. (KATRIN), A novel detector system for KATRIN to search for keV-scale sterile neutrinos (2018), 1810.06711 (cit. on p. 113)

[Ott08]   E. Otten and C. Weinheimer, Neutrino mass limit from tritium β decay. *Reports on Progress in Physics*, 71(8):086201 (2008), doi:10.1088/0034-4885/71/8/086201 (cit. on p. 13)

[Pas]   R. Paschotta, article on 'p–i–n photodiodes' in the Encyclopedia of Laser Physics and Technology (cit. on p. 51)

[Pau64]   W. Pauli, R. Kronig, and V. Weisskopf, Collected scientific papers. Interscience, New York, NY (1964), offener Brief an die Gruppe der Radioaktiven bei der Gauvereinstagung zu Tübingen (datiert 4. Dez. 1930) (cit. on p. 3)

[Pic92]   A. Picard, H. Backe, and H. B. et al., A solenoid retarding spectrometer with high resolution and transmission for keV electrons. *Nuclear Instruments and Methods in Physics Research Section B: Beam Interactions with Materials and Atoms*, 63(3):345–358 (1992), doi:10.1016/0168-583X(92)95119-C (cit. on p. 15)

[Rei53]   F. Reines and C. Cowan, Detection of the Free Neutrino. *Physical Review*, 92:830–831 (1953), doi:10.1103/PhysRev.92.830 (cit. on pp. III, 1, and 4)

[Ren11]   P. Renschler, KESS - A new Monte Carlo simulation code for low-energy electron interactions in silicon detectors. Ph.D. thesis, Karlsruher Institut für Technologie (KIT) (2011) (cit. on p. 109)

[SC]   L. E. S.Y.F. Chu and R. Firestone, WWW Table of Radioactive Isotopes, URL http://nucleardata.nuclear.lu.se/nucleardata/toi/ (cit. on p. XIII)

[Sch]   U. Schmitt, R. Gehring, F. Gluck, M. Steidl, and S. Wuestling, Proposal KATRIN Forward Beam Monitor Detector Design Document Version 1.2 (cit. on pp. 25 and 28)

[Sch08]   U. Schmitt, Entwicklung eines Monitordetektors für das KATRIN-Experiment. Ph.D. thesis, KIT, Karlsruhe, EKP (2008) (cit. on pp. 25, 28, 32, and 47)

[Sch11]   M. Schlösser, S. Fischer, M. Sturm, B. Bornschein, R. Lewis, and H. Telle, Design Implications for Laser Raman Measurement Systems for Tritium Sample-Analysis, Accountancy or Process-Control Applications. *Fusion Science and Technology*, 60(3):976–981 (2011) (cit. on p. 23)

[Sch17]   S. Schubotz, Untersuchung des Magnetfeldes der kryogenen Pumpstrecke des KATRIN-Experiments mittels des Forward Beam Monitors (2017), bachelor Thesis (cit. on pp. 41, 92, and 93)

[Tan18]   M. Tanabashi, K. Hagiwara, K. Hikasa, K. Nakamura, Y. Sumino, F. Takahashi, and J. e. a. Tanaka (Particle Data Group), Review of Particle Physics. *Phys. Rev. D*, 98:030001 (2018), doi:10.1103/PhysRevD.98.030001 (cit. on pp. 7, 11, and 49)

[Tep13]   A. Tepe, Design Document for the Forward Beam Monitor (2013) (cit. on p. 29)

[Ubi11]   M. Ubieto Díaz, Off-line commissioning of a non-destructive FT-ICR detection system for monitoring the ion concentration in the KATRIN beamline. Ph.D. thesis, Ruperto-Carola University of Heidelberg (2011) (cit. on p. 19)

[UD09]   M. Ubieto-Díaz, D. Rodríguez, S. Lukic, S. Nagy, S. Stahl, and K. Blaum, A broad-band FT-ICR Penning trap system for KATRIN. *International Journal of Mass Spectrometry*, 288(1–3):1–5 (2009), doi:10.1016/j.ijms.2009.07.003 (cit. on p. 19)

[Wal14] B. Wall, J. Amsbaugh, and A. B. et al., Dead layer on silicon p-i-n diode charged-particle detectors. *Nuclear Instruments and Methods in Physics Research Section A: Accelerators, Spectrometers, Detectors and Associated Equipment*, 744(0):73–79 (2014), doi:10.1016/j.nima.2013.12.048 (cit. on p. 109)

[Wan13] N. Wandkowsky, Study of background and transmission properties of the KATRIN spectrometers. Ph.D. thesis, Karlsruher Institut für Technologie (KIT) (2013) (cit. on pp. 19 and 20)

[Wei35] C. F. V. Weizsäcker, Zur Theorie der Kernmassen. *Zeitschrift fur Physik*, 96:431–458 (1935), doi:10.1007/BF01337700 (cit. on p. 12)

[Wro05] F. Wrobel, Short Course Notebook – New challenges for Radiation Tolerance Assessment. 5–31 (2005) (cit. on p. 48)

[Zel18] G. Zeller, Detailed analysis on correlations between FBM and LARA data during the first tritium campaign of KATRIN. Private conversation (2018) (cit. on pp. 85 and 88)

List of Figures

List of Tables

Nomenclature

ADEI   Advanced Data Extraction Infrastructure

CAD   Computer-Aided Design

CKrS   Condensed Krypton Source

CMM   Coordinate Measuring Machine

CPS   Cryogenic Pumping Section

DPS   Differential Pumping Section

FBM   Forward Beam Monitor

FPD   Focal Plane Detector

FPGA   Field-Programmable Gate Array

FT-ICR   Fourier Transform-Ion Cyclotron Resonance mass spectrometer

GUI   Graphical User Interface

IPE   Data Processing and Electronics

KATRIN   KArlsruhe TRItium Neutrino experiment

KESS   KATRIN Electron Scattering in Silicon

KIT   Karlsruhe Institute of Technology

MAC-E   Magnetic Adiabatic Collimation with Electrostatic

PP2   Pump Port 2

RGA   Residual Gas Analyzer

RS   Rear Section

SDS   Spectrometer and Detector Section

STS   Source and Transport Section

TLK   Tritium Laboratory Karlsruhe

TMP   Turbomolecular pump

UHV   Ultra-High Vacuum

WGTS   Windowless Gaseous Tritium Source